



This is to certify that the
dissertation entitled

FABRICATION, CHARACTERIZATION, AND
ELECTROCATALYTIC ACTIVITY OF METAL/DIAMOND
COMPOSITE ELECTRODES

presented by

Jian Wang

has been accepted towards fulfillment
of the requirements for the

Ph.D. degree in Chemistry


Major Professor's Signature

12/20/02

Date

PLACE IN RETURN BOX to remove this checkout from your record.
TO AVOID FINES return on or before date due.
MAY BE RECALLED with earlier due date if requested.

DATE DUE	DATE DUE	DATE DUE
MAY 06 2006		
04 20 06		
OCT 27 2006		
JUN 19 2006		
JAN 09 2007		
08 27 06		
NOV 28 2007		

**FABRICATION, CHARACTERIZATION, AND
ELECTROCATALYTIC ACTIVITY OF METAL/DIAMOND
COMPOSITE ELECTRODES**

By

Jian Wang

A DISSERTATION

Submitted to
Michigan State University
in partial fulfillment of the requirements
for the degree of

DOCTOR OF PHILOSOPHY

Department of Chemistry

2002

ABSTRACT

FABRICATION, CHARACTERIZATION, AND ELECTROCATALYTIC ACTIVITY OF METAL/DIAMOND COMPOSITE ELECTRODES

By

Jian Wang

This dissertation is devoted to a new research area of diamond electrochemistry: application of boron-doped diamond thin-film electrodes in the field of electrocatalysis. The main focus is on the fabrication and characterization of Pt/diamond composite electrodes and on the investigation of their electrocatalytic activities.

Dimensionally stable Pt/diamond composite electrodes are fabricated by a sequential diamond growth/ Pt deposition/ diamond growth procedure. In this multistep process, a continuous boron-doped diamond thin film is first deposited on a conductive substrate (e.g. Pt, Si or W). DC magnetron sputtering or electrodeposition is next used to deposit a discontinuous layer of Pt particles on the surface. The Pt-coated diamond film is then subjected to a short, secondary diamond growth in order to anchor the metal particles into the diamond surface microstructure.

The resulting Pt/diamond composite films are characterized by SEM, EDX, AFM, AES, XRD, SIMS, Raman spectroscopy, and cyclic voltammetry. The metal particles range in diameter from 10 to 500 nm. In the electrodeposition approach, the number of exposed metal particles, particle size, and distribution can be controlled, to some extent, by adjusting the electrodeposition and secondary diamond growth conditions. The second, short diamond deposition serves to entrap many of the metal particles into the

diamond microstructure by surrounding their base. Consequently, there is little catalyst detachment or particle aggregation during use under extreme conditions. The catalytic activity of the composite electrodes is extremely stable, as no microstructural alterations or activity losses were observed during a 2 h anodic polarization in 85% H₃PO₄ at 0.1 A·cm⁻² and 170°C.

The electrode's catalytic activity is evaluated using the oxygen reduction reaction and methanol oxidation reaction, at room temperature in acidic media. The catalytic activities of the composite electrode are found to be comparable to those for a polycrystalline and carbon-supported Pt catalyst. The results suggest that there is little alteration of the physicochemical properties of the Pt catalyst during secondary diamond growth. The diamond film exhibits metal-like electrical conductivity as both a support material and a current collector.

As part of the groundwork for my research, copper electrodeposition is investigated in order to gain a fundamental understanding of metal nucleation/growth on diamond surface. The electrodeposition of copper is strongly influenced by the electronic properties (i.e., doping level) of the diamond film. An increase in the boron-doping level significantly increases the number density of nucleation sites and alters the nucleation mechanism. The size of the metal deposits, their spatial distribution and number density are potentially to be controlled by adjusting the applied overpotential, deposition time and electrical conductivity (i.e., boron doping level) of the diamond film.

ACKNOWLEDGEMENTS

I am appreciative of all those who have helped along the way. Foremost, I would like to thank my advisor, Dr. Greg M. Swain, for his long-term patience, constant support, and never-ending encouragement during my entire graduate education. Greg has been a great mentor. Not only has he expertly guided my scientific development, but his extra personal touch has also helped me over many rough spots during the past five years.

I am also grateful to my former advisory committee members at Utah State University, Dr. Robert Brown, Dr. Stephen Bialkowski, Dr. John Hubbard, and Dr. T. C. Shen. Their constant guidance and encouragement have played a critical role at the early stage of my research. I would also like to thank my committee members at Michigan State University, Dr. Simon Garrett, Dr. Thomas Pinnavaia, and Dr. Jes Asmussen, for reading my thesis and providing helpful suggestions.

The deepest gratitude goes to my parents, in-laws, my sisters and brother-in-laws for their unreserved support, love, and trust in these years. Special thanks are given to my wife, Ning Yu. She has sacrificed so much, particularly during my two-year stay here at Michigan, so that I could finally make it through my graduate study. It is her love, understanding, and support that make it possible for me to overcome the obstacles I faced during the past five years.

Many people I have met in the Swain research group have been a source of support at one time or another during my graduate career. Special thanks go to three visiting scientists: Dr. Jerzy Strojek taught me most of the experimental skills when I joined the group. Dr. Jerzy Zak and Dr. Miles Koppang were other mentors to me. Many

thought-provoking discussions with them expanded my knowledge of both experimental and theoretical aspects of this research. I would also like to thank the past and present Swain group members: Mike, Jishou, Qingyun, Matt, Maggie, Prerna, Jason B, Jason S, Shannon, JinWoo, Show, Grace, and Gloria. Thank you for all the friendships I have acquired, which have made my graduate life a really enjoyable one.

Finally, I gratefully acknowledge the Office of Science, Department of Energy for the financial support, Utah State University and Michigan State University for the Graduate Teaching and Research Assistantships, and Seagate Technology for the 2002 Summer Internship.

TABLE OF CONTENTS

LIST OF TABLES.....	viii
LIST OF FIGURES.....	x
CHAPTER 1 INTRODUCTION	1
1.1 Electrocatalysis and Direct Methanol Fuel Cells	1
1.2 Carbon Support Materials	4
1.3 The Problem	5
1.4 Diamond Electrochemistry.....	8
1.5 The Motivations.....	17
1.6 Outline of the Dissertation	18
References.....	21
CHAPTER 2 ELECTROCHEMICAL AND IN SITU ATOMIC FORCE MICROSCOPIC STUDIES OF COPPER DEPOSITION ON BORON-DOPED DIAMOND THIN-FILM ELECTRODES	25
2.1 Introduction	25
2.2 Experimental	27
2.3 Theories of Metal Nucleation and Growth.....	32
2.4 Results.....	36
2.4.1 Electrochemical Study of Copper Deposition	36
2.4.2 ECAFM Study of Copper Deposition	50
2.5 Discussion	63
2.6 Conclusions	68
References.....	70
CHAPTER 3 FABRICATION AND CHARACTERIZATION OF DIMENSIONALLY STABLE PT/DIAMOND COMPOSITE ELECTRODES FOR ELECTROCATALYSIS — THE MAGNETRON SPUTTERING APPROACH ...	73
3.1 Introduction	73
3.2 Experimental	75
3.3 Results and Discussion	78
3.3.1 Structural Characterization.....	78
3.3.2 Electrochemical Characterization	85
3.4 Conclusions	94
References.....	95
CHAPTER 4 FABRICATION AND CHARACTERIZATION OF DIMENSIONALLY STABLE PT/DIAMOND COMPOSITE ELECTRODES FOR ELECTROCATALYSIS — THE ELECTRODEPOSITION APPROACH	97
4.1 Introduction	97
4.2 Experimental	99
4.3 Results and Discussion	103

4.3.1 Electrodeposition of Pt on Diamond Thin Films	103
4.3.2 Secondary Diamond Growth	110
4.3.3 Stability of the Pt/Diamond Composite Electrode.....	121
4.4 Conclusions	124
References.....	125

**CHAPTER 5 OXYGEN REDUCTION REACTION ON PT/DIAMOND
COMPOSITE ELECTRODES — A ROTATING DISK VOLTAMMETRIC
STUDY.....**

5.1 Introduction	127
5.2 Mechanism and Kinetics of ORR	129
5.3 Experimental	131
5.4 Results and Discussion	133
5.4.1 Characterization of the Diamond Film on Mo Disk	133
5.4.2 ORR at Stationary Pt/Diamond Composite Electrodes.....	139
5.4.3 ORR at Pt/Diamond Composite RDEs	143
5.5 Conclusions	156
References.....	158

**CHAPTER 6 METHANOL OXIDATION REACTION ON METAL/DIAMOND
COMPOSITE ELECTRODES**

6.1 Introduction	160
6.2 Mechanism and Kinetics of MOR	162
6.3 Experimental	165
6.4 Results and Discussion	166
6.4.1 Measurement of the Open Circuit Potential	166
6.4.2 MOR at Pt/Diamond Composite Electrodes.....	168
6.4.2.1 Cyclic Voltammetric Studies of MOR	168
6.4.2.2 Chronoamperometric Studies of MOR.....	174
6.4.3 MOR at a Bimetallic Catalyst.....	179
6.5 Conclusions	183
References.....	184

LIST OF TABLES

Table 2.1. Summary of the diamond thin-film deposition parameters.....	28
Table 2.2. CV data for copper electrodeposition on different electrodes in 1 mM CuSO ₄ + 50 mM H ₂ SO ₄	38
Table 2.3. Current-time transient data for copper electrodeposition on LBD.....	44
Table 2.4. Current-time transient data for copper electrodeposition on HBD.....	44
Table 2.5. Current-time transient data for copper electrodeposition on HOPG.....	45
Table 2.6. Current-time transient data for copper electrodeposition on GC.....	45
Table 4.1. Pt particle size, distribution, hydrogen desorption charge and roughness factor (RF) for the Pt/diamond composite electrodes before and after the secondary diamond growth.....	108
Table 5.1. Electrochemically active surface area and roughness factor for the Pt/diamond composite RDEs with different Pt loadings.....	138
Table 5.2. Open circuit potentials (25 °C) for the Pt/diamond composite RDEs in different acid electrolytes.....	140
Table 5.3. Comparison of the kinetics parameters for ORR at the Pt/diamond composite electrodes with the literature data reported for single crystal, polycrystalline, and carbon-supported Pt at room temperature.....	152
Table 5.4. Comparison of the specific activity (SA) and mass activity (MA) of the Pt/diamond composite electrode for ORR with the literature data reported for other carbon-supported Pt electrodes.....	155
Table 6.1. Electrochemically active surface area and roughness factor for the polycrystalline Pt and Pt/diamond composite electrodes with different Pt loadings.....	166
Table 6.2. Open circuit potentials for Pt/diamond composite electrodes in 0.1 M HClO ₄ with different methanol concentrations.....	167
Table 6.3. Cyclic voltammetric data for the MOR in 0.1 M HClO ₄ at Pt/diamond composite electrodes with different Pt loadings.....	172

Table 6.4. Summary of the chronoamperometric i-t data for the oxidation of methanol at a Pt/diamond composite electrode in 0.1 M HClO ₄ as a function of the methanol concentration.....	179
--	-----

LIST OF FIGURES

Figure 1.1. (A) Schematic diagram of a direct methanol fuel cell working in an acidic medium. (B) Schematic diagram of a proton exchange membrane fuel cell. Highly-dispersed catalyst (small dots) is supported on carbon black particles (big dots).....	3
Figure 1.2. Diamond film morphologies as a function of methane-to-hydrogen source gas ratio used during microwave plasma CVD. The surface area is $10 \times 10 \mu\text{m}^2$. Z-axis range is $6 \mu\text{m}$. Hydrogen flow rate is 200 sccm. Growth time is 10 h.....	10
Figure 1.3. The effect of anodic polarization on the electrode morphology. Both the diamond film and glassy carbon electrodes were subjected to polarization at 2 V vs. Ag/AgCl in 0.1 M HClO ₄ . The <i>in situ</i> AFM images were recorded for polarization times 2, 10, and 15 min., respectively.....	14
Figure 2.1. Diagram of the single-compartment, glass electrochemical cell. (a) Cu or Al metal current collecting back plate, (b) working electrode, (c) Viton O-ring, (d) input for nitrogen purge gas, (e) carbon rod or Pt counter electrode, and (f) reference electrode inside a glass capillary tube with a cracked tip.	30
Figure 2.2. Diagram of the ECAFM fluid cell. (a) photodetector, (b) He-Ne laser, (c) auxiliary electrode, (d) reference electrode, (e) tip, (f) solution inlet, (g) solution outlet, (h) working electrode, (i) O-ring, and (j) piezoscanner.	31
Figure 2.3. (A) Schematic representation of the growth of the diffusion zones and their eventual overlap. The arrows indicate the directions of the diffusional field during the growth of the nuclei. (B) Typical current-time transient recorded during the potential step after background correction.....	34
Figure 2.4. Cyclic voltammetric i-E curves for copper deposition on (A) GC, (B) HBD, (C) LBD, and (D) HOPG in 1 mM CuSO ₄ + 50 mM H ₂ SO ₄ . Scan rate = 20 mV/s.....	37
Figure 2.5. Potentiostatic current-time transients for copper deposition on LBD in 1 mM CuSO ₄ + 50 mM H ₂ SO ₄ at the overpotentials indicated in mV.....	40
Figure 2.6. Comparison of experimental current-time transients (dash curves) for LBD (see Figure 2.5) with the theoretical transients corresponding to instantaneous (solid curve a) and progressive (solid curve b)	

nucleation at different overpotentials: (A) -410, (B) -460, (C) -510, (D) -610, (E) -660, and (F) -710 mV.....	42
Figure 2.7. Potentiostatic current-time transients for copper deposition on HBD in 1 mM CuSO ₄ + 50 mM H ₂ SO ₄ at the overpotentials indicated in mV.	43
Figure 2.8. Comparison of experimental current-time transients (dashed curves) for HBD (see Figure 2.7) with the theoretical transients corresponding to instantaneous (solid curve a) and progressive (solid curve b) nucleation at overpotentials of (A) -410 and (B) -610 mV.....	43
Figure 2.9. Comparison of experimental current-time transients (dashed curves) with the theoretical transients according to Equation 2.8 for copper deposition on LBD at overpotentials of (A) -410 and (B) -610 mV.....	46
Figure 2.10. Plot of the logarithm of the number density of active sites vs. overpotential, constructed from the data given in Table 2.3 and 2.4.	46
Figure 2.11. AFM images (force mode, in air, 5 × 5 μm) of (A) LBD, (B) HBD, (C) HOPG, and (D) GC.....	51
Figure 2.12. ECAFM images (force mode, 10 × 10 μm) collected for copper deposition on LBD at overpotentials of (B) 390 mV, (C) -460, (D) -560, (E) -710, and (F) 390 mV for 30 s each. The solution is 1mM CuSO ₄ + 50 mM H ₂ SO ₄ . (a)-(i) represent individual copper crystallite. The diagram of the sequential potential steps is shown in (A). The triangular markers indicate the starting time of each imaging.	54
Figure 2.13. ECAFM images (height mode, 2.5 × 2.5 μm) collected for copper deposition on LBD in 1mM CuSO ₄ + 50 mM H ₂ SO ₄ (A) before and (B-E) after the potential step to -460 mV. The deposition times are (B) 30, (C) 60, (D) 120, and (E) 180 s, respectively. Corresponding cross sections, through the top view images shown in the middle column, are indicated by the straight lines. The horizontal distance between the two black cursors represents the lateral dimension of the crystallite.....	55
Figure 2.14. ECAFM images (force mode, 4 × 4 μm) collected for copper deposition on LBD in 1mM CuSO ₄ + 50 mM H ₂ SO ₄ (B) before and (C-F) after the potential step to -710 mV. The deposition times are (C) 30, (D) 60, (E) 120, and (F) 180 s, respectively. (a)-(f) represent individual copper crystallite. The diagram of the potential step is shown in (A). The triangular markers indicate the starting time of each imaging.	57
Figure 2.15. ECAFM images (force mode, 5 × 5 μm) collected for copper deposition on HBD at overpotentials of (B) 390 mV, (C) -460, (D) -	

560, (E) -710, and (F) 390 mV for 30 s each. The solution is 1mM CuSO ₄ + 50 mM H ₂ SO ₄ . The diagram of the sequential potential steps is shown in (A). The triangular markers indicate the starting time of each imaging.....	61
Figure 2.16. ECAFM images (force mode, 3.4 × 3.4 μm) collected for copper deposition on HBD in 1mM CuSO ₄ + 50 mM H ₂ SO ₄ (B) before and (C-F) after the potential step to -460 mV. The deposition times are (C) 30, (D) 60, (E) 120, and (D) 180 s. (a)-(e) represent individual copper crystallite, respectively. The diagram of the potential step is shown in (A). The triangular markers indicate the starting time of each imaging.....	62
Figure 2.17. Proposed band structure for the diamond/electrolyte interface. E _{VB} , E _{CB} and E _{VAC} are the energies at the bottom of the conduction band, at the top of the valance band and in the vacuum. The potentials are quoted versus SCE. The band positions are determined using a flat-band potential of 0.45 V vs. SCE and a band gap of 5.45 eV.....	64
Figure 3.1. Fabrication process for the Pt/diamond composite electrodes.....	75
Figure 3.2. SEM images of composite diamond electrodes fabricated (A) with and (B) without Pt.....	78
Figure 3.4. Raman spectra for diamond composite electrodes fabricated with and without Pt. Excitation = 514.5 nm. Integration time = 10 s. The laser power density at the sample was estimated to be ca. 150 kW/cm ²	81
Figure 3.5. Dynamic SIMS profiles (positive ion mode) for diamond composite electrodes prepared (A) with and (B) without Pt.....	84
Figure 3.6. Cyclic voltammetric i-E curves for a Pt/diamond composite electrode in (A) 0.1 M HClO ₄ and (B) 1 M H ₂ SO ₄ . Scan rate = 50 mV/s.....	86
Figure 3.7. Cyclic voltammetric i-E curves in (A) 0.1 M HClO ₄ and (B) 1 M H ₂ SO ₄ for a composite electrode prepared without Pt. Scan rate = 50 mV/s.....	87
Figure 3.8. Cyclic voltammetric i-E curves in 0.1 M HClO ₄ for a Pt/diamond composite electrode before and after 1000 potential cycles between -400 and 1500 mV vs. Ag/AgCl. Scan rate = 50 mV/s. The maximum anodic and or cathodic current density during the cycling was ~1 mA/cm ²	89
Figure 3.9. Electrochemical AFM images for a Pt/diamond composite electrode in 0.1 M HClO ₄ (A) before and (B) after 1000 potential cycles between -400 and 1500 mV vs. Ag/AgCl. Scan rate = 50 mV/s. The z-	

axis is 4 nN full-scale. The images were acquired at 350 mV vs. Ag/AgCl.	91
Figure 3.10. Cyclic voltammetric i-E curves for boron-doped diamond composite electrodes with and without deposited with Pt in 0.6 M CH ₃ OH + 0.1 M HClO ₄ . Scan rate = 50 mV/s.	92
Figure 3.11. Cyclic voltammetric i-E curves for diamond composite electrodes, with and without Pt, in O ₂ -saturated 0.1 M HClO ₄ . Scan rate = 50 mV/s.	93
Figure 4.1. (A) Successive potentiodynamic i-E curves for a boron-doped diamond thin film in 1mM K ₂ PtCl ₆ + 0.1M HClO ₄ . Scan rate = 50mV/s. (B) AFM force-mode image (air) of the diamond thin film after 25 potential cycles.	104
Figure 4.2. AFM force-mode images (air) of boron-doped diamond thin films after galvanostatic deposition of Pt from a solution of 1 mM K ₂ PtCl ₆ + 0.1M HClO ₄ . The deposition times are (A) 100, (B) 200, (C), 300 and (D) 400 s, respectively.	107
Figure 4.3. Cyclic voltammetric i-E curves in 0.1 M HClO ₄ for a boron-doped diamond thin film electrodeposited with Pt, during 1000 potential cycles between -400 and 1500 mV vs. Ag/AgCl at 50 mV/s. Dashed arrows show the decrease in current response with scan number. The maximum anodic and/or cathodic current density during the cycling was ca. 1 mA/cm ²	109
Figure 4.4. AFM force-mode images (air) of Pt coated diamond thin films (as indicated in Figure 4.2) after a 3 h secondary diamond growth. The corresponding Pt deposition times are (A) 100, (B) 200, (C), 300 and (D) 400 s, respectively.	111
Figure 4.5. Energy dispersive x-ray analysis spectrum for a Pt metal particle shown in the SEM image (inset).	112
Figure 4.6. XRD pattern of a Pt/diamond composite electrode.	113
Figure 4.7. Cyclic voltammetric i-E curves for a Pt-coated diamond thin film in 0.1M HClO ₄ before (solid line) and after (dashed line) a 3 h of secondary diamond growth. The Pt deposition time was 200s. Scan rate = 50 mV/s.	116
Figure 4.8. SEM images of a Pt/diamond composite electrode (A) before and (B) after etching in aqua regia. The Pt deposition time was 200 s.	118

Figure 4.9. Cross-sectional SEM images of an acid-etched Pt/diamond composite electrode. (A) Secondary electron imaging mode. (B) Back-scattered electron imaging mode. The secondary diamond growth time was 3 h. Arrow 1-3 show three Pt particles covered by the diamond film. Arrow 4 shows a cavity after dissolving Pt.....	120
Figure 4.10. Cyclic voltammetric i-E curves for a Pt/diamond composite electrode in 0.1 M HClO ₄ before (dashed line) and after two 1-h polarizations (solid lines) in 85 wt % H ₃ PO ₄ at 170 °C and 0.1 A·cm ⁻² . The Pt deposition time was 200 s.	123
Figure 4.11. AFM images (air) of the Pt/diamond composite electrode (A) before and (B) after 2-h anodic polarization in 85 wt % H ₃ PO ₄ at 170 °C and 0.1 A·cm ⁻²	123
Figure 5.1. Schematic diagram of a rotating disk Pt/diamond composite electrode: a) a top and side view showing the direction of mass transport; b) a view of the electrode mounted in Teflon; c) a side view of the composite disk electrode architecture.	132
Figure 5.2. SEM image of a boron-doped diamond thin film deposited on a Mo disk. The diamond deposition time was 15 h and methane-to-hydrogen ratio was 0.35%.....	134
Figure 5.3. Raman spectrum for a boron-doped diamond thin film deposited on a Mo disk. Excitation wavelength = 532 nm. Incident power density = 500 kWcm ⁻² . Integration time = 10 s.	135
Figure 5.4. Cyclic voltammetric i-E curves for a boron-doped diamond thin film deposited on a Mo disk in 0.1 M HClO ₄ . Scan rate = 100 mV/s.....	137
Figure 5.5. Cyclic voltammetric i-E curves for Pt/diamond composite electrodes in 0.1 M HClO ₄ . The Pt deposition times were 200, 300, and 400 s, respectively. Scan rate = 50 mV/s.	137
Figure 5.6. Cyclic voltammetric i-E curves for (A) RDE #1 and (B) polycrystalline Pt foil electrode in N ₂ -purged (dashed line) and O ₂ -saturated (solid line) 0.1 M HClO ₄ . Scan rate 50 mV/s. Active surface area of the Pt foil electrode is 0.43 cm ² (geometric area is 0.2 cm ²).	141
Figure 5.7. Linear potential sweep voltammetric i-E curves for RDE #1 in O ₂ -saturated 0.1 M HClO ₄ at different scan rates. Inset shows the plot of peak potential vs. logarithm of scan rate.	142
Figure 5.8. Cyclic voltammetric i-E curves for RDE #3 in (A) N ₂ -purged and (B) O ₂ - saturated 0.1 M HClO ₄ . The dashed line is the curve for oxygen	

reduction after background correction. Scan rate = 20 mV/s. Rotation rate = 1000 rpm.....	144
Figure 5.9. Linear sweep voltammetric i-E curves for RDE#3 in O ₂ -saturated 0.1 M HClO ₄ as a function of the rotation rate. Scan rate = 20 mV/s.....	146
Figure 5.10. Koutechy-Levich plots for the oxygen reduction reaction in 0.1 M HClO ₄ . Data taken from the polarization curves shown in Figure 5.9.	148
Figure 5.11. Tafel plots for the oxygen reduction reaction in 0.1 M HClO ₄ . Data taken from the polarization curves shown in Figure 5.9.....	149
Figure 5.12. Tafel plots for the oxygen reduction reaction at RDE #3 in 0.1 M (A) HClO ₄ , (B) H ₂ SO ₄ and (C) H ₃ PO ₄ . Scan rate = 20 mV/s. Rotation rate = 2500 rpm.	151
Figure 5.13. Tafel plots for the oxygen reduction reaction in 0.1 M HClO ₄ at different Pt/diamond RDEs. Scan rate = 20 mV/s. Rotation rate = 2500 rpm.....	153
Figure 6.1. Cyclic voltammetric i-E curves for (A) Pt/diamond composite electrode and (B) polycrystalline Pt foil electrode in 0.1 M HClO ₄ + 0.2 M CH ₃ OH (solid line) and 0.1 M HClO ₄ (dashed line). Scan rate = 50 mV/s. Active surface area of the composite electrode is 0.44 cm ² (Pt deposition time was 200 s).....	169
Figure 6.2. Cyclic voltammetric i-E curves for Pt/diamond composite electrodes in 0.1 M HClO ₄ + 0.6 M CH ₃ OH. Scan rate = 50 mV/s.	172
Figure 6.3. Cyclic voltammetric i-E curves for the electrooxidation of 0.6 M CH ₃ OH in different 0.1 M acid electrolytes at a Pt/diamond composite electrode. Active surface area of the composite electrode is 0.44 cm ² (Pt deposition time was 200 s). Scan rate = 50 mV/s.	173
Figure 6.4. Current-time transients for a Pt/diamond composite electrode in 0.1 M HClO ₄ + 0.6 M CH ₃ OH at different electrode potentials. Active surface area of the composite electrode is 0.60 cm ²	175
Figure 6.5. Current-time transients for a Pt/diamond composite electrode obtained after a potential step to 0.6 V vs. Ag/AgCl in 0.1 M HClO ₄ containing different concentrations of methanol. Active surface area of the composite electrode is 0.60 cm ²	177
Figure 6.6. Log i vs. log c plot at 0.6 V vs. Ag/AgCl. Data taken from the current-time transients shown in Figure 6.5.....	177

Figure 6.7. AFM image ($10 \times 10 \mu\text{m}$) of a Pt/Ru/diamond composite electrode.
The deposition time is 300 s. 180

Figure 6.8. Cyclic voltammetric i-E curves for the Pt/Ru/diamond composite
electrodes in (A) 0.1 M HClO_4 and (B) 0.1M HClO_4 + 0.2 M CH_3OH .
The electrodeposition time is 300 s. Scan rate = 50 mV/s. 181

Chapter 1

Introduction

1.1 Electrocatalysis and Direct Methanol Fuel Cells

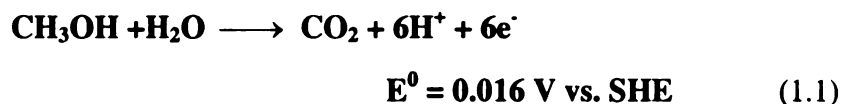
Electrocatalysis represents the combination of two important subdisciplines of physical chemistry, namely, electrochemistry and catalysis.¹ The term, which first appeared as early as 1963 in a paper by Grubb,² can be defined as the study of heterogeneous catalytic reactions that involve reactant and product species transferring electrons through an electrolyte/catalyst interface.³ An electrocatalyst is a conducting chemical entity that enhances the rate of an electrochemical reaction without being either consumed or generated in the process. Since an electrocatalyst is part of the electrode, sufficient electrical conductivity and electrochemical stability of the material at the operating electrode potential are essential.

The electrochemical technology mostly influenced by advances in electrocatalysis is electrochemical energy conversion, especially fuel cells. A fuel cell is a device that converts the chemical energy of a fuel directly into electrical energy via electrocatalytic reactions at an anode and cathode. The fuel cell is a nineteenth century invention. However, no application of fuel cells was reported until the early 1960s. Recently, rising concerns about the energy shortage and the environmental consequences of fossil fuel use have led to a renewed interest in the fuel cell technology. For example, fuel cells are promising candidates as power sources for electric vehicles. Unlike the case of Carnot-limited thermal engines, the free energy change in fuel cell reactions can be converted to

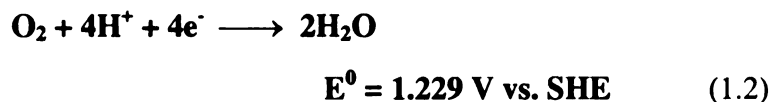
electrical energy (i.e., work) with a theoretical conversion efficiency of over 80%. In addition, the low emission, lack of noise and low cooling requirement are additional attributes.

There are several types of fuel cells under study and they are generally classified according to the type of fuel and electrolyte, operating temperature, or direct or indirect utilization of fuel. Hydrogen and methanol are two favored fuels. Hydrogen is the most electroactive fuel for fuel cells operating at low and intermediate temperatures. Methanol can be considered as a hydrogen carrier in a fuel cell. Conventionally, methanol has been reformed to produce hydrogen. Methanol, however, can be fed directly in to the fuel cell without the intermediate step of reforming. In this case, the fuel cell is called a direct methanol fuel cell (DMFC).

In a DMFC, methanol is oxidized at the anode and oxygen is reduced at the cathode (Figure 1.1A). The two electrodes are separated by an ionic conducting electrolyte, either an aqueous solution or a proton exchange membrane. The direct electrooxidation of methanol in acid media is given by the following reaction⁴



in which CO_2 and protons are formed as products. The protons migrate through the electrolyte and combine with oxygen to produce water at the interface. The electroreduction of oxygen (from air) can be written as



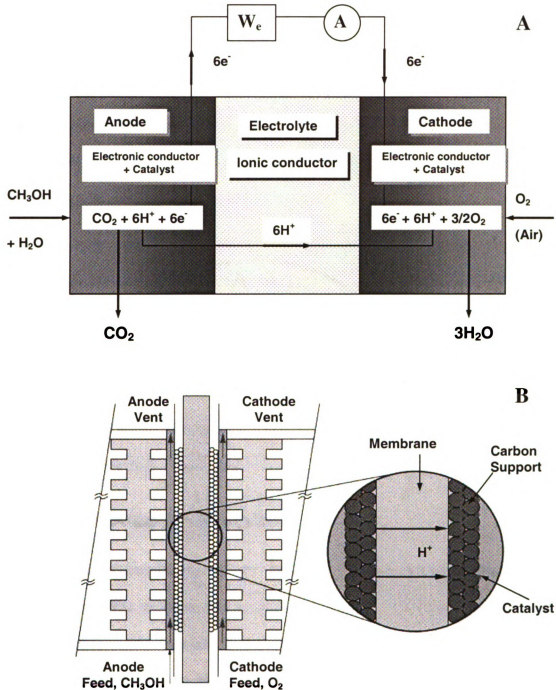


Figure 1.1. (A) Schematic diagram of a direct methanol fuel cell working in an acidic medium. (B) Schematic diagram of a proton exchange membrane fuel cell. Highly-dispersed catalyst (small dots) is supported on carbon black particles (big dots).⁵

The thermodynamic cell voltage of a DMFC is 1.21 V. However, the practical energy conversion efficiency is rather low due to the slow kinetics of both the anodic and cathodic reactions, even with the state-of-the-art electrocatalysts. The catalysts routinely used in low temperature fuel cells are precious metals and their alloys, such as Pt and PtRu.^{6,7} Recently, a number of other catalyst systems have been investigated for methanol oxidation, including the tertiary and higher Pt-based catalyst alloys — PtRuOs,⁸ PtRuSn,⁹ PtRuW,¹⁰ PtRuSnW^{11,12} and PtRuOsIr.¹³

The slow kinetics, scarcity, and expense of noble-metal-based catalysts are driving forces for finding ways to improve the catalytic activity. A high level of activity is achieved by using finely dispersed catalyst, i.e. catalyst with a high specific surface area supported on a high surface-area, electrically conducting material (Figure 1.1B). Carbons and metal oxides are the most favored support materials.¹⁴ Boron carbide, tantalum boride, and silicides of tungsten and titanium have been also reported as catalyst supports due to their high corrosion resistance in aggressive chemical environments.^{15,16}

1.2 Carbon Support Materials

The primary role of the catalyst support is to provide a high surface area over which small metallic particles can be dispersed and stabilized.¹⁷ The porous support should also allow facile mass transport of reactants and products to and from the active sites. Several properties of the support are critical: porosity, pore size distribution, crush strength, surface chemistry, and microstructural and morphological stability.¹⁷

The materials that appear to possess the best combination of these characteristics are carbons. Carbonaceous materials offer microscopic to macroscopic porosity, which

can be readily tailored by controlling the manufacturing conditions, yielding the required pore-size distributions. They also exhibit a chemical inertness, with no metal-support interactions. Additionally, these materials can be burnt off, providing an economical way to recover the precious metal. For electrochemical reactions, the attractive properties of carbon supports are the electrical conductivity and good chemical and electrochemical stability.

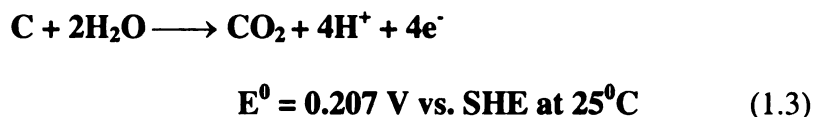
Typical carbon supports include carbon black, graphite, and graphitized carbon black. These materials all contain sp^2 -bonded carbon, but differ significantly from one another in terms of the particle size, porosity, and microstructure. The ideal graphite structure consists of layers of carbon atoms arranged in fused hexagonal rings with an interlayer spacing of 3.354 Å. The parameters of importance are the coherence lengths of the graphite crystallites along a-axis (L_a) parallel and c-axis (L_c) perpendicular to the layer planes. Graphitic allotropes of carbon differ physically from each other in terms of the graphite crystallite dimensions. For example, highly oriented pyrolytic graphite has an L_a larger than 10 μm, whereas L_a for graphite powders can be smaller than 100Å.¹⁸ Carbon blacks are considered to be amorphous carbons, consisting of randomly oriented small graphitic crystallites with values for L_a and L_c in the range of 15 to 25 Å, respectively.¹⁹ Carbon blacks are the most-often-used support materials and are available in a variety of forms. By controlling the manufacturing conditions, carbon blacks can be produced with particle sizes varying from less than 50 Å to greater than 3000 Å, leading to a surface areas ranging from 1000 to 10 m²/g.¹⁹

1.3 The Problem

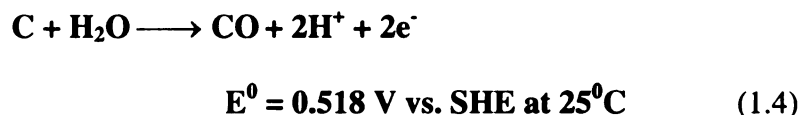
Although sp^2 -bonded carbons have some attractive properties as an electrocatalyst support, a significant limitation of these materials is their susceptibility to corrosion, particularly under the prevailing working conditions of a fuel cell. The corrosion could either be catastrophic causing electrode failure (e.g., CO_2 evolution) or more subtle involving microstructural and morphological alteration that lead to catalyst detachment. Support corrosion may influence the overall electrode performance in several ways. First, electrochemical corrosion of carbon is favored at the cathode operating potential, i.e., 0.6-1.2 V. Carbon oxidation seems to establish a mixed potential at the cathode, thus limiting the cathode working potential. Second, carbon surface oxides formed during the electrochemical oxidation increase the electrical resistance of the carbon support.²⁰ Third, The gasification product, CO, is a poison to Pt-based catalysts, causing decreased catalytic activity. Fourth, limited carbon corrosion causes surface microstructure changes that affect the carbon-metal particle contact, extent of aggregation, the accessibility of the catalyst particles within the support pores (so-called hidden catalyst effect). Fifth, severe carbon corrosion is destructive to the electrode bulk, causing catastrophic mechanical failure.

The importance of support stability has long been recognized. The investigation of electrochemical oxidation of carbon, particularly under the fuel cell operating conditions, can be traced back to the early 1960s. Extensive studies were performed by Binder et al.,²⁰ Kinoshita and Bett,²¹ Stonehart²² and, Gruver.²³ These studies provided important insight into the mechanistic and kinetic aspects of the carbon corrosion process. Carbon corrosion in acidic media occurs by at least two anodic reaction

pathways involving the evolution of gaseous products and the formation of surface oxides. These reactions can be written as ¹⁹



and



Both reactions are thermodynamically favorable, but, in general, kinetically slow. The reaction rate strongly depends on the electrode potential, electrode microstructure, electrolyte composition, and pH. The rate is also affected at a given potential by other factors such as the temperature and vapor pressure. In general, high temperature, high pressure, and high operating potentials result in increased rates of corrosion.

Several approaches have been reported to increase the stability (i.e., corrosion resistance) of carbon support materials. The fact that carbon corrosion generally initiates at surface defect sites and crystallite plane edge sites resulted in the use of heat treatment (graphitization) to reduce the number of surface active sites and thus reduce the corrosion rate.^{24,25} Doping carbon with boron or silicon has been also proposed to enhance the corrosion resistance, as well as to introduce trap sites on the surface that inhibit the catalyst aggregation.²⁶

Considerable efforts have been directed toward the development of alternative support materials. Meilbuhr²⁷ reported that boron carbide might be a useful support for the cathode in the alkaline (KOH) fuel cell. Mckee^{15,16} observed that boron carbide, tantalum boride, and silicides of tungsten and titanium were corrosion-resistant in 85%

H₃PO₄ (150 °C) and 6 N H₂SO₄ (850 °C) and, since these materials have high electrical conductivity, proposed that they might function as electrocatalyst supports. However, the viability of these materials in fuel cells has not been demonstrated.

1.4 Diamond Electrochemistry

Unlike graphite and amorphous carbons, diamond is a carbon allotrope that only recently has begun to be examined as an electrode material for electrochemical technologies. Diamond has long been known for its unique mechanical, thermal, optical, and electrical properties.^{28, and references therein} For example, diamond is extremely hard, inert to corrosive reagents, resistant to radiation damage, and optical transparent in the visible and infrared spectral regions of the electromagnetic spectrum. Historically, the material has been used as an abrasive and as an optical window. Diamond is a wide band gap (5.5 eV) semiconductor with a conduction band close to the vacuum level. Therefore, negative electron affinity is observed for hydrogen-terminated diamond surfaces, making it an excellent choice for field emission devices.²⁹ In addition, diamond is an attractive material for high-temperature, high-frequency and high-power device applications because of its high thermal conductivity (20 Wcm⁻¹ k⁻¹), low dielectric constant (5.5),³⁰ high breakdown field (10⁶-10⁷ Vcm⁻¹), and high electron and hole mobility (2000 cm²V⁻¹s⁻¹ and 1800 cm²V⁻¹s⁻¹).³¹

The R&D activities drastically expanded when chemical vapor deposition (CVD) of diamond became a reality in the early 1970s. CVD affords the possibility of producing diamond thin films on a variety of substrates with relatively low cost. To date, hot-filament and microwave-assisted CVD are the most popular deposition protocols, with a

CH₄/H₂ mixture routinely used as the source gas. Owing to the synthetic nature of diamond growth, it is possible to manipulate the physical and chemical properties of diamond by proper control over the gas composition, system pressure, substrate temperature and reactor design. For example, microcrystalline diamond films, with typical crystallite size range from 1 to 10 μm, can be readily deposited from a hydrogen-rich hydrocarbon environment, whereas nanocrystalline diamond with crystallite sizes in the 10 - 50 nm range, is deposited from a hydrogen-poor environment.³² The methane concentration in the source gas mixture also has a significant impact on diamond nucleation, crystal size, and film composition. Figure 1.2 shows a series of atomic force microscope (AFM) images of films deposited with different CH₄/H₂ ratios. Clearly, as the CH₄/H₂ ratio increases so does the secondary growth rate leading to smaller crystallite size. Also, the films become thicker, more opaque and have higher incidence of non-diamond impurity and other defects with increased CH₄/H₂ ratio. Most importantly, CVD allows for *in situ* doping of a variety of impurities such as boron, phosphorus, and sulfur into the diamond lattice, rendering diamond *p*-type or *n*-type semiconductor properties.³³ Boron is the most prominent dopant because of its small covalent radius, and can be easily incorporated into substitutional sites within the diamond without causing lattice distortion. Boron concentrations in excess of 10²¹cm⁻³ are possible.³⁴

Diamond thin films with sufficient electrical conductivity are attractive electrode materials. The use of diamond in electrochemistry is a relatively new field of research that has begun to blossom in recent years.^{35-38, and references therein} The first paper was published in 1983 by Iwaki et al.,³⁹ but the field was actually initiated by the seminal paper from Pleskov et al..⁴⁰ Boron-doped, hydrogen terminated, polycrystalline diamond

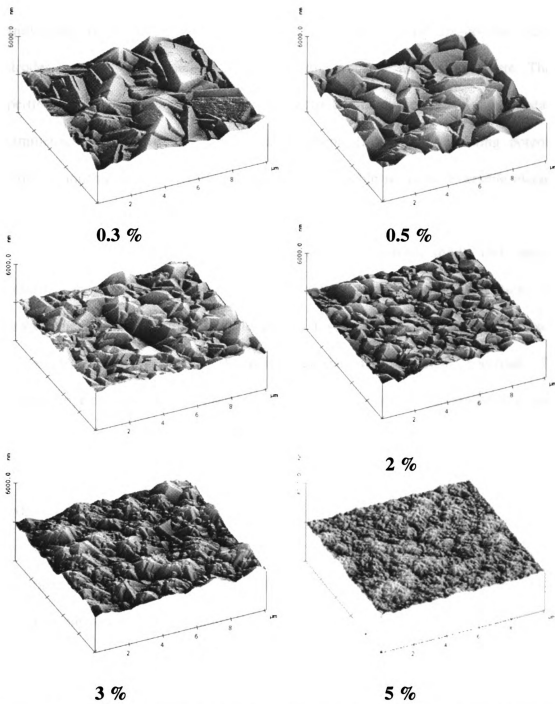


Figure 1.2. Diamond film morphologies as a function of methane-to-hydrogen source gas ratio used during microwave plasma CVD. Hydrogen flow rate is 200 sccm. Growth time is 10 h.

thin films possess a number of important and practical electrochemical properties, unequivocally distinguishing them from other commonly used sp^2 -bonded carbon electrodes, such as glassy carbon (GC), pyrolytic graphite, and carbon paste. These properties are: (i) controllable electrical conductivity via doping; (ii) low and stable voltammetric and amperometric background current; (iii) a wide working potential window in aqueous and nonaqueous media; (iv) reversible to quasi-reversible electron transfer kinetics for several inorganic redox systems without conventional pretreatment; (v) superb morphological and microstructural stability at extreme anodic and cathodic potentials; (vi) weak adsorption of polar molecules from aqueous solution, like anthraquinone-2,6-disulfonate;⁴¹ (vii) long-term response stability; and (viii) optical transparency in the UV/vis and IR regions of the electromagnetic spectrum. The attractive properties of diamond have been exploited a variety of electrochemical technologies including electroanalysis,⁴²⁻⁴⁶ electrocatalysis,⁴⁷⁻⁴⁹ spectroelectrochemistry,⁵⁰ bioelectrochemistry, and electrochemical-based toxic waste-detection and remediation.^{51,52}

The as-deposited diamond surfaces are typically hydrogen-terminated. Chemisorbed hydrogen is critical for stabilizing the structure and prohibiting phase transformations (i.e., graphitization) during growth. The most reproducible electrochemical properties of diamond are observed for the nonpolar and hydrophobic hydrogen-terminated surface. Hydrogen-terminated diamond lacks of surface sites for adsorption and stabilization of reaction intermediates. Therefore, electrochemical reactions that involve adsorbed intermediates or radicals can be strongly hindered on diamond electrode.⁵³ A good example of this is the water discharge reaction that involves

the oxygen and hydrogen evolution reactions, both of which involve multistep processes and formation of reaction intermediates. The suppressed kinetics for both reactions on diamond result in a wide working potential window (3 – 4 V) in aqueous media. This is an attractive feature because it allows electrochemical reactions to be monitored that are screened on other sp^2 -bonded electrodes. For example, zinc electrodeposition ($E^0 = -0.76$ V vs. SHE) can be studied at diamond without severe interference from hydrogen evolution. At the anodic end, aliphatic polyamine oxidation⁴⁶ and halides evolution^{54,55} has been reported. The nonpolar surface shows weak adsorption of polar molecules, leading to improved resistance to electrode deactivation and fouling. The hydrogen-termination also partially contributes to the low double layer capacitance of diamond electrodes, 1 to 8 $\mu\text{F}/\text{cm}^2$, compared to 30–40 $\mu\text{F}/\text{cm}^2$ for glassy carbon. This affords enhanced signal-to-background ratios in electroanalysis due to the low background current and capacitance.

The most striking feature of diamond is its superb corrosion resistance and electrochemical stability. The diamond stability during anodic polarization in acidic fluoride, alkaline, acidic chloride, and neutral chloride media has been investigated. For example, Swain⁵⁶ compared the corrosion resistance of boron-doped diamond, HOPG and glassy carbon (GC) during potential cycling experiments in an acidic fluoride solution at 50 °C. Based on voltammetric, Raman spectroscopic, and capacitance measurements, the morphology and microstructure of diamond were comparatively unchanged by the polarization while severe damage was observed for both HOPG and GC. Katsuki⁵⁷ found that ozone could be generated in H_2SO_4 at boron-doped diamond thin films using a current density from 1 to 10 A/cm^2 . No structural damage of diamond such as pitting, grain roughening, or film delamination, were observed. Chen et al.⁵⁵ carried

out a comparative study of the corrosion resistance of diamond and HOPG for chlorine generation at high anodic current densities. Polycrystalline diamond underwent no gross morphological or microstructural changes at anodic current densities of 0.1 A/cm^2 for 12 plus hours in an acidic chloride media [$E = 3\text{-}4 \text{ V vs. saturated calomel electrode (SCE)}$]. HOPG catastrophically corroded within 30 s under the same conditions.

Figure 1.3 shows a comparison of the surface morphologies of diamond and GC electrode during anodic polarization in an acidic medium as measured by *in situ* AFM. It can be seen diamond undergoes no morphological change during polarization, whereas the GC surface is severely roughened due to the alteration in the surface microstructure and the formation of surface oxide layer. The diamond surface is easily converted to an oxygen-termination during the anodic polarization, but the oxidation is restricted to the surface. The structural and chemical robustness of diamond results from its high atomic density and strong, directional covalent bonding, which inhibit bulk oxidation under all but the most severe conditions (*e.g.*, oxygen plasma treatment). The morphological and microstructural stability contrasts with the severe bulk damage that occurs for many sp^2 -bonded carbon electrodes, which is caused by a combination of intercalation, oxidation, and gasification reactions. Therefore, diamond offers significant improvements in corrosion resistance and dimensional stability compared with more commonly used sp^2 -bonded carbon supports, and can be used in aggressive chemical environments at high temperature and current density, including electrosynthesis, energy conversion devices, and electrochemical-based toxic waste remediation.

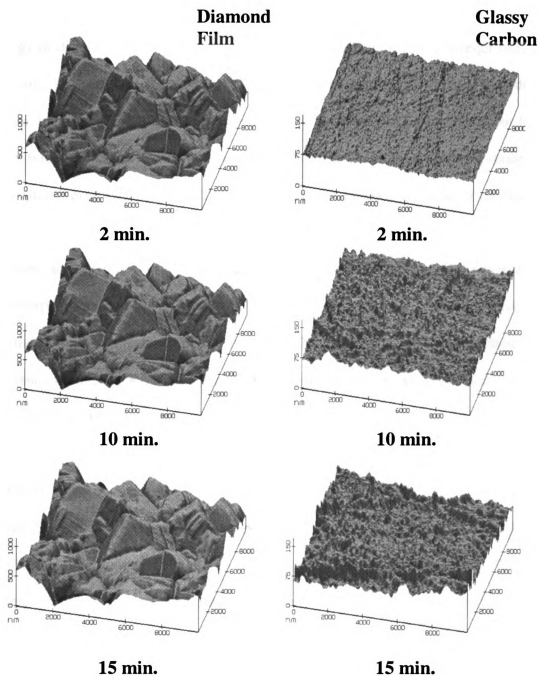


Figure 1.3. The effect of anodic polarization on the electrode morphology. Both the diamond film and glassy carbon electrodes were subjected to polarization at 2 V vs. Ag/AgCl in 0.1 M HClO₄. The *in situ* AFM images were recorded for polarization times 2, 10, and 15 min., respectively.

CVD diamond films are most often polycrystalline because the surface free energy of diamond is high such that the 2D growth of diamond on a foreign substrate is difficult. Furthermore, the covalent C-C bonds in diamond are so rigid that diamond nuclei, individually formed on a substrate, are very unlikely to coalesce without forming grain boundaries.⁵⁸ Certainly, polycrystalline thin films have been the most studied form of diamond electrode, thus far. The electron transfer kinetics at diamond electrodes are influenced by several factors: (i) the dopant type and concentration, (ii) morphological features, such as grain boundaries and extended and point defects, (iii) the non-diamond or amorphous carbon impurity content, (iv) the primary crystallographic orientation, and (v) the surface termination (H, F or O, etc). The degree to which any of these factors influence the electrode response strongly depends on the electrode reaction mechanism for a particular redox analyte.

The boron doping level and uniformity are major factors governing the electrical conductivity of diamond films. Doping levels on the order of 10^{17} to 10^{18} cm^{-3} result in diamond thin films that exhibit semiconducting electronic properties.^{35,40,59} At this level, conduction occurs mainly through holes in the valence band formed the thermal promotion of electrons to empty states of the substitutional boron. The activation energy is rather high (0.37 eV), therefore, only about 0.2 % of the boron sites are ionized at room temperature.³³ At higher doping levels, conduction occurs by nearest neighbor and variable range hopping of holes between ionized sites. This is accompanied by a drop in mobility.³⁴ As very high doping level, 10^{19} cm^{-3} or greater, the overlapping wave functions of nearby acceptor centers leads to band formation, and impurity band conduction takes place.³³ The activation energy for conduction decreases with doping

level as impurity band conduction dominates, and at sufficiently high boron concentrations, the impurity band merges with the valence band leading to metallic conduction. For highly doped films, activation energies as low as 0.002 eV have been reported due to band formation.³³ The boron doping level is also one of the major factors governing the electrode kinetics. Boron doping introduces electronic states within the band gap which mediate the charge transfer across the diamond/electrolyte interface. The density of these states increases with the doping level.

Morphological defects and grain boundaries also affect the electrical conductivity of diamond in a complex manner. On one hand, grain boundary conduction is known to be dominant in undoped and low doped polycrystalline diamond films.⁶⁰ Grain boundaries are a source of disordered sp^2 -bonded carbon, along which variable range hopping occurs.⁶¹ On the other hand, the electrical conduction is inhibited by grain boundaries and other defects at high doping levels because of a reduction in the electron and hole mobilities.⁶² Defects can serve as discrete sites for electron transfer or can simply affect the electronic properties of the material by increasing the density of states. In addition, the grain boundaries could contain nondiamond carbon impurity phases giving rise to additional midgap electronic states and reactive sites.⁵³ Nondiamond impurity is a major factor that affects the electrochemical performance of diamond in terms of the working potential window and background current magnitude, electrode stability, and adsorption.⁶³ Compared with the diamond phase, the nondiamond carbon phase is highly susceptible to oxidation, which introduces oxygen-containing functional groups onto the electrode surface.⁶⁴

1.5 The Motivations

We believe that polycrystalline diamond possesses properties ideally suited for an active material support and current collector for batteries, and an electrocatalyst support for fuel cells and electrosynthesis. The material possesses superior morphological stability and corrosion resistance, compared to conventional sp^2 carbon support materials, being able to withstand current densities on the order of $1 \text{ A}\cdot\text{cm}^{-2}$ for days, in both acidic and alkaline media, without any evidence of structural degradation. The material is chemically inert allowing for its use at elevated temperatures in oxidizing or reducing environments without loss of properties. The thermal conductivity of the material is near that of copper at room temperature, such that diamond might be useful for thermal management purposes. The rough, polycrystalline morphology might also serve to anchor adsorbed metal catalyst particles or active material, leading to improved electrode performance. Metal catalyst particles well anchored into the diamond matrix, rather than just physically sitting on the surface, possess much improved electrode stability and durability. Some of the problems observed with sp^2 -bonded carbon supported catalyst, such as catalyst mobility, aggregation and detachment, particularly when operated at elevated temperature, may be alleviated by incorporating the catalyst particles into the diamond matrix. In addition, the diamond surface is H-terminated so some of the site blocking effects often experienced with O-terminated carbon supports may be minimized. Surface carbon-oxygen functionalities terminating the nearby edge-plane sites of the sp^2 -bonded carbon supports can provide site blocking OH moieties that diminish the Pt catalyst activity.

The synthetic nature of the diamond film growth process, along with the strongly reducing environment (i.e., high flux of atomic hydrogen), allows for the possibility of incorporating foreign metal particles during the deposition. There are several possible ways one might consider incorporating metal impurities into the growing diamond film. We have attempted to incorporate Pt nanoparticles into a diamond matrix by first growing a conductive diamond film, then depositing dispersed Pt particles on top of the conducting diamond, and followed by a secondary diamond film growth around the base of the metal particles. Our ideas for this manner of metal inclusion were stimulated by work performed by two groups. First, Tachibana and coworkers⁵⁸ showed that highly textured diamond films can be grown on Pt(111) substrates. Highly oriented and spontaneously coalesced diamond (111) faces can be grown in so-called “Shintani” growth process. During the course of our electrochemical investigations of this material, we observed that electroactive Pt nanoparticles were serendipitously incorporated into the surface region of the film. This observation led us to try and control the incorporation of such catalyst particles. Second, Callstrom and coworkers⁶⁵ successfully incorporated nanoscale metal clusters into an sp^2 -bonded carbon matrix. Specifically, Pt was incorporated into a “glassy carbon” matrix by low temperature pyrolysis of polymeric precursors.

We expected that the incorporation of metal particles into diamond surface microstructure would result in a conductive, dimensionally stable electrode material containing metal particles of controlled composition, size, and catalytic activity.

1.6 Outline of the Dissertation

This dissertation is devoted to a new research area of diamond electrochemistry: application of boron-doped diamond thin-film electrodes in the field of electrocatalysis. The main focus is on the fabrication and characterization of Pt/diamond composite electrodes and on the investigation of their electrocatalytic activity.

If diamond is going to be effective catalyst support, a fundamental understanding of how metals nucleate, grow, and adhere to the surface is needed. Chapter 2 describes detailed studies of copper electrodeposition on boron-doped diamond thin-film electrodes, in comparison with the sp^2 -bonded carbon electrodes. A unique aspect of the work is the use of *in situ* atomic force microscopy to investigate the shape, spatial distribution, and the nucleation/growth mechanism of the metal deposits. The copper deposition depends strongly on the electronic and chemical properties of the electrode. Hydrogen-terminated diamond exhibits poor interaction with the metal deposits. The size, number density, and spatial distribution of metal deposits are controlled by adjusting the applied overpotential, deposition time, and the electrical conductivity (boron-doping level) of the diamond film.

The methodology for fabricating the metal/diamond composite electrodes is explored in Chapter 3. Our initial attempts to prepare the Pt/diamond composite electrodes by a sequential diamond growth/Pt magnetron sputtering/diamond growth fabrication procedure are described. Nanometer-sized Pt particles can be incorporated into the diamond surface microstructure. The dispersed Pt particles are stabilized by the growth of a thin film of diamond around their base and are in good electrical communication with the current collecting substrate through the boron-doped diamond matrix. Chapter 4 describes a similar multistep fabrication procedure, the difference

being that the dispersion of Pt onto the diamond surface is accomplished by electrodeposition. The size and distribution of Pt particles can be controlled by adjusting the electrodeposition and secondary diamond growth conditions. The composite material is extremely stable with unchanging catalytic activity even after 2 h of anodic polarization in aggressive chemical environments.

It is of specific interest to probe the electrocatalytic activity of the composite electrodes for two important fuel cell electrode reactions: oxygen reduction (cathode) and methanol oxidation (anode). Chapter 5 describes a study of the oxygen reduction reaction kinetics at Pt/diamond composite electrodes. The study focused on the use of rotating disk voltammetry to determine the kinetic parameters for the reaction as a function of the Pt loading and electrolyte composition. Chapter 6 describes a study of the methanol oxidation reaction kinetics at Pt/diamond composite electrodes. The kinetic parameters were determined as a function of the Pt loading, methanol concentration, and catalyst composition. The catalytic activity of the Pt/diamond composite electrodes is comparable to that for polycrystalline Pt. Efforts to prepare the Pt/Ru/diamond composites were made. Preliminary results indicated the electrocatalytic activity for methanol oxidation reaction is greatly enhanced when modifying Pt with Ru.

References:

1. K. Christmann, in *Electrocatalysis*, J. Lipkowski and P. N. Ross, Editors, Wiley-VCH, New York, 1 (1998).
2. W. Grubb, *Nature*, **198**, 883 (1963).
3. A. J. Appleby, in *Comprehensive Treatise of Electrochemistry*, B. E. Conway, J. O. M. Bockris, E. Yeager, S. U. M. Khan and R. E. White, Editors, Plenum Press, New York, **7**, 173 (1983).
4. C. Lamy and J. M. Leger, in *Interfacial Electrochemistry: Theory, Experiment, and Applications*, A. Wieckowski, Editor, Marcel Dekker, New York, 885 (1999).
5. C. Lamy, J. M. Leger, and S. Srinivasan, in *Modern Aspects of Electrochemistry*, R. E. White, Plenum, New York, **34**, 53 (2001).
6. M. Watanabe and S. Motoo, *J. Electroanal. Chem. Interfacial Electrochem.*, **60**, 259 (1975).
7. M. Watanabe and S. Motoo, *J. Electroanal. Chem. Interfacial Electrochem.*, **60**, 267 (1975).
8. K. L. Ley, R. Liu, C. Pu, Q. Fan, N. Leyarowska, C. Segre, and E. S. Smotkin, *J. Electrochem. Soc.*, **144**, 1543 (1997).
9. A. Aramata and M. Masuda, *J. Electrochem. Soc.*, **138**, 1949 (1991).
10. C. He, H. R. Kunz, and J. M. Fenton, *J. Electrochem. Soc.*, **144**, 970 (1997).
11. A. S. Arico, Z. Poltarzewski, H. Kim, A. Morana, N. Giordano, and V. Antonucci, *J. Power Sources*, **55**, 159 (1995).
12. A. S. Arico, P. Creti, N. Giordano, V. Antonucci, P. L. Antonucci, and A. Chuvilin, *J. Appl. Electrochem.*, **26**, 959 (1996).
13. E. Reddington, A. Sapienza, B. Gurrau, R. Viswanathanm, S. Sarangapani, E. S. Smotkin, and T. E. Mallouk, *Science*, **280**, 1735 (1998).
14. K. Kinoshita and P. Stonehart, in *Modern Aspects of Electrochemistry*, R. E. White, Plenum, New York, **12**, 53 (1977).
15. L. W. Niedrach and D. W. Mckee, in *Proceedings of the 21st Annual Power Sources Conference*, May 16-18, 1967, PSC Publications Committee, Red Bank, NJ, 6.

16. W. T. Grubb and D. W. Mckee, *Nature*, **210**, 192 (1966).
17. E. Auer, A. Freund, J. Pietsch, and T. Tacke, *Appl. Catalysis A: General*, **173**, 259 (1998).
18. R. L. McCreery, in *Interfacial Electrochemistry: Theory, Experiment, and Applications*, A. Wieckowski, Editor, Marcel Dekker, New York, 631 (1999).
19. K. Kinoshita, *Carbon: Electrochemical and Physicochemical Properties*, John Wiley & Sons, New York, 22 (1988).
20. H. Binder, A. Kohling, K. Richter, and G. Sandstede, *Electrochim. Acta*, **9**, 255 (1964).
21. K. Kinoshita and J. A. S. Bett, *Carbon*, **11**, 237 (1973).
22. P. Stonehart, *Carbon*, **22**, 423 (1984).
23. G. A. Gruver, *J. Electrochem. Soc.*, **225**, 1719 (1978).
24. J. B. Donnet, P. Ehrburger, and A. Voet, *Carbon*, **10**, 737 (1972).
25. Z. Wei, H. Guo, and Z. Tang, *Journal of Power Sources*, **62**, 233 (1996).
26. P. Stonehart and J. P. MacDonald, *Stability of Acid Fuel Cell Cathode Materials*, Research Project RP 1200-2, Final report for Jan.1, 1978 to May 31, 1984, Prepared for the Electric Power Research Institute, Palo Alto, CA, 1985.
27. S. G. Meilbuhr, *Nature*, **210**, 409 (1966).
28. L. S. G. Plano, in *Diamond: Electronic Properties and Applications*, D. R. Kania, Kluwer Academic Publishers, Norwell, MA, 62 (1995).
29. B. B. Pate, in *Diamond: Electronic Properties and Applications*, L. S. Pan and D. R. Kania, Editors, Kluwer Academic Publishers, Norwell, MA, 45 (1995).
30. C. Chen and S. H. Chen, *Diamond and Related Materials*, **4**, 451 (1995).
31. V. K. Bazhenov, I. M. Viokulin, and A. G. Goonar, *Sov. Phys. Semicond.*, **19**, 829 (1985).
32. D. M. Gruen, *Annual Review of Materials Science*, **29**, 211 (1999).
33. S. Han, L. S. Pan, and D. R. Kania, in *Diamond: Electronic Properties and Applications*, L. S. Pan and D. R. Kania, Editors, Kluwer Academic Publishers, Norwell, MA, 260 (1995).

34. K. Nishimura, K. Das, and G. J. T., *J. Appl. Phys.*, **69**, 3142 (1991).
35. Y. V. Pleskov, *Russian Chemical Reviews*, **68**, 381 (1999).
36. R. Tenne and C. Levy-Clement, *Israel Journal of Chemistry*, **38**, 57 (1998).
37. G. M. Swain, A. B. Anderson, and J. C. Angus, *MRS Bulletin*, **23**, 56 (1998).
38. A. Fujishima and T. N. Rao, *Diamond and Related Materials*, **10**, 1799 (2001).
39. M. Iwaki, S. Sato, K. Takahashi, and H. Sakairi, *Nucl. Instrum. Methods*, **209**, 1129 (1983).
40. Y. V. Pleskov, A. Y. Sakharova, M. D. Krotova, L. L. Builov, and B. V. Spitsyn, *J. Electroanal. Chem. Interfacial Electrochem.*, **228**, 19 (1987).
41. J. Xu, Q. Chen, and G. M. Swain, *Anal. Chem.*, **70**, 3146 (1998).
42. J. Xu and G. M. Swain, *Anal. Chem.*, **70**, 1502 (1998).
43. A. Manivannan, M. S. Seehra, D. A. Tryk, and A. Fujishima, *Anal. Lett.*, **35**, 355 (2002).
44. M. C. Granger, J. Xu, J. W. Strojek, and G. M. Swain, *Anal. Chim. Acta*, **397**, 145 (1999).
45. B. V. Sarada, T. N. Rao, D. A. Tryk, and A. Fujishima, *Proceedings - Electrochemical Society*, **99-32**, 502 (2000).
46. M. A. Witek and G. M. Swain, *Anal. Chim. Acta*, **440**, 119 (2001).
47. J. Wang, G. M. Swain, T. Tachibana, and K. Kobashi, *Proceedings - Electrochemical Society*, **99-32**, 428 (2000).
48. J. Wang, G. M. Swain, T. Tachibana, and K. Kobashi, *Electrochem. Solid-State Lett.*, **3**, 286 (2000).
49. J. Wang, G. M. Swain, T. Tachibana, and K. Kobashi, *J. New Mater. Electrochem. Sys.*, **3**, 75 (2000).
50. J. K. Zak, J. E. Butler, and G. M. Swain, *Anal. Chem.*, **73**, 908 (2001).
51. C. Terashima, T. N. Rao, B. V. Sarada, D. A. Tryk, and A. Fujishima, *Anal. Chem.*, **74**, 895 (2002).

52. T. N. Rao, B. H. Loo, B. V. Sarada, C. Terashima, and A. Fujishima, *Anal. Chem.*, **74**, 1578 (2002).
53. M. C. Granger, M. Witek, J. Xu, J. Wang, M. Hupert, A. Hanks, M. D. Koppang, J. E. Butler, G. Lucazeau, M. Mermoux, J. W. Strojek, and G. M. Swain, *Anal. Chem.*, **72**, 3793 (2000).
54. N. Vinokur, B. Miller, Y. Avyigal, and R. Kalish, *J. Electrochem. Soc.*, **143**, L238 (1996).
55. Q. Chen, M. C. Granger, T. E. Lister, and G. M. Swain, *J. Electrochem. Soc.*, **144**, 3806 (1997).
56. G. M. Swain, *J. Electrochem. Soc.*, **141**, 3382 (1994).
57. N. Katsuki, S. Wakita, Y. Nishiki, T. Shimamune, Y. Akiba, and M. Iida, *Jpn. J. Appl. Phys., Part 2*, **36**, L260 (1997).
58. T. Tachibana, Y. Yokota, K. Miyata, T. Onishi, K. Kobashi, M. Tartutani, Y. Takai, R. Shimizu, and Y. Shintani, *Phys. Rev. B*, **56**, 15967 (1997).
59. C. Reuben, E. Galun, H. Cohen, R. Tenne, R. Kalish, Y. Muraki, K. Hashimoto, A. Fujishima, and J. Butler, *J. Electroanal. Chem.*, **396**, 233 (1995).
60. B. Fiegl, R. Kuhnert, M. Ben-Chorin, and F. Koch, *Appl. Phys. Lett.*, **65**, 371 (1994).
61. Y. Muto, T. Sugino, J. Shirafuji, and K. Kobashi, *Appl. Phys. Lett.*, **59**, 843 (1991).
62. G. A. Sokolina, A. A. Botev, L. L. Builov, S. V. Banysekov, O. I. Lazareva, and A. F. Belyanin, *Sov. Phys. Semicond.*, **24**, 105 (1990).
63. J. Bennett and G. M. Swain, unpublished results.
64. H. B. Martin, A. Argoitia, J. C. Angus, and U. Landau, *J. Electrochem. Soc.*, **146**, 2959 (1999).
65. M. R. Callstrom, T. X. Neenan, R. L. McCreery, and D. C. Alsmeyer, *J. Am. Chem. Soc.*, **112**, 4955 (1990).

Chapter 2

Electrochemical and *in situ* Atomic Force Microscopic Studies of Copper Deposition on Boron-Doped Diamond Thin-Film Electrodes

2.1 Introduction

There has been a growing interest over the years in the fundamental understanding of the electrochemical properties of boron-doped diamond thin films.¹⁻⁴, and references therein Such interest has resulted from the promising applications of diamond in the field of electroanalysis, electrosynthesis, electrocatalysis, and electrochemical-based toxic waste remediation. Diamond is also an interesting electrode material for fundamental research, including the study of electron-transfer processes at the electrode/electrolyte interface. In contrast to many other carbon-based (e.g. glassy carbon (GC) and highly oriented pyrolytic graphite (HOPG)) and metal electrodes, diamond does not form a significant interfacial (oxide) layer when brought to contact with an aqueous solution. Moreover, it does not undergo microstructure alteration over a wide potential range.

A significant motivation of previous and current research is the need to develop a predictive understanding of the structure-reactivity relationship of boron-doped diamond thin-film electrodes. We have established a multistep electrochemical characterization protocol to assess diamond electrode responsiveness.⁵⁻⁸ Our goal is to correlate the physical, chemical, and electronic properties of the material with its electrochemical responsiveness. Several electrochemical probes are routinely employed to characterize

the electrodes, including $\text{Fe}(\text{CN})_6^{-3/-4}$, $\text{Ru}(\text{NH}_3)_6^{+3/+2}$, methyl viologen ($\text{MV}^{+2/+0}$), $\text{Fe}^{+3/+2}$, catechols, and oxygen reduction. These redox systems are used because each is sensitive to different physicochemical properties, and their formal potentials span a wide potential range ($\sim +1.1$ to -0.8 V vs. SHE).⁷

Metal electrodeposition is another type of surface “sensitive” charge-transfer process that can be used to probe the reactivity of diamond electrodes. The original metal deposition work on diamond was conducted by Awada et al., in which they demonstrated that Pt, Pb, and Hg were readily deposited on a diamond surface.⁹ Moreover, metal deposition on diamond electrodes is of great practical significance because (i) electrodeposition allows for fabrication of various passive and active electrical contacts on the diamond surface, as metallization processes will be indispensable for establishing electronic devices based on diamond technology;³ (ii) it is the groundwork for developing diamond-based anodic stripping voltammetric detection of heavy metal ions; and (iii) surface roughness, corrosion resistance and chemical stability of polycrystalline diamond films combined with the catalytic activity of metal adlayers afford the possibility of developing an advanced class of highly sensitive and stable electrocatalytic surfaces. For these reasons, electrodeposition of Ag,¹⁰ Hg,^{10,11} Pt,¹² Pb¹³ and Cu¹⁴⁻¹⁶ on boron-doped diamond electrodes has been recently reported.

We present herein the first detailed investigation of copper electrodeposition on diamond electrodes using a combination of electrochemical and microscopic techniques. The study was aimed at elucidating (i) the mechanism of metal nucleation on diamond, (ii) the structure-reactivity relationship at diamond by examining metal nucleation and growth, and (iii) the capability of diamond serving as a support/host for electrocatalytic

metal particles. Copper electrodeposition was examined on diamond films with different boron-doping levels and the results were compared with those obtained for GC and HOPG. The diamond films used had a boron doping level ca. 10^{19} and 10^{21} cm^{-3} , which are referred to as low boron-doped diamond (LBD) and highly boron-doped diamond (HBD), respectively. The nucleation mechanism (progressive vs. instantaneous nucleation) was studied by examining initial stages of copper deposition with cyclic voltammetry (CV) and chronoamperometry. Electrochemical atomic force microscope (ECAFM) was used to *in situ* monitor the new phase formation on diamond during deposition. The location and shape of the metal deposits provide important information regarding the spatial reactivity (grain boundary vs. grain reactivity) of the diamond electrodes. The nucleation mechanism revealed by ECAFM was in good agreement with the electrochemical data.

2.2 Experimental

Electrode preparation. Boron-doped diamond thin films were deposited on p-Si(100) substrates using microwave-assisted chemical vapor deposition (CVD) (Kobe Steel Ltd., Japan). A summary of the growth conditions is shown in Table 2.1. The substrates were 0.1 cm thick and 1 cm^2 in area. The source gas used was a CH_4/H_2 mixture with a CH_4 concentration of 0.2-0.6 %. The gas pressure was 50 torr, and the microwave power was 0.8-1 kW. The substrate temperature was about 875 $^\circ\text{C}$. The boron dopant source was B_2H_6 and the boron-doping was controlled by adjusting the volumetric ratio of B_2H_6 in the source gas. The boron dopant concentrations were estimated to be approximately 10^{19} to 10^{21} B/cm^3 (in the film), based on the secondary ion mass

spectrometry analysis of other films deposited using similar conditions. The apparent in-plane film resistivities ranged from 0.1 to 0.01 Ω -cm, and were measured using a tungsten four-point probe with the diamond film attached to the conducting Si substrate.

Table 2.1. Summary of the diamond thin-film deposition parameters.

Substrate	p-Si (100)
CH ₄ /H ₂ (v/v) ratio	0.2-0.6 %
Microwave power	0.8-1 kW
Deposition pressure	50 torr
Deposition time	20 hrs
Substrate temperature	875 °C
Boron dopant source	B ₂ H ₆
Doping level (in film)	10 ¹⁹ -10 ²¹ cm ⁻³

Glassy carbon (1 cm², GC-30, Tokai Ltd., Japan) was prepared by polishing on separate felt pads with successively smaller grades of alumina powder slurried in ultrapure water (1.0, 0.3, and 0.05 μ m). The electrode was rinsed thoroughly with and ultrasonicated for 5 min. in ultrapure water after each polishing step. A fresh basal plane of HOPG (Advanced Ceramics Corp., USA) was exposed by cleaving the topmost layers with scotch tape. This cleaving process leaves a variable amount of adventitious defects on the surface.

Electrochemical measurements. The cyclic voltammetric and chronoamperometric measurements were performed in a single compartment glass cell using a CYSY-2000 digital potentiostat (Cypress Systems, Inc., Lawrence, KS). Figure 2.1 shows a diagram of the cell. A commercial saturated calomel electrode (SCE) was used as the

reference and a large area carbon rod served as the counter electrode. The diamond film electrodes were pressed against the bottom of the glass cell with the fluid being contained by a Viton O-ring. The geometric area exposed was 0.2 cm^2 and all currents were normalized to this area. The large area counter electrode was positioned parallel to the working electrode. The reference electrode was positioned near the working electrode using a glass capillary that was filled with 50 mM H_2SO_4 . The end of the capillary was cracked to allow for ion conduction. Electrical connection was made to the diamond in one of three ways with each method generally providing similar results: (i) scratching the backside of the Si substrate with a diamond scribe and then coating the area with graphite before contacting the Al current collecting backplate, (ii) same as above but coating the area with Ag paste, or (iii) same as above but running a bead of Ag paste from the top edge of the diamond film to the backside of the Si substrate. The Al plate was polished clean prior to use. Care must be taken to avoid solution leakage which can cause formation of salt deposits on the backside of the Si substrate and impede good contact with the current collecting plate. Sometimes, an In/Ga eutectic was used to make ohmic contact to the backside of the scratched Si substrate. All measurements were made at room temperature with solution deoxygenation by a nitrogen purge gas. The diamond film working electrodes were pretreated, once mounted in the cell, by a thorough rinsing with ultrapure water ($>17 \text{ M}\Omega\text{-cm}$, Barnstead Nanopure), a 20 min. soak in distilled isopropanol, followed by another thorough rinsing with ultrapure water. Isopropanol can be an effective cleaning agent for sp^2 -bonded carbon electrodes.¹³ A three-step cleaning procedure was used for all glassware: washing in a KOH/methanol bath, washing in a liquid detergent/water bath (Alconox, Inc.) and rinsing with ultrapure water.

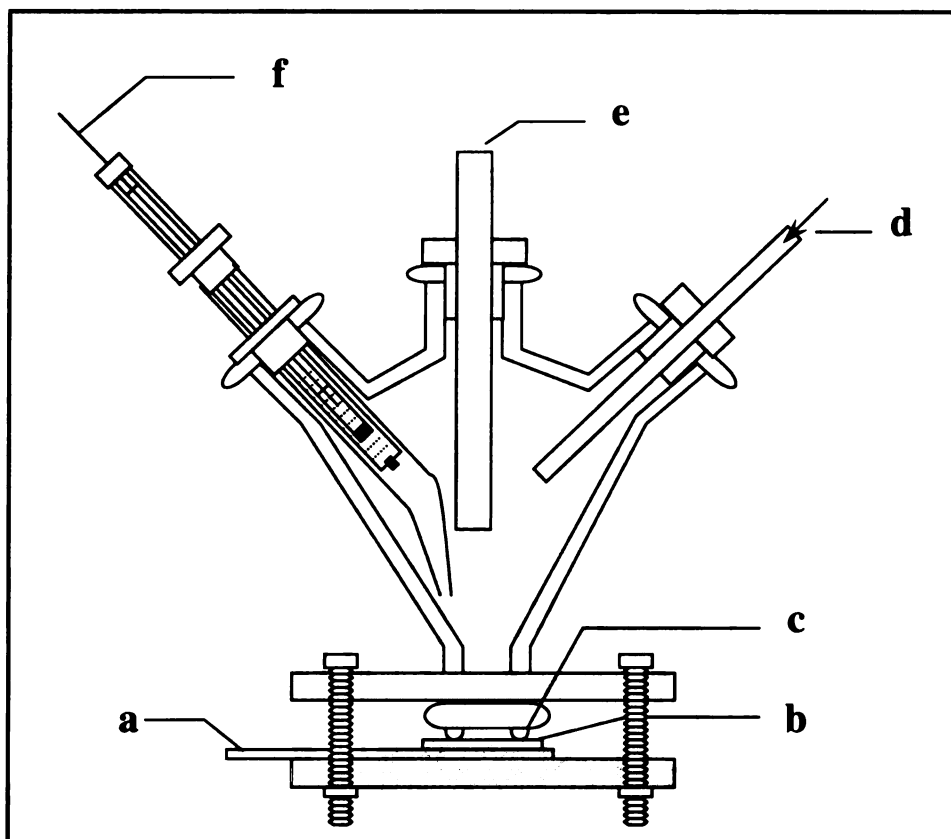


Figure 2.1. Diagram of the single-compartment, glass electrochemical cell. (a) Cu or Al metal current collecting back plate, (b) working electrode, (c) Viton O-ring, (d) input for nitrogen purge gas, (e) carbon rod or Pt counter electrode, and (f) reference electrode inside a glass capillary tube with a cracked tip.

ECAFM measurements. The ECAFM images were acquired using Nanoscope II atomic force microscope (Digital Instruments Inc., Santa Barbara, CA) equipped with a standard ECAFM fluid cell. Figure 2.2 shows the diagram of the fluid cell. The cell has tapered channels for allowing the flow of the electrolyte and also the insertion of auxiliary and reference electrodes. Both were platinum wires. The fluid cell was sealed

by pressing the working electrode against the bottom of the cell, isolated by a Viton O-ring. The exposed surface area of the electrode was 0.38 cm^2 . A pyramidal Si_3N_4 45° tip, mounted on a gold-coated $100\mu\text{m}$ v-shaped silicon nitride cantilever (0.38 N/m spring constant), was used for imaging. The tip was held in an optically transparent holder in the fluid cell. The AFM was operated in the contact mode.

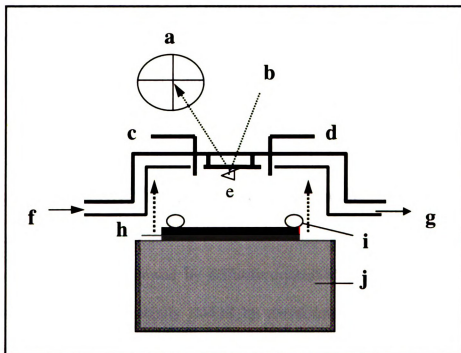


Figure 2.2. Diagram of the ECAFM fluid cell. (a) photodetector, (b) He-Ne laser, (c) auxiliary electrode, (d) reference electrode, (e) tip, (f) solution inlet, (g) solution outlet, (h) working electrode, (i) O-ring, and (j) piezoscanner.

ECAFM images were obtained in either the height mode, in which the tip height was adjusted via a feedback mechanism so as to maintain the force constant, or force mode in which the tip height was kept constant so as to measure the force. A potentiostat

was used to perform the potential cycling or potential step measurements. In ECAFM, all potentials were recorded against the Pt quasi-reference electrode. The potential difference between Pt and SCE electrode was ca. 0.3 V in 50 mM H₂SO₄. For convenience, all potentials are reported, here after, converted to the SCE reference scale. All the images were recorded with 400 × 400 pixels. All measurements were made at room temperature.

Chemicals. The CuSO₄·5H₂O was reagent grade quality (Fisher Scientific) and the H₂SO₄ acid electrolyte was ultrahigh purity grade (99.999%) (Aldrich). Ultrapure water (>17MΩ·cm) from a Barnstead E-pure system was used to prepare the solutions, clean the glassware and rinse all electrodes.

2.3 Theories of Metal Nucleation and Growth

The early stages of electrochemical phase transformations are usually associated with 3-D nucleation process followed by diffusion-controlled growth of the mature nuclei.¹⁷ These processes are generally studied by chronoamperometry, in which the electrode potential is stepped to a value cathodic enough to cause diffusion-controlled metal deposition, and then the potentiostatic current-time transient is recorded. Reliable information regarding the number density of nuclei on the surface, nucleation rate, and nucleation mechanism can be obtained from the analysis of the current transient.

The nucleation/growth during the early stages of deposition is illustrated in Figure 3.3A.¹⁷ A number of hemispherical nuclei are randomly formed on the electrode surface at short times after the potential step. Because of their small size and isolation, the growth is described in terms of localized spherical diffusion to individual microelectrodes. This corresponds to the rising part of the current transient (see Figure 3.3B). As the radius of

the growth center increases and the hemispherical diffusion zones of various nuclei begin to overlap, the hemispherical diffusion gives way to linear diffusion to a planar electrode surface.¹⁷ Consequently, the current reaches a maximum and then decays at a $t^{-1/2}$ rate as predicted from the Cottrell equation. Such a 3D nucleation/growth mechanism has been described in several theoretical models.^{17,18}

In the approach of Scharifker and Hills,¹⁷ nucleation is classified as either “instantaneous”, in which rapid nucleation takes place on a fix number of active sites, or “progressive”, in which the number of nuclei increases with time and the number of active sites available for nucleation are considered to be virtually infinite.

For instantaneous nucleation, the current density is given by

$$i = \frac{nFD^{1/2}c}{\pi^{1/2}t^{1/2}} [1 - \exp(-N\pi kDt)] \quad (2.1)$$

where D is the diffusion coefficient, c is the bulk concentration of metal ions, nF is the molar charge transferred during electrodeposition, and k is

$$k = (8\pi cM / \rho)^{1/2} \quad (2.2)$$

where M and ρ are the molecular weight and density of the deposited metal, respectively.

For progressive nucleation, the current density is given by

$$i = \frac{nFD^{1/2}c}{\pi^{1/2}t^{1/2}} [1 - \exp(-AN_0\pi k'Dt^2 / 2)] \quad (2.3)$$

and

$$k' = \frac{4}{3}(8\pi cM / \rho)^{1/2} \quad (2.4)$$

where N_0 is the number density of active sites over the substrate surface, A is the nucleation rate constant per site.

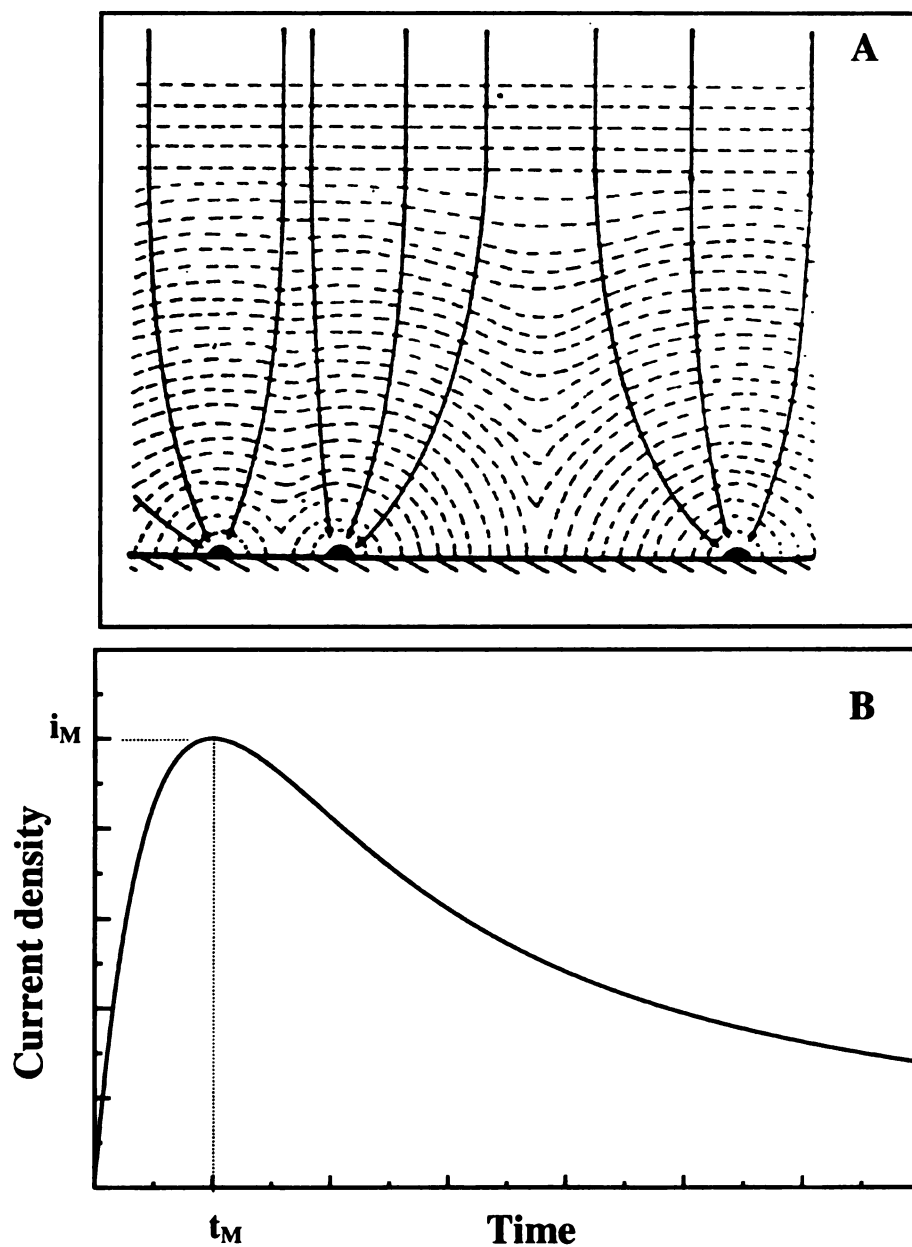


Figure 2.3. (A) Schematic representation of the growth of the diffusion zones and their eventual overlap. The arrows indicate the directions of the diffusional field during the growth of the nuclei. (B) Typical current-time transient recorded during the potential step after background correction.

For convenient analysis, the transients are generally presented in dimensionless form by plotting $(i/i_M)^2$ vs. t/t_M , where i_M and t_M are the current and the time at the maximum, as in Figure 2.3B. They are

$$\left(\frac{i}{i_M}\right)^2 = 1.9542 \left(\frac{t}{t_M}\right)^{-1} \left\{ 1 - \exp \left[-1.2564 \left(\frac{t}{t_M}\right) \right] \right\}^2 \quad (2.5)$$

$$\left(\frac{i}{i_M}\right)^2 = 1.2254 \left(\frac{t}{t_M}\right)^{-1} \left\{ 1 - \exp \left[-2.3367 \left(\frac{t}{t_M}\right)^2 \right] \right\}^2 \quad (2.6)$$

for instantaneous and progressive nucleation, respectively.

In the approach of Scharifker and Mostany,¹⁸ it is not necessary to classify the nucleation process as instantaneous or progressive, since these cases appear as the extremes of a more general mechanism. The entire current transient can be expressed as

$$i = \frac{nFD^{1/2}c}{\pi^{1/2}t^{1/2}} \left[1 - \exp \left\{ -N_0\pi kD \left[t - \frac{(1 - \exp(-At))}{A} \right] \right\} \right] \quad (2.7)$$

The dimensionless form is

$$\left(\frac{i}{i_M}\right)^2 = \left(\frac{t}{t_M}\right)^{-1} \frac{\left\{ 1 - \exp \left[-x \frac{t}{t_M} + \alpha \left[1 - \exp \left(-\left(\frac{x}{\alpha}\right) \frac{t}{t_M} \right) \right] \right] \right\}^2}{\left\{ 1 - \exp \left[-x + \alpha \left[1 - \exp \left(-\frac{x}{\alpha} \right) \right] \right] \right\}^2} \quad (2.8)$$

where $x = N_0\pi kDt_M$, and $\alpha = N_0\pi kD/A$. In this approach, the A and N_0 can be calculated separately.

In this work, we analyze the experimental results according to both approaches. The nucleation mechanism of copper on diamond surface is illustrated by the first

approach, and the potential dependence of the nucleation rate and number density of active sites are determined by the second approach.

2.4 Results

2.4.1 Electrochemical Study of Copper Deposition

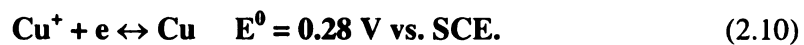
Cyclic voltammetry. The electrodeposition of copper on a low (LBD) and highly (HBD) boron-doped diamond, as well as HOPG and GC, was initially studied by cyclic voltammetry. Figure 2.4 shows the voltammetric *i*-*E* curves recorded in N₂-purged 1 mM CuSO₄ + 50 mM H₂SO₄. The potential sweep was initiated at 0.4 V and scanned in the negative direction at a scan rate of 20 mV/s. Each *i*-*E* curve represents the first sweep. The overall reaction is¹⁹



A summary of the voltammetric data is shown in Table 2.2.

The voltammograms exhibit the characteristic features of nucleation and growth phenomena, particularly for LBD and HOPG, i.e., the large negative shift of the reduction peak potential and the current crossover during the reverse scan. The equilibrium potential, E_{eq} , for Reaction (2.9) in 1 mM CuSO₄, is ca. 10 mV vs. SCE, as calculated from the Nernst equation. Therefore, the overpotential needed to initiate the formation of the bulk metal phase ranges from -110 to -240 mV, and increases in the order GC < HBD < LBD < HOPG. No current crossovers, however, were observed in the *i*-*E* curves for GC and HBD. Rather, the cathodic process most likely proceeds in two steps. In both cases, discernible cathodic current starts at ca. 70 mV, leading to the formation of a

shoulder peak prior to the steep rise of the current. The shoulder peak is presumably due to the reduction of trace amount of Cu^+ . The reaction can be written as²⁰



which occurs at more positive potential.

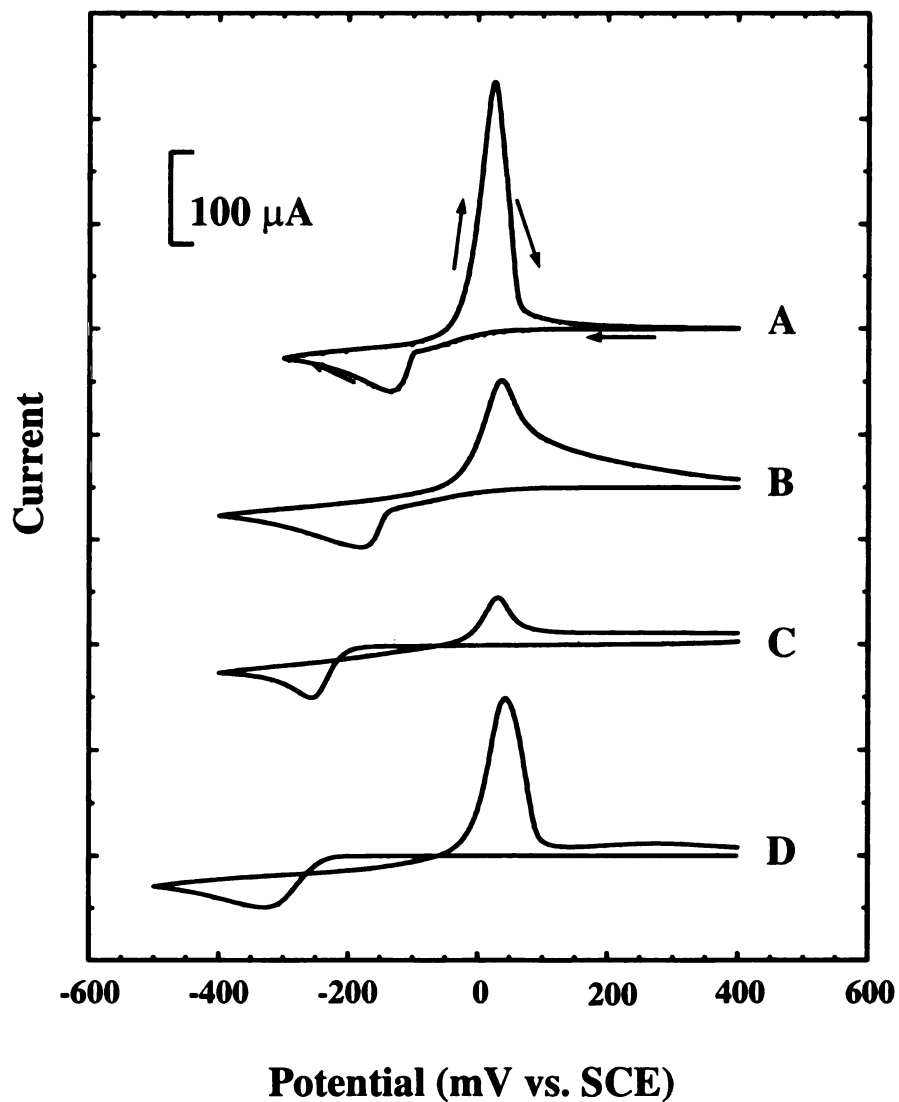


Figure 2.4. Cyclic voltammetric *i*-*E* curves for copper deposition on (A) GC, (B) HBD, (C) LBD, and (D) HOPG in 1 mM CuSO_4 + 50 mM H_2SO_4 . Scan rate = 20 mV/s.

Table 2.2. CV data for copper electrodeposition on different electrodes in 1 mM CuSO₄ + 50 mM H₂SO₄.

Electrode	Onset reduction potential ^a (mV)	i_p^{red} (μA)	E_p^{red} (mV)	E_p^{ox} (mV)	ΔE_p (mV)	$Q_{\text{ox}}/Q_{\text{red}}$
GC	-100	-57.6	-132	26	158	0.94
HBD	-138	-55.2	-180	36	216	0.90
LBD	-185	-50.3	-255	31	286	0.73
HOPG	-230	-46.2	-320	43	363	0.85

a. Onset reduction potentials for Reaction 2.9.

The voltammetric data for all four electrodes are shown in Table 2.2. The onset reduction potential for copper deposition is greatest for HOPG and least for GC. The two diamond films have values in between. The reduction peak current for each electrode increased linearly with the square root of scan rate ($r^2 = 0.998$) over the range from 20 to 200 mV/s, suggestive of a diffusion-controlled process. In contrast, the oxidation peak current increased rather linearly with the scan rate ($r^2 = 0.992$), indicative of a surface-confined process. Very broad oxidation peaks are observed for both diamond surfaces in contrast to that for GC, which are most likely attributed to the heterogeneity of both the diamond surface structure and electronic properties. Similar results were obtained for Ag and Hg deposition on diamond.¹⁰ In addition to the broad stripping peaks, the anodic currents were observable at potentials positive of the equilibrium value. Integration of the

areas under both anodic and cathodic peaks, after background subtraction, yields the oxidation and reduction charge. As shown in Table 2.2, the anodic stripping charge is ca. 10-25% lower than the cathodic deposition charge, indicating that the copper deposits do not completely strip during the anodic scan, at least during the time scale of the measurement. Indeed, some residual copper particles were detected on the LBD surface in the ECAFM study, as described below.

It should be noted that copper deposits weakly adhere to the diamond surface, a phenomenon that has been observed in the case of Pb,⁹ Ag and Hg¹⁰ electrodeposition on diamond. The deposits can be easily dislodged by the turbulence of solution mixing. The weak deposit-substrate interaction is attributed to the low activity of hydrogen-terminated diamond surface.¹⁴

Chronoamperometry. Single-step chronoamperometric measurements were carried out to investigate the metal nucleation/growth process in greater detail. Figure 2.5 presents a set of current-time transients for copper deposition on LBD from 1 mM CuSO₄ + 50 mM H₂SO₄. The measurements were performed by stepping the potential from 0.5 V, where copper was not deposited, to different final potentials, E_f , sufficiently cathodic to induce nucleation and subsequent crystallite growth. Note the potentials shown in Figure 2.5 are overpotentials, $\eta = E_f - E_{eq}$. The working electrode was poised at a positive potential of 0.6 V for 5 min after each step in order to completely oxidize the copper deposits. This led to a good reproducibility of consecutive measurements performed under the same conditions.

The current increases immediately after the application of the potential step and decreases at very short times, as the electrode double layer fully charges. The current then

increases as a result of the formation of stable nuclei and growth of the metal deposits. As the individual hemispherical diffusion zones of the growing crystallites coalesce, the current passes a maximum, i_M , then decays at a $t^{-1/2}$ rate predicted from Cottrell equation. The values of i_M and t_M , the time at which i_M occurs, are listed in Table 2.3.

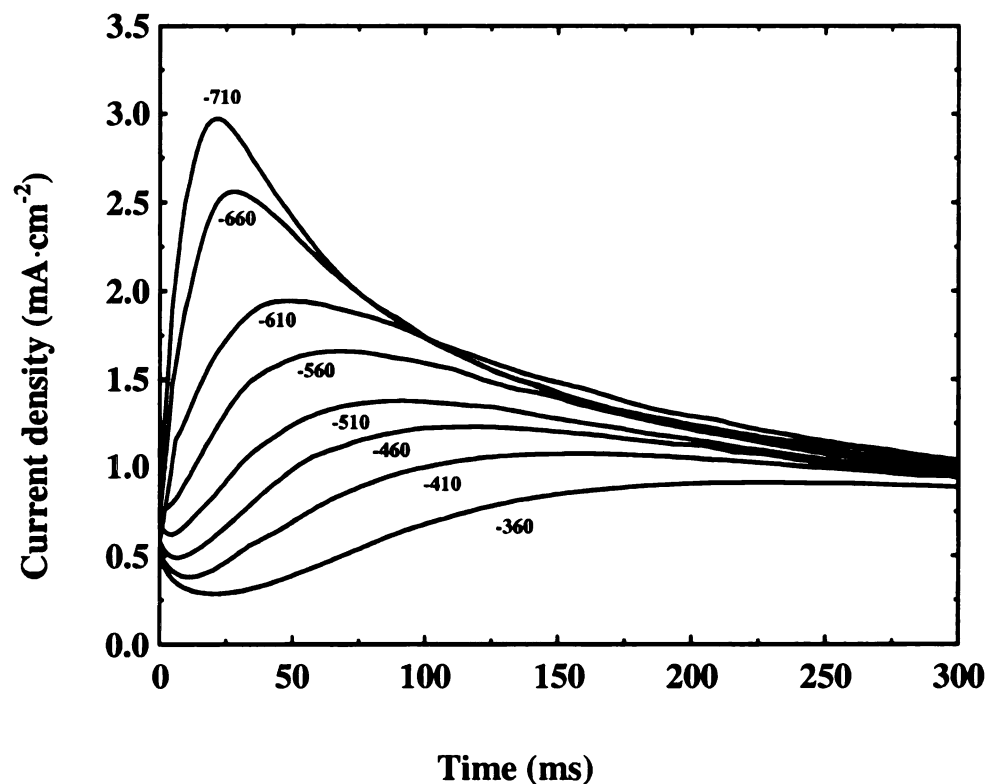


Figure 2.5. Potentiostatic current-time transients for copper deposition on LBD in 1 mM CuSO_4 + 50 mM H_2SO_4 at the overpotentials indicated in mV.

Analysis of the current transients and classifying the nucleation process. The current-time transients were initially analyzed according to Scharifker and Hills' approach, i.e., to classify the nucleation process as "instantaneous" or "progressive". Figure 2.6 shows some examples of the experimental data (dashed curves) in comparison

with the theoretical curves (solid curve a for instantaneous and b for progressive nucleation). The theoretical curves are constructed by plotting $(i/i_M)^2$ vs. t/t_M according with Equation 2.5 and 2.6. The actual experimental data without background correction are also presented (dashed line) in the dimensionless plots. The fit for any of the experimental curves with entire the instantaneous or progressive curves is not perfect, but the data do tend to more closely match one limiting case or the other at all potentials. The deviation from the limiting situations is a typical phenomenon for heterogeneous nucleation on a finite number of active sites on the surface.²¹ The nucleation of copper on LBD appears to follow an instantaneous nucleation mechanism at low overpotentials ($|\eta| < 610$ mV), and a progressive mechanism at high overpotentials, ($|\eta| > 610$ mV).

The chronoamperometric measurements were also performed on HBD, GC and HOPG. The current-time transients for copper deposition on HBD are shown in Figure 2.7. The i_M increases and t_M decreases with increased boron doping level (i.e., the conductivity of the diamond film). The comparisons of the experimental current-time transients with the theoretical curves are shown in Figure 2.8. The experimental data deviate from both limiting cases, but follow closely the response predicted for progressive nucleation at both low (-410 mV) and high overpotentials (-610 mV).

Analysis of the current transients without classifying the nucleation process. In Scharifker and Mostany's approach, it is not necessary to classify the nucleation process as one of the two limiting cases. The parameters A and N_0 can be estimated separately from a single point of the experimental transients, such as the current maximum, or by nonlinear fitting of the entire current-time transients to the theoretical expression

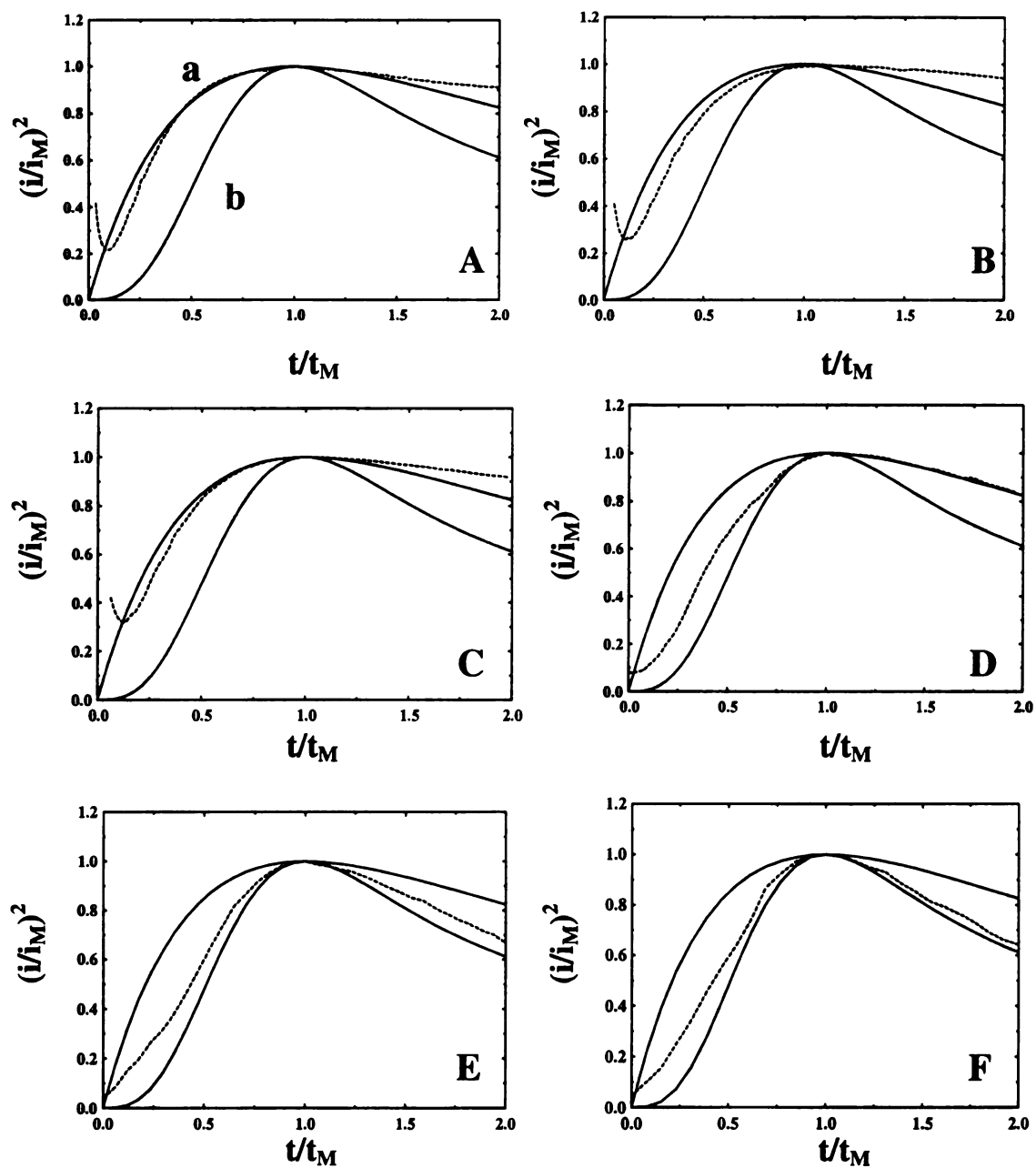


Figure 2.6. Comparison of experimental current-time transients (dash curves) for LBD (see Figure 2.5) with the theoretical transients corresponding to instantaneous (solid curve a) and progressive (solid curve b) nucleation at different overpotentials: (A) -410 , (B) -460 , (C) -510 , (D) -610 , (E) -660 , and (F) -710 mV.

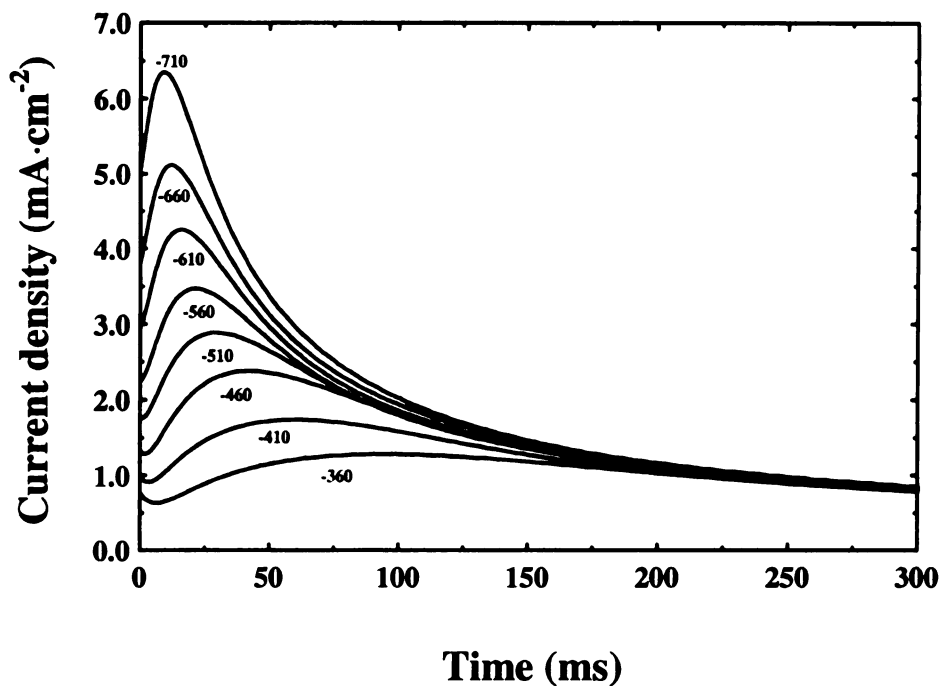


Figure 2.7. Potentiostatic current-time transients for copper deposition on HBD in 1 mM CuSO_4 + 50 mM H_2SO_4 at the overpotentials indicated in mV.

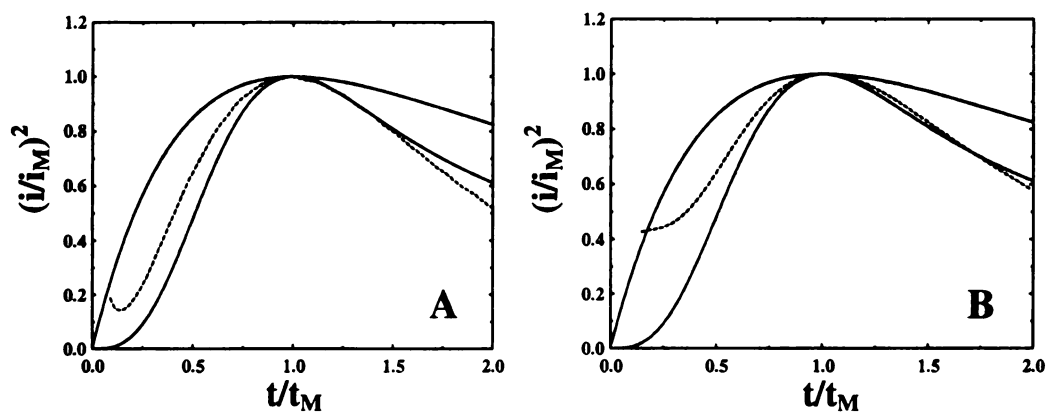


Figure 2.8. Comparison of experimental current-time transients (dashed curves) for HBD (see Figure 2.7) with the theoretical transients corresponding to instantaneous (solid curve a) and progressive (solid curve b) nucleation at overpotentials of (A) -410 and (B) -610 mV.

Table 2.3. Current-time transient data for copper electrodeposition on LBD.

$-\eta$ (mV)	i_M (mA·cm ⁻²)	t_M (s)	$i_M t_M^{1/2} / a$	$10^{-7} N_0$ (cm ⁻²)	A (s ⁻¹)	$10^{-7} N_s$ (cm ⁻²)
360	0.913	0.226	0.7890	0.82	26.9	—
410	1.075	0.165	0.7953	1.17	31.9	—
460	1.232	0.128	0.8027	1.58	37.1	—
510	1.375	0.105	0.8081	2.02	41.7	—
560	1.660	0.073	0.8155	3.06	53.4	4.28
610	1.961	0.054	0.8285	4.63	59.2	5.54
660	2.567	0.033	0.8463	9.15	71.7	8.57
710	2.970	0.025	0.8620	14.3	80.7	11.4

Table 2.4. Current-time transient data for copper electrodeposition on HBD.

$-\eta$ (mV)	i_M (mA·cm ⁻²)	t_M (s)	$i_M t_M^{1/2} / a$	$10^{-8} N_0$ (cm ⁻²)	A (s ⁻¹)	$10^{-8} N_s$ (cm ⁻²)
360	1.280	0.127	0.8007	0.14	37.9	0.24
410	1.742	0.074	0.8297	0.30	42.2	0.38
460	2.382	0.042	0.8498	0.66	53.0	0.63
510	2.896	0.029	0.8608	1.13	60.2	0.87
560	3.481	0.020	0.8706	1.94	65.3	1.19
610	4.250	0.014	0.8807	3.70	69.0	1.69
660	5.167	0.010	0.8848	6.47	79.7	2.40

Table 2.5. Current-time transient data for copper electrodeposition on HOPG.

$-\eta$ (mV)	i_M (mA·cm ⁻²)	t_M (s)	$i_M t_M^{1/2} / a$	$10^{-7} N_0$ (cm ⁻²)	A (s ⁻¹)	$10^{-7} N_s$ (cm ⁻²)
360	0.557	0.652	0.7491	0.18	20.8	—
410	0.795	0.340	0.7729	0.40	22.7	—
460	1.098	0.190	0.7980	0.83	26.7	—
510	1.415	0.120	0.8172	1.51	31.8	—
560	1.884	0.070	0.8324	2.94	42.7	3.75
610	2.201	0.052	0.8383	4.20	52.0	4.94
660	2.555	0.039	0.8410	5.79	66.4	6.56
710	2.927	0.030	0.8450	7.89	80.4	8.42

Table 2.6. Current-time transient data for copper electrodeposition on GC.

$-\eta$ (mV)	i_M (mA·cm ⁻²)	t_M (s)	$i_M t_M^{1/2} / a$	$10^{-8} N_0$ (cm ⁻²)	A (s ⁻¹)	$10^{-8} N_s$ (cm ⁻²)
360	2.680	0.044	0.8589	0.59	61.4	0.64
410	3.127	0.033	0.8679	0.94	65.2	0.83
460	3.545	0.026	0.8734	1.36	70.7	1.04
510	4.070	0.020	0.8794	2.09	72.5	1.30
560	4.570	0.016	0.8832	3.02	77.5	1.62
610	5.103	0.013	0.8855	4.13	86.1	1.99
660	5.877	0.010	0.8888	6.54	90.8	2.58

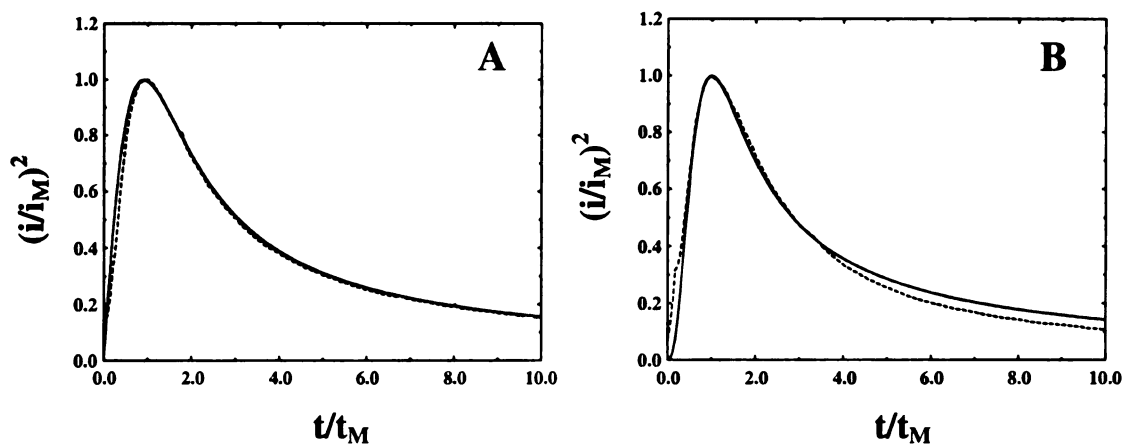


Figure 2.9. Comparison of experimental current-time transients (dashed curves) with the theoretical transients according to Equation 2.8 for copper deposition on LBD at overpotentials of (A) -410 and (B) -610 mV.

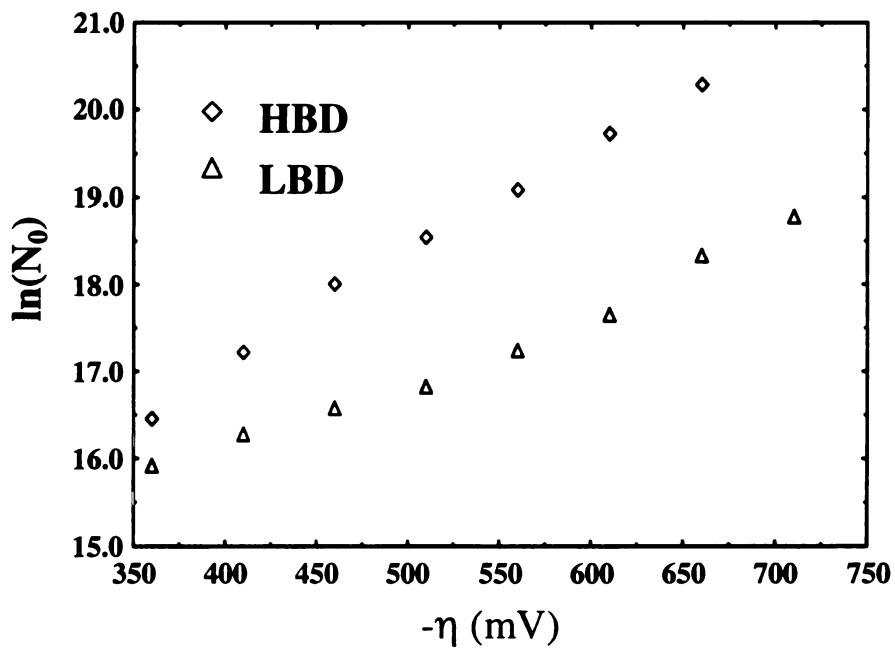


Figure 2.10. Plot of the logarithm of the number density of active sites vs. overpotential, constructed from the data given in Table 2.3 and 2.4.

(Equation 2.7). In this section, we have estimated the values of A and N₀ from the experimental current maximum of the transients by solving a system of equations that are derived from Equation 2.7¹⁸

$$\ln\left(1 - \frac{i_M t_M^{1/2}}{a}\right) + x - \alpha(1 - e^{-x/\alpha}) = 0 \quad (2.11)$$

$$\ln[1 + 2x(1 - e^{-x/\alpha})] - x + \alpha(1 - e^{-x/\alpha}) = 0 \quad (2.12)$$

where $a = nFD^{1/2}c/\pi^{1/2}$. The relationship between the two approaches is as follows. There are two limiting cases of the general mechanism proposed in the second approach, small α and large α , corresponding to the two extreme cases described in the first approach. For $\alpha \rightarrow 0$ (instantaneous nucleation), $i_{Mt_M^{1/2}}/a \approx 0.7153$, $x \approx 1.2564$; for $\alpha \rightarrow \infty$ (progressive nucleation), $i_{Mt_M^{1/2}}/a \approx 0.9034$, $x \approx 2.1618\alpha^{1/2}$.

The diffusion coefficient of Cu²⁺, D, is needed to interpret the data. The diffusion coefficient can be determined from the decay portion of the current-time transient using the Cottrell equation,

$$i = nFc\left(\frac{D}{\pi t}\right)^{1/2} \quad (2.13)$$

The estimated value of D in 1 mM CuSO₄ + 50 mM H₂SO₄ is $(2.5 \pm 0.5) \times 10^{-5} \text{ cm}^2\text{s}^{-1}$, higher than that expected for typical diffusion coefficient of Cu²⁺ in aqueous solution,²² i.e., $7.8 \times 10^{-6} \text{ cm}^2\text{s}^{-1}$. It is important to note that it is impossible to solve the Equation 2.11 and 2.12 using the literature reported value. Moreover, the value of D estimated from the current transient is in good agreement with that calculated from the cyclic

voltammetric study. Therefore, the value of $2.5 \times 10^{-5} \text{ cm}^2\text{s}^{-1}$ is used in this work to calculate the kinetic parameters for copper electrodeposition.

The current-time transient data and calculated results for copper electrodeposition on LBD, HBD, HOPG and GC are listed in Table 2.3 - 2.6, respectively. The accuracy of the calculation was studied. Figure 2.9 shows the comparison of the experimental data with the theoretical current transients for copper deposition on LBD at both low and high overpotential. The theoretical curves were constructed according to Equation 2.8 using the calculated values of A and N_0 listed in Table 2.3. It is clear that the Scharifker and Mostany's approach adequately describes the copper deposition process on these substrates.

In all cases, the reaction rate, reflected by the current maximum, i_M , increases with applied overpotential, whereas t_M decreases. In other words, the time period required for the coalesce of the hemispherical diffusion zone of each mature nuclei, which serves as the growth center, decreases with overpotential, implying an increase in the number density of growth centers. The observation is consistent with the fact that the number density of sites, N_0 , that are active toward copper nucleation, increases with overpotential. Figure 2.9 shows the dependence of N_0 for copper deposition on diamond electrodes with overpotential. A rather linear relationship ($r^2 = 0.997$) between the $\ln(N_0)$ and η is observed for copper nucleation on HBD within the overpotential range from -360 to -660 mV. However, the plot seems to exhibit two distinct slopes on LBD. At high overpotentials, the increase of N_0 with overpotential is comparable to that on HBD, whereas at low overpotentials the active sites toward copper nucleation are restricted and

the potential-dependence of N_0 diminishes. The value of $i_{MTM}^{1/2}/a$, varying between 0.7 and 0.9, indicates that the copper nucleation does not follow the extreme “instantaneous” or “progressive” nucleation mechanism, which is typical for heterogeneous nucleation on a finite number of active sites on surface. However, the value increase with overpotential and the nucleation approaches the progressive limit on each substrate at high overpotentials.

The kinetics of copper deposition also strongly depend on the nature of the substrate. The lowest number density of active sites is observed on HOPG because of the low density of electrochemically active surface defects. Both N_0 and A increase in the order of HOPG < LBD < HBD < GC. The current maximum is increased by a factor of two while the boron doping level of the diamond film increases from 10^{19} to 10^{21} cm^{-3} . Furthermore, the number density of active sites for copper deposition on HBD is nearly one-order of magnitude higher than that on LBD at the same overpotential. However, the values of N_0 in all cases are much smaller than the atomic density of the substrate (ca. 10^{15} cm^{-2}), which indicates that the restricted density of active sites on the surface may constitute a severe limitation for the formation of copper nuclei.

For the case of progressive nucleation, the steady-state nucleation rate over the entire surface can be expressed as the product of the nucleation rate per active site, A , and the number density of active sites, N_0 . As the nucleation rate decreases continuously due to the decline of the N_0 available for nucleation, the saturation number density of nuclei, attained at long times, is given by¹⁷

$$N_s = \left(\frac{AN_0}{2kD} \right)^{1/2} \quad (2.14)$$

The meanings of k' and D are the same as in Section 6.3.

In the case of 3D nucleation/growth, the growth centers develop into isolated 3D crystallites. Therefore, the saturate number density of nuclei actually reflects the number density of the isolated metal crystallites distributed on the surface. The estimated values of N_s for copper deposition on different substrates are also listed in Table 2.3-2.6. The N_s , ranging from 10^7 to 10^8 cm^{-2} , increases with overpotential.

2.4.2 ECAFM Study of Copper Deposition

Electrochemical studies of the mechanism and kinetics of metal deposition are macroscopic in nature. They provide integral measurements over the whole surface. However, local information concerning the structure of the substrate and the deposit is needed if one wishes to build up a more rigorous model of the process occurring at the microscopic level. Scanning probe microscopy (SPM) has proven to be a useful aid in understanding the fundamentals of electrodeposition at the atomic level.²³⁻²⁷ The ECAFM study of copper deposition on diamond thin-film electrodes is presented in this section. The study has a focus on the measurements of potential-dependent number density of metal particles, their spatial distribution, and the nucleation mechanism.

Surface morphology of the carbon electrodes. The carbon electrodes employed in this work differ from one another in terms of the surface microstructure, chemical composition and electronic properties. The surface morphology of the electrodes is illustrated in Figure 2.11 (A-D). The diamond surface is polycrystalline consisting of well faceted microcrystallites and numerous grain boundaries. The diamond crystals range in diameter from 0.5 to 3 μm . The diamond films exhibit significant surface

roughness, ca. $1.4 \pm 0.5 \mu\text{m}$. Grain boundaries, formed from the coalescence of adjacent grains, are the major defects in polycrystalline films.²⁸ There are also extended defects observed on the grains. Both the grain boundaries and surface defects may serve as active sites for metal deposition. As expected, the structure and morphology is not appreciably altered by boron doping.²⁹

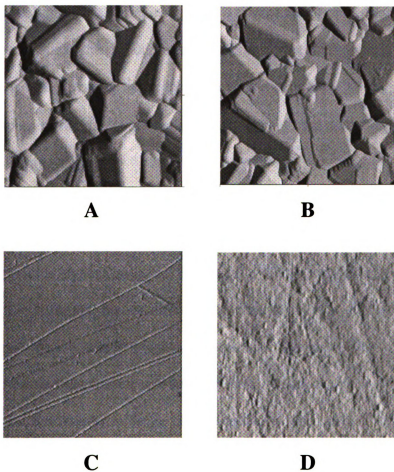


Figure 2.11. AFM images (force mode, in air, $5 \times 5 \mu\text{m}$) of (A) LBD, (B) HBD, (C) HOPG, and (D) GC.

HOPG is an ordered sp^2 -bonded carbon material, in which the graphite sheets are oriented on a macroscopic (i.e. centimeter) scale.³⁰ As seen in Figure 2.11C, freshly cleaved HOPG surface is characterized by atomically flat domains (basal planes) and differently structured defects (edge planes). Cleavage edges (lines shown in Figure 2.11C) are the most often encountered defects on HOPG, whereas some pits and crevices are also observed. GC has graphitic domains limited to 5 – 10 nm, and is isotropic at larger distance scales.³⁰ As seen in Figure 2.11D, the freshly polished GC surface has a “grainy” texture due to the carbon microparticle layer that forms during the abrasive action of the mechanical polishing.³¹ The mean roughness over the $0.5 \times 0.5 \mu\text{m}^2$ area, is 45 ± 6 nm. This apparent roughness is very near that of the 50 nm diameter alumina grit used in the final polishing step.

It has been well established that the electronic properties of the “edge” planes, or defects on HOPG surface, differ drastically from the basal planes. The edge planes provide sites with higher density of “localized” electronic states, favoring facile electron transfer.³⁰ For example, the electron-transfer rate for $\text{Fe}(\text{CN})_6^{-3/4}$ and $\text{Ru}(\text{NH}_3)_6^{+3/+2}$ is approximately four orders of magnitude faster on edge plane than on the basal plane.³⁰ Therefore, the electrochemical properties of the sp^2 -bonded carbon materials are strongly dependent on the fraction of edge plane exposed at the surface. GC, generally with a fractional coverage of edge plane near 100%, exhibits metallic properties for a variety of systems. In contrast, HOPG, with a typical coverage less than 1%, behaves more like a semimetal.³⁰

Copper electrodeposition on LBD. The copper deposition on LBD from 1mM $\text{CuSO}_4 + 50 \text{ mM H}_2\text{SO}_4$ was investigated by ECAFM. The copper deposition, as a

function of the applied overpotential, was first examined. As illustrated in Figure 2.12A, the electrode potential was sequentially stepped to different overpotentials (i.e., 390, -460, -560, -710, and 390 mV). A series of images (Figure 2.12B-F) were collected *in situ* at 30 s after the application of each potential step. It should be noted that each AFM image was collected by scanning the tip from the bottom to the top, and it generally took 20 s to complete each imaging. Therefore, each image corresponds to a 20-s segment of the deposition time. In other words, the copper deposits shown in the upper part of the image are deposited for longer period of time than the ones at the bottom. The triangular markers in Figure 2.12A indicate the starting time of each imaging.

Figure 2.12B shows the AFM image of LBD surface after the electrode potential was stepped to an overpotential of 390 mV. As expected, no copper deposition takes place. The image represents part of a bare diamond surface, which is identical with that obtained at open circuit potential. After the potential was stepped from an overpotential of 390 mV to -460 mV, a number of copper crystallites were generated, as can be seen in Figure 2.12C. The copper crystallites have sizes ranging from 20 nm to 500 nm. It is clear that copper deposits are not uniformly distributed over the surface. The copper nucleation most likely initiates from a limited number of active sites which are predominantly located at the grain boundaries or defects in the diamond surface. As the potential was stepped to higher overpotentials (-560 and -710 mV), the increase in surface coverage of copper deposits is evident (Figure 2.12D and E). On one hand, the initially deposited copper crystallites seem to serve as the growth centers (e.g., Crystallite a) and they increase in size with time at a given overpotential. On the other hand, new copper crystallites were formed (e.g., Crystallite d and e in Figure 2.12D, and Crystallite

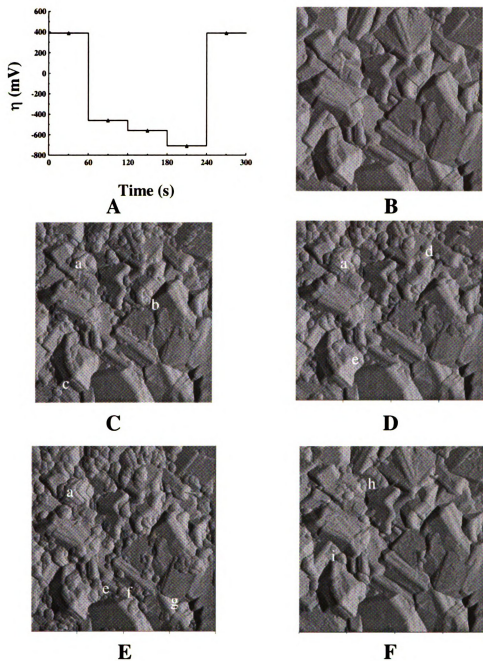
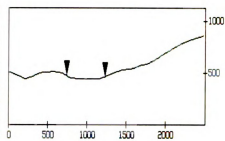
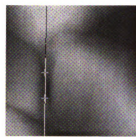
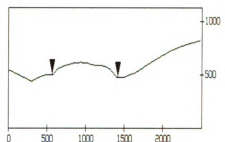
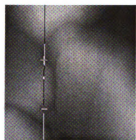


Figure 2.12. ECAFM images (force mode, $10 \times 10 \mu\text{m}$) collected for copper deposition on LBD at overpotentials of (B) 390 mV, (C) -460, (D) -560, (E) -710, and (F) 390 mV for 30 s each. The solution is 1mM $\text{CuSO}_4 + 50 \text{ mM H}_2\text{SO}_4$. (a)-(i) represent individual copper crystallite. The diagram of the sequential potential steps is shown in (A). The triangular markers indicate the starting time of each imaging.

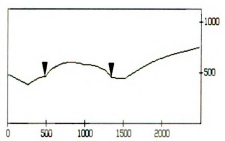
Figure 2.13. ECAFM images (height mode, $2.5 \times 2.5 \mu\text{m}$) collected for copper deposition on LBD in $1\text{mM CuSO}_4 + 50 \text{ mM H}_2\text{SO}_4$ (A) before and (B-E) after the potential step to -460 mV . The deposition times are (B) 30, (C) 60, (D) 120, and (E) 180 s, respectively. Corresponding cross sections, through the top view images shown in the middle column, are indicated by the straight lines. The horizontal distance between the two black cursors represents the lateral dimension of the crystallite.



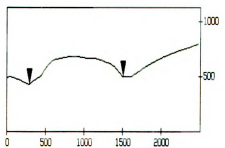
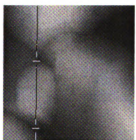
A



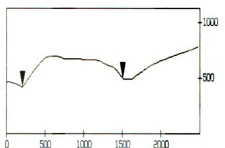
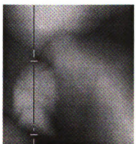
B



C



D



E

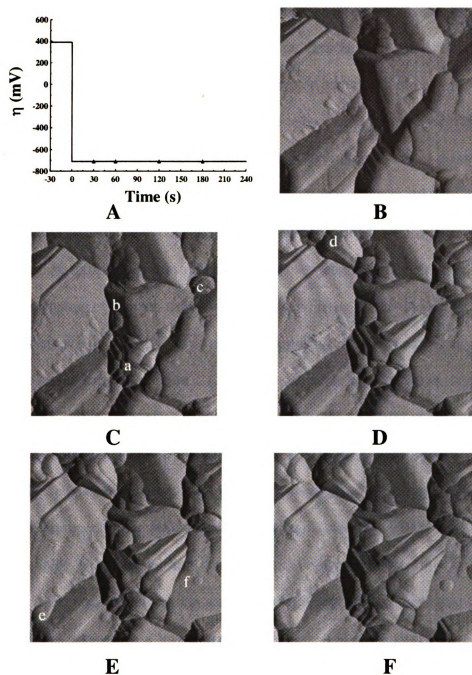


Figure 2.14. ECAFM images (force mode, $4 \times 4 \mu\text{m}$) collected for copper deposition on LBD in $1\text{mM CuSO}_4 + 50\text{mM H}_2\text{SO}_4$ (B) before and (C-F) after the potential step to -710 mV . The deposition times are (C) 30, (D) 60, (E) 120, and (F) 180 s, respectively. (a)-(f) represent individual copper crystallite. The diagram of the potential step is shown in (A). The triangular markers indicate the starting time of each imaging.

f and g in Figure 2.12E). The increase of number density of deposits with overpotential was evident in the chronoamperometric studies. Furthermore, the number density of copper deposits, estimated by manually counting the particles in the AFM image, is about 10^7 - 10^8 cm^{-2} , in good agreement with the theoretical calculations (see Table 2.3). It is also noticeable that some copper crystallites (e.g. Crystallite b and c) disappeared as the potential was stepped to the overpotential of -560 mV. This is presumably due to the occasional displacement of the microparticles by the AFM tip since the copper deposits poorly adhere to the diamond surface. After an overpotential of 390 mV was applied, the anodic stripping of copper deposits took place. Figure 2.12F shows an AFM image recorded after 30 s. Clearly, most of metal deposits are gone and the image is almost identical to that shown in Figure 2.12B, except for some residue copper crystallites (e.g., Crystallite h and i). The result confirms the incomplete stripping of the copper deposits from LBD surface, a phenomenon that was observed in the electrochemical studies.

The copper deposition, at a given overpotential as a function of deposition time, was next examined. In the following experiments, the electrode potential was stepped to a fixed cathodic overpotential and the gradual development of the copper deposits was monitored. Figure 2.13 presents a series of images taken before and after the electrode potential was stepped to a low overpotential (i.e., -460 mV). Figure 2.13A shows the diamond surface prior to the copper deposition. The region consists of three well-faceted diamond microcrystallites and a “deep valley” (grain boundary) between two adjacent grains. As expected, the defective grain boundary provides active sites toward copper deposition, and a copper crystallite (indicated by the arrow in Figure 2.13B), was formed after application of the potential step. The diameter of the crystallite increases with time.

The growth is apparently three-dimensional. The cross section analysis provides a more quantitative assessment of the 3D growth process, which is also shown in Figure 2.13. The copper crystallite has a lateral dimension of ca. 1.3 μm and a height of ca. 0.2 μm after 3 min growth. It's evident that no other copper crystallites were formed in the course of the deposition while the existing one increased in size, which suggests an instantaneous nucleation mechanism. This is in good agreement with the electrochemical measurements.

A series of AFM images (Figure 2.14) were also collected after the electrode potential was stepped to a relatively high overpotential (i.e., -710 mV). As seen in Figure 2.14C, a number of copper crystallites (e.g., Crystallite a, b and c) were formed at the grain boundaries upon application of the potential step. The further development of the crystallites is shown in Figure 2.14D-F. In contrast to that observed at low overpotential, while the existing ones increased gradually in size, some new copper crystallites were formed (e.g., Crystallite d in Figure 2.14D, and Crystallite e and f in Figure 2.14E). It is likely that continuous activation of surface sites toward copper nucleation/growth occurs at high cathodic overpotential on LBD, thus progressive nucleation is favored. This is also consistent with the electrochemical results derived from the current-time transient measurements.

Copper deposition on HBD. The copper deposition on HBD was also investigated by ECAFM. Figure 2.15 presents a series of images taken for copper deposition at different cathodic overpotentials. As revealed in Figure 2.15A, the chosen diamond surface region is free of any copper deposits at an overpotential of 390 mV. Copper nucleation/growth takes place upon stepping potential to an overpotential of -460

mV. The estimated number density of copper crystallites, ca. 10^8 cm^{-2} , falls into the range predicted by the theoretical calculation (see Table 2.4). The number density of copper deposits increases with overpotential as new copper crystallites are continuously formed (Figure 2.15D). At -710 mV , the significant overlap of adjacent copper crystallites and the nucleation/growth over the existing copper deposits take place.

Some interesting features for copper deposition on HBD are noticeable. Copper deposits not only initiate at the grain boundaries, but also decorate the grain surfaces (indicated by the arrows in Figure 2.15D). At the same overpotential, the number density of copper deposits on HBD is much higher than that on LBD. This suggests that the number density of surface active sites toward copper nucleation increases with boron doping level. Complete stripping of copper is observed upon stepping potential back to the overpotential of 390 mV . As can be seen in Figure 2.15F, the surface was returned to a state identical to that before the copper deposition (Figure 2.15B).

Boron doping level can also affect the copper nucleation mechanism. The copper deposition, at a given overpotential as a function of time, was examined. Shown in Figure 2.16 are AFM images taken at the same time sequence as that in Figure 2.13, at an overpotential of -460 mV . Copper deposition on HBD follows a progressive nucleation mechanism, which is in contrast to the observation on LBD. As evidenced by Figure 2.16E, some new copper crystallites (e.g., Crystallite c, d and e) were formed at the grain boundaries as the electrodeposition proceeded.

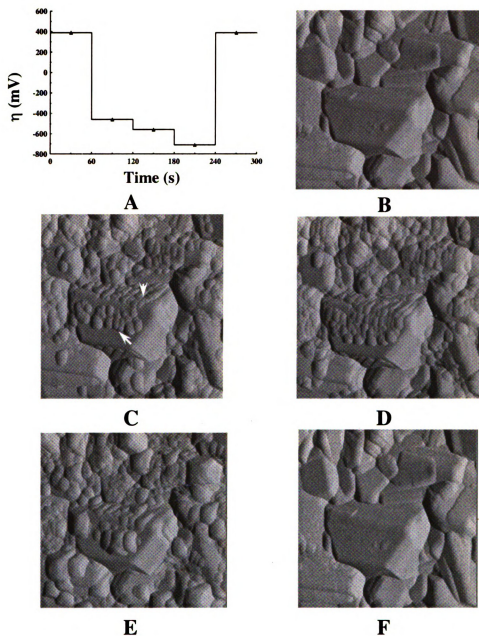


Figure 2.15. ECAFM images (force mode, $5 \times 5 \mu\text{m}$) collected for copper deposition on HBD at overpotentials of (B) 390 mV, (C) -460, (D) -560, (E) -710, and (F) 390 mV for 30 s each. The solution is 1 mM $\text{CuSO}_4 + 50 \text{ mM H}_2\text{SO}_4$. The diagram of the sequential potential steps is shown in (A). The triangular markers indicate the starting time of each imaging.

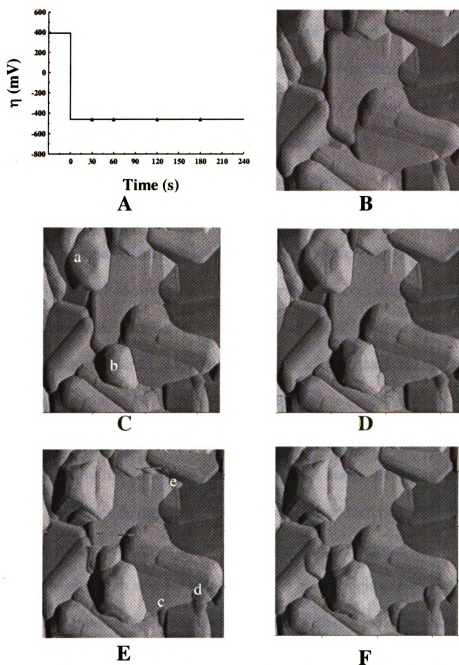


Figure 2.16. ECAFM images (force mode, $3.4 \times 3.4 \mu\text{m}$) collected for copper deposition on HBD in $1\text{mM CuSO}_4 + 50\text{mM H}_2\text{SO}_4$ (B) before and (C-F) after the potential step to -460 mV . The deposition times are (C) 30, (D) 60, (E) 120, and (D) 180 s. (a)-(e) represent individual copper crystallite, respectively. The diagram of the potential step is shown in (A). The triangular markers indicate the starting time of each imaging.

2.5 Discussion

Metal electrodeposition taking place at an electrode-solution interface involves two basic processes: the discharge of solution ions and the formation of new phase on the surface. Therefore, both the electronic properties of the substrate and the chemical natures of the surface can affect the electrodeposition process. Diamond is widegap semiconductor. There are two important mechanisms for electron transfer between a semiconductor and a redox couple in solution: direct electron exchange with conduction band or valance band, and exchange mediated by midgap electronic states.

Figure 2.17 shows the schematic interfacial energy diagram for a polycrystalline diamond electrode, with boron doped at a level of 10^{19} cm^{-3} or greater.⁷ In the case of copper deposition, direct electron exchange is unlikely to occur because the standard reduction potential of $\text{Cu}^{+2/0}$ falls into the band gap region. Therefore, the midgap-state-mediated electron transfer dominates. As a consequence, the copper deposition kinetics are governed by the density of midgap electronic states. Boron-doped, polycrystalline diamond electrodes deviate from ideal *p*-type semiconductor behavior because of a high density of midgap electronic states. Granger et al. has proposed that the midgap density of states results from at least four factors: (i) boron-doping level, (ii) lattice hydrogen content, (iii) inherent grain boundaries and other defects in the polycrystalline film, and (iv) nondiamond carbon impurity phases at the surface.⁷

The boron doping level and uniformity are major factors governing the electrical conductivity of diamond films, hence the electron transfer kinetics at the diamond/electrolyte interface. Boron doped diamond can possess semiconductor to semimetal properties, depending on boron doping level. At boron doping on the order of

10^{19} cm^{-3} or greater, impurity band conduction dominates. At sufficiently high boron concentration, the impurity band tends to emerge with the valence band leading to metallic conduction. Diamond is also host for a variety of extended defects such as stacking faults, microtwins, dislocations, nondiamond carbon impurities, and grain boundaries. The defects could serve as discrete sites for electron transfer or could simply affect the electronic properties of the material by increasing the density of states.⁷

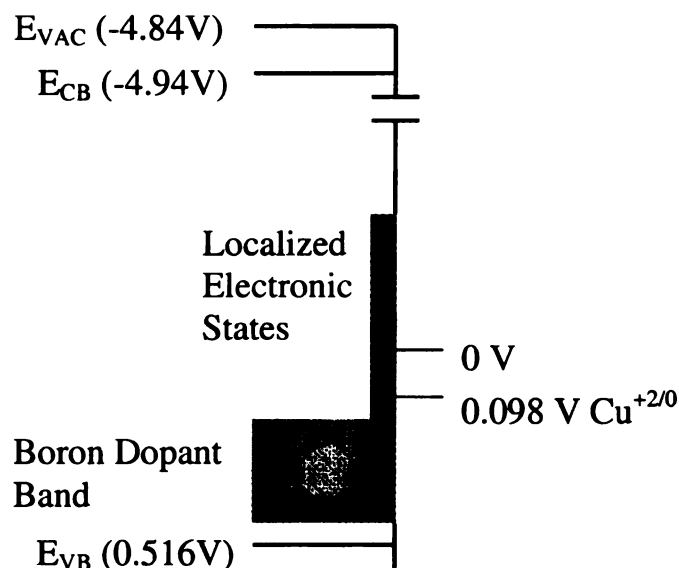


Figure 2.17. Proposed band structure for the diamond/electrolyte interface. E_{VB} , E_{CB} and E_{VAC} are the energies at the bottom of the conduction band, at the top of the valence band and in the vacuum. The potentials are quoted versus SCE. The band positions are determined using a flat-band potential of 0.45 V vs. SCE and a band gap of 5.45 eV.

The observations for copper deposition at diamond electrode can be correlated to its semimetal-semiconductor nature. Distinct copper nucleation overpotentials are

observed. The overpotential for HBD is greater than for GC by some 40 mV, whereas, the overpotential for LBD is greater by some 80 mV. The overpotential is influenced by two processes: the overpotential related to electron transfer (η_t), and the overpotential related to crystallization (η_c). It is likely that η_t dominates in the case of copper nucleation on LBD. Diamond electrodes with a low boron concentration have a relatively low density of states within the midgap. Therefore, high activation energy is required for electron hopping between these electronic states. Furthermore, electrons supplied by the electrode to the solution metal ions need to tunnel through a space charge layer. A potential drop within the electrode bulk might take place. Since the width of the space-charge layer decreases and density of states increases with boron doping, η_t is expected to decrease as the boron-doping level increases.

The overpotential related to crystallization, η_c , is influenced by the substrate since crystallization involves the incorporation of metal adatoms into the surface microstructure. According to the equation³²

$$\Delta G(N) = -Nze|\eta| + \Phi(N) \quad (2.15)$$

the Gibbs free energy of crystal formation is reduced as the overpotential increases (i.e., the $-Nze|\eta|$ term). On the other hand, part of the energy is consumed by the new phase formation (i.e., the $\Phi(N)$ term). $\Phi(N)$ denotes the total energy mainly associated with the formation of new interfaces: crystal/solution and crystal/substrate. It can be written as³²

$$\Phi(N) = \sum \sigma_i A_i + A_{j^*} (\sigma_j - \beta) \quad (2.16)$$

where σ_i and A_i are the specific surface energy and surface area of respective crystallographic face i confining the crystal form. σ_j and A_{j^*} are the specific surface

energy and surface area of crystal face contacting with the substrate. β is the specific adhesion energy between the crystal and the substrate.

Thereby, the smaller $\Phi(N)$, the smaller overpotential required to initiate the nucleation. Strong metal-substrate interaction (i.e., large β) leads to a reduced total surface energy associated with the new phase formation. Therefore, small crystallization overpotential is required. Hydrogen-terminated diamond surface is nonpolar and chemically inert, implying a weak interaction between the deposits and the substrate. Therefore, a relatively higher η_c is expected. In contrast, GC surface is covered with a variety of oxygen-containing functionalities. Strong interaction between metal and surface oxides has been reported.³³

Surface sites associated with localized electronic states (surface states), mediating electron transfer at the diamond/electrolyte interface, may serve as the active sites toward copper nucleation. The population of surface states vary drastically upon polarization of the electrodes in different potentials.³ Therefore, increases in number density of active sites with increased cathodic overpotentials are observed on both diamond electrodes. However, the trend for LBD is diminished at low overpotentials. It is presumably due to the high activation energy of the boron sites and the non-uniform distribution of the surface states. At potentials below a threshold (i.e., ca. -610 mV), most of the localized states remain inactivated and may not participate in the charge transfer at the electrode/electrolyte interface. Accordingly, copper nucleation is restricted to very few active sites on the surface which become exhausted at an early stage in the process, nucleation thus approaches the instantaneous limit. Most of the surface sites are activated at high overpotentials. In this case, progressive nucleation takes place.

The low density of states and the non-uniformity in the energy distribution might lead to a heterogeneous electronic structure on the LBD surface. It is our assumption that the surface of LBD has regions of high electrical conductivity isolated from each other by regions of lower conductivity. Allongue³⁴ has studied metal deposition on semiconductors, also suggesting that the density of charge carriers on the semiconductor surface is small and they must be considered as individual reactants. The fact that copper nuclei formed elusively at the intercrystalline grain boundaries on LBD suggests the grain boundaries are the most active regions toward copper deposition. Indeed, electrically, grain boundaries introduce states within the midgap which trap charge carriers and mediate the charge transfer across the diamond/electrolyte interface.³⁵ Chemically, nondiamond carbon impurities tend to concentrate at the grain boundaries,³⁶ making them susceptible to oxygen attack in the aqueous solution.³⁷ As discussed above, the formation of oxides might reduce the copper nucleation overpotential.

Incomplete copper stripping is observed at the anodic polarization on LBD, which could be also related to the heterogeneous electronic structure. Copper nuclei always initiate at the electrically active sites and then the crystals are gradually spread over to less or non-active sites. During the anodic process, copper deposits which are connected to the active sites can dissolve but dissolution of the apparently poorly contacted rest of the copper deposits does not occur until enough anodic potential applied. According to a “undercutting” model postulated by Adzic et al,³⁸ the faster dissolution of the part of deposit closer to the surface might occasionally cuts off the contact of the rest part of the deposit with the electrode, leaving them as residues on the surface.

The density of states within the midgap induced by boron doping increases with the doping level.³ The number density of active sites increases with increased boron-doping level, in consistent with the increased density of surface states. Moreover, the active sites are no longer restricted at the grain boundaries as evidenced by the formation of copper deposits on the diamond grain surfaces. In other words, both the grains and grain boundaries are equally electrochemically active toward the copper deposition on HBD. The observation is consistent with our recent studies of single crystal diamond film. Chen et al³⁹ investigated the electrochemical behavior of diamond (100) electrode. Relatively small ΔE_{ps} are observed for $\text{Ru}(\text{NH}_3)_6^{+2/+3}$ and $\text{MV}^{+2/+0}$ which have formal potentials well into the band gap region. Since the grain boundaries and defects are negligible at this electrode, the results suggest that the density of states on the single crystal surface, induced by boron doping ($> 10^{19} \text{ cm}^{-3}$), are sufficient high to support facile electron transfer at the diamond/electrolyte interface.

2.6 Conclusions

The copper electrodeposition on boron-doped diamond thin-film electrodes was investigated using cyclic voltammetry, chronoamperometry, and *in situ* atomic force microscopy, in comparison with that on sp^2 -bonded carbon materials, i.e., GC and HOPG. It is shown that the copper nucleation/growth depends strongly on the electrical and chemical natures of the substrate.

Distinct nucleation overpotential is observed for copper deposition on diamond electrodes, presumably due to the chemical inertness of the diamond surface and/or sluggish electron transfer at the diamond/electrolyte interface. The overpotential

decreases with increased boron doping level. A potential-dependent nucleation mechanism was observed on low boron-doped diamond electrode. Copper nucleation at relatively low cathodic overpotentials is restricted to few active sites, which are exclusively located at grain boundaries and other surface defects, thus an instantaneous nucleation mechanism follows. The density of states increases with overpotential, and the progressive nucleation occurs at high overpotentials. Incomplete anodic stripping of copper was observed, presumably due to the heterogeneity of the surface electronic structure.

The number density of active sites toward copper nucleation increases by a factor of 10 when the boron doping is increased from 10^{19} to 10^{21}cm^{-3} . In contrast to low boron-doped diamond electrode, the surface active sites are no longer restricted at grain boundaries. The diamond grains are also electrochemically active at high boron doping level, and a progressive nucleation mechanism is obtained over a wide potential range.

in situ microscopic studies shows that the copper electrodeposition on boron-doped diamond film electrode follows a 3D nucleation/growth mechanism. It is apparent that the size of the metal deposits, number density and spatial distribution are potentially to be controlled by adjusting the applied overpotential, deposition time and electrical conductivity (i.e., boron doping level) of the diamond film.

References:

1. J. Xu, M. C. Granger, Q. Chen, J. W. Strojek, T. E. Lister, and G. M. Swain, *Anal. Chem.*, **69**, 591A (1997).
2. G. M. Swain, A. B. Anderson, and J. C. Angus, *MRS Bulletin*, **23**, 56 (1998).
3. R. Tenne and C. Levy-Clement, *Israel Journal of Chemistry*, **38**, 57 (1998).
4. Y. V. Pleskov, *Russian Chemical Reviews*, **68**, 381 (1999).
5. S. Alehashem, F. Chambers, J. W. Strojek, G. M. Swain, and R. Ramesham, *Anal. Chem.*, **67**, 2812 (1995).
6. M. C. Granger and G. M. Swain, *J. Electrochem. Soc.*, **146**, 4551 (1999).
7. M. C. Granger, M. Witek, J. Xu, J. Wang, M. Hupert, A. Hanks, M. D. Koppang, J. E. Butler, G. Lucazeau, M. Mermoux, J. W. Strojek, and G. M. Swain, *Anal. Chem.*, **72**, 3793 (2000).
8. M. C. Granger, J. Xu, J. W. Strojek, and G. M. Swain, *Anal. Chim. Acta*, **397**, 145 (1999).
9. M. Awada, J. W. Strojek, and G. M. Swain, *J. Electrochem. Soc.*, **142**, L42 (1995).
10. N. Vinokur, B. Miller, Y. Avyigal, and R. Kalish, *J. Electrochem. Soc.*, **146**, 125 (1999).
11. A. Manivannan, M. S. Seehra, D. A. Tryk, and A. Fujishima, *Anal. Lett.*, **35**, 355 (2002).
12. O. Enea, B. Riedo, and G. Dietler, *Nano Letters*, **2**, 241 (2002).
13. C. Prado, S. J. Wilkins, F. Marken, and R. G. Compton, *Electroanalysis*, **14**, 262 (2002).
14. S. Nakabayashi, D. A. Tryk, A. Fujishima, and N. Ohta, *Chem. Phys. Lett.*, **300**, 409 (1999).
15. F. Bouamrane, A. Tadjeddine, R. Tenne, J. E. Butler, R. Kalish, and C. Levy-Clement, *J. Phys. Chem. B*, **102**, 134 (1998).
16. J. Zak and M. Kolodziej-Sadlok, *Electrochim. Acta*, **45**, 2803 (2000).
17. B. Scharifker and G. Hills, *Electrochim. Acta*, **28**, 879 (1983).

18. B. Scharifker and J. Mostany, *J. Electroanal. Chem.*, **177**, 13 (1984).
19. A. J. Bard and L. R. Faulkner, *Electrochemical Methods, Fundamentals and Applications*, John Wiley & Sons, Inc, New York, 1980.
20. A. J. Bard and L. R. Faulkner, *Electrochemical Methods, Fundamentals and Applications*, John Wiley & Sons, Inc, New York, 2001.
21. M. Y. Abyaneh and M. Fleischmann, *Electrochim. Acta*, **27**, 1513 (1982).
22. T. I. Quickenden and Q. Xu, *J. Electrochem. Soc.*, **143**, 1248 (1996).
23. N. Batina, T. Will, and D. M. Kolb, *Faraday Discuss.*, **94**, 93 (1992).
24. R. J. Nichols, W. Beckmann, H. Meyer, N. Batina, and D. M. Kolb, *J. Electroanal. Chem.*, **330**, 381 (1992).
25. Z. Chen, J. Li, and E. K. Wang, *J. Electroanal. Chem.*, **373**, 83 (1994).
26. N. Kimizuka and K. Itaya, *Faraday Discuss.*, **94**, 117 (1992).
27. J. Y. Josefowicz, L. Xie, and G. C. Farrington, *J. Phys. Chem.*, **97**, 11995 (1993).
28. L. S. Pan and D. R. Kania, *Diamond: Electronic Properties and Applications*, Kluwer Academic Publishers, Norwell, MA, (1995).
29. R. Locher, J. Wagner, F. Fuchs, and R. Kalish, *Diamond Relat. Mater.*, **4**, 678 (1995).
30. R. L. McCreery, in *Interfacial Electrochemistry: Theory, Experiment, and Applications*, A. Wieckowski, Editor, Marcel Dekker, New York, 631 (1999).
31. B. Kazee, D. E. Weisshaar, and T. Kuwana, *Anal. Chem.*, **57**, 2736 (1985).
32. E. Budevski, G. Staikov, and W. J. Lorenz, *Electrochemical Phase Formation and Growth*, VCH, New York, 1996.
33. K. Kinoshita and P. Stonehart, in *Modern Aspects of Electrochemistry*, J. O. M. Bockris and B. E. Conway, Editors, Plenum Press, New York, 183 (1977).
34. P. Allongue, S. Blonkowski, and E. Souteyrand, *Electrochim. Acta*, **37**, 781 (1992).
35. N. Vinokur, B. Miller, Y. Avyigal, and R. Kalish, *Electrochem. Solid-State Lett.*, **1**, 265 (1998).

36. W. Zhu, in *Diamond: Electronic Properties and Applications*, D. R. Kania, Kluwer Academic Publishers, Norwell, MA, 173 (1995).
37. H. B. Martin, A. Argoitia, J. C. Angus, and U. Landau, *J. Electrochem. Soc.*, **146**, 2959 (1999).
38. G. D. Adzic, A. R. Despic, and D. M. Drazic, *J. Electroanal. Chem.*, **241**, 353 (1988).
39. Q. Chen, J. Wang, G. M. Swain, I. Sakaguchi, M. Nishitani-Gamo, and T. Ando, unpublished results.

Chapter 3

Fabrication and Characterization of Dimensionally Stable Pt/Diamond Composite Electrodes for Electrocatalysis — The Magnetron Sputtering Approach

3.1 Introduction

The use of nanometer-sized noble metal particles, supported on high surface area carbon materials, is common practice in heterogeneous electrocatalysis. Their catalytic activity essentially depends on the physical and chemical nature of both the catalyst and the support material.^{1-4, and references therein} While sp^2 -bonded carbon supports suffer severe oxidation/corrosion in aggressive chemical environments and at elevated temperature, sp^3 -bonded conductive diamond thin films are extremely stable in such environments. The materials possess several important properties: controllable electrical conductivity, chemical inertness, morphological stability, and corrosion resistance,⁵⁻⁷ all of which make the material an ideal candidate for a catalyst support/host.

The importance of the catalyst/electrode preparation method is well recognized. The preparation method affects the crystallite size, composition, and surface crystallographic orientation of the catalyst, factors that strongly influence the catalytic activity.¹ Common methods, for the preparation of high surface-area catalysts supported on porous substrates (e.g., sp^2 -bonded carbons), include impregnation, ion exchange, colloidal adsorption, electrodeposition, and physical vapor deposition techniques. Clearly, most of the methods might not be applicable for preparing supported catalyst

particles on diamond film because of the geometric nature of the material and its inert surface.

In the search for alternate strategies for the preparation of diamond-film-supported electrocatalysts, magnetron sputtering was a method investigated for depositing the catalytic metal particles. This method has been successfully used, as reported in several studies,^{8,9} to deposit nanoparticles of catalyst on a variety of substrates. In addition, magnetron sputtering, coupled with annealing, has been employed for depositing metal adlayers on diamond films for the fabrication of ohmic contacts.^{10,11}

In this chapter, we report on our initial attempts to prepare Pt/diamond composite electrodes by sequential diamond growth/ Pt magnetron sputtering/ diamond growth fabrication procedure. In this multistep process, a continuous boron-doped diamond thin film was first deposited on a conductive substrate (e.g. Pt foil). The film thickness was 2-5 μm . Next, DC magnetron sputtering was used to deposit a discontinuous layer of Pt on the surface. The Pt-coated diamond film was then subjected to a short, secondary diamond growth in order to anchor the metal particles into the surface microstructure.¹² The resulting Pt/diamond composite films were characterized by scanning electron microscopy (SEM), energy dispersive x-ray analysis (EDX), atomic force microscopy (AFM), auger electron spectroscopy (AES), Raman spectroscopy, powder x-ray diffraction (XRD), secondary ion mass spectrometry (SIMS), and cyclic voltammetry. The results demonstrated that 10-500 nm Pt particles are stably anchored into the surface region of a boron-doped diamond thin film, and the particles are in good electronic communication with the current collecting substrate. The catalyst particles were active for the UPD of hydrogen, reduction of oxygen, and oxidation of methanol.

3.2 Experimental

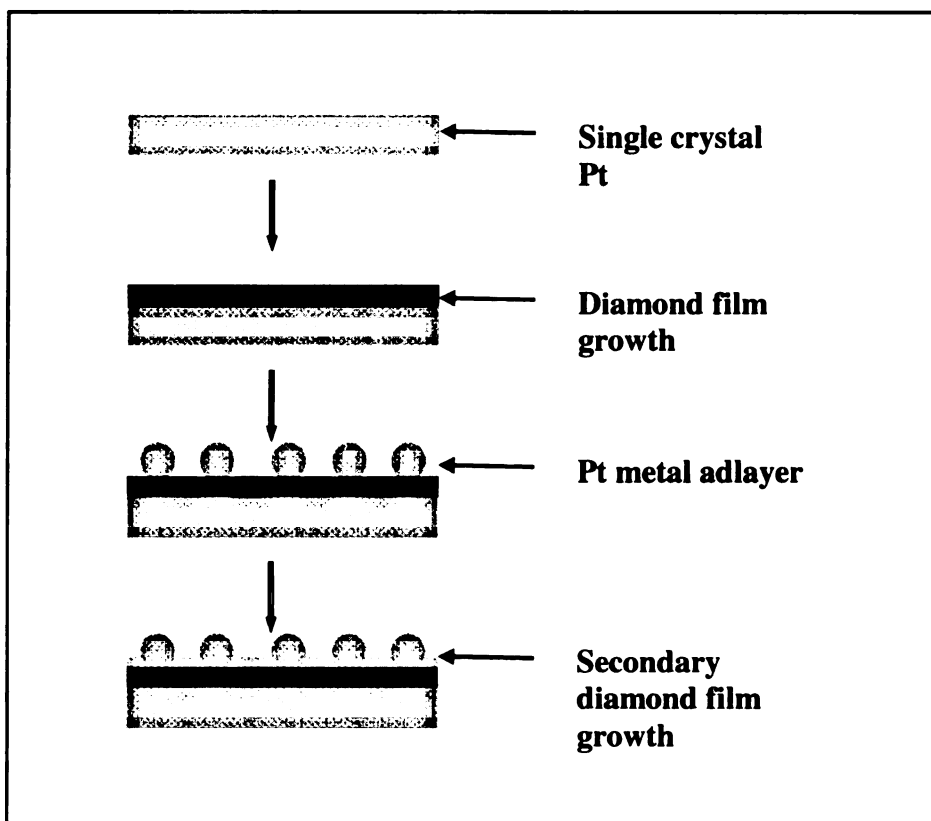


Figure 3.1. Fabrication process for the Pt/diamond composite electrodes.

Preparation of Pt/diamond composite electrodes. The multistep fabrication procedure for the composite electrodes is shown diagrammatically in Figure 3.1. A boron-doped diamond thin film was deposited on Pt (100) substrate using microwave-assisted chemical vapor deposition (CVD). The boron-doped film was deposited for 12 h using a CH_4/H_2 ratio of 0.33 %, a gas pressure of 60 torr, and a substrate temperature of 875 °C. The film thickness at this stage was ca. 3 μm . The boron doping was

accomplished by controlling the B_2H_6 introduced with the source gas mixture (~0.1% B/C). The doping level was in the range of $\sim 10^{19} \text{cm}^{-3}$. The diamond growth was then stopped, the substrate was removed from the chamber, and the diamond film was coated with a discontinuous layer of Pt. The Pt layer was deposited by DC magnetron sputtering. SEM images revealed the Pt metal incompletely covered the diamond surface. The Pt-coated films were then placed back into the CVD reactor and a second diamond deposition was performed, as described above, for 3 h. The extra film thickness was less than $1 \mu\text{m}$. The diamond film deposited on Pt(100) substrate without any sputtered Pt catalyst was prepared using the same 2-step procedure.

Film characterization. SEM was performed with a Hitachi S-800 field-emission microscope. Images were recorded using both secondary and backscattered electrons at an accelerating voltage of 20 kV. Some of the images were also obtained at the Materials Characterization Center (University of Puerto Rico, San Juan, PR) using a JEOL 5800LV microscope with an EDX, x-ray fluorescence CDU leap detector. AFM (both *in situ* and *ex situ*) was performed with a Nanoscope II instrument (Digital Instruments, Santa Barbara, CA). The instrument was equipped with a $12 \mu\text{m}$ scanning head and was operated in the contact mode. A standard fluid cell, constructed with Kel-F and equipped with a gold-coated spring clip and a pyramidal Si_3N_4 45° tip mounted on a cantilever ($100 \mu\text{m}$ legs, 0.38 N/m spring constant), was used to acquire the images *in situ*. The tip was held in an optically transparent holder as part of the fluid cell. The cell was sealed with an acid-resistant ethylene-propylene-diethylene o-ring. The geometric area of the exposed electrode was 0.38 cm^2 . Both the auxiliary and quasi-reference electrodes were Pt wires.

Raman spectroscopy was performed in a 180° backscattered collection geometry using 1.25 m spectrograph (Instruments SA) consisting of an air-cooled 100 mW Ar^+ laser, a 1.25m spectrometer (1800 grooves/mm holographic grating), a 1482E MicraMate confocal microscope assembly, and a Spectrum One 2000 x 800 CCD detector. Spectra were collected with an incident power density of ca. 150 kW/cm^2 (0.010 W and $5 \mu\text{m}$ spot size). The spectrometer was calibrated with either a piece of single crystal Si (lattice phonon mode = 519.0 cm^{-1}) or a Type IIa diamond standard (lattice phonon mode = 1332.5 cm^{-1}).

XRD was performed using a Rigaku RINT1000 diffractometer in a 2-theta/theta geometry. The x-ray source was Cu (1.5407 \AA). The x rays were generated at 200 mA, with a accelerating voltage of 50 kV. The scan rate was 4 degrees/min.

Positive ion SIMS data were acquired with a Camera IMS5F instrument using O_2^+ at 8kV and 100 nA (Surface Analysis Laboratory, University of Utah). The dynamic SIMS profiles were collected over an $85 \mu\text{m}^2$ area with an apparent sputter rate of 0.82 nm/sec. The total sampling depth was estimated to be approximately $1.8 \mu\text{m}$.

The cyclic voltammetry was performed with an CYSY-1090 digital potentiostat (Cypress Systems Inc., Lawrence, KS) using a single compartment glass cell (see Chapter 2) . The exposed geometric area of the working electrode was 0.2 cm^2 . A platinum wire served as the auxiliary electrode and a Ag/AgCl electrode (in sat. KCl) was used as the reference. The H_2SO_4 and HClO_4 acid electrolytes were ultrahigh purity grade (99.999% Aldrich) and the methanol was reagent grade quality (Fisher Scientific). All glassware was cleaned in a KOH/methanol bath prior to use.

3.3 Results and Discussion

3.3.1 Structural Characterization

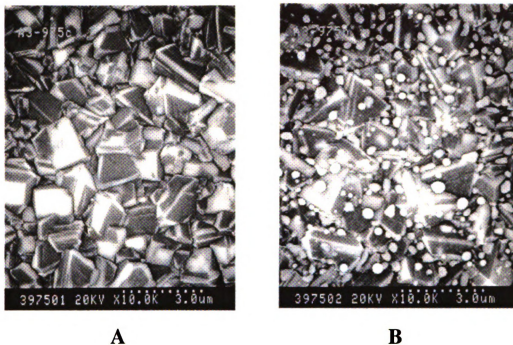


Figure 3.2. SEM images of composite diamond electrodes fabricated (A) with and (B) without Pt.

Figure 3.2A and B show SEM images of boron-doped diamond thin films with and without deposited Pt, respectively. Both images reveal a well-facted, polycrystalline morphology with octahedral, cubic, and cubo-octahedral microcrystallites. The larger crystallites are approximately $2\ \mu\text{m}$ in diameter at the base, and roughly $1\ \mu\text{m}$ in height. There are numerous grain boundaries, extended defects and re-entrant grooves on the crystallites. The film deposited with Pt clearly shows the presence of pseudo-spherical metal particles dispersed over the surface. The larger particles have diameters between 100 and 500 nm. Unfortunately, these deposits are too large for a practical catalytic

electrode. The metal deposits exist at both defect sites on the grains, and in the grain boundaries. As will be shown below, the deposits are strongly anchored to the surface because of the secondary diamond film growth around the base.

Figure 3.3 shows a higher magnification top-view, $5 \times 5 \mu\text{m}^2$ AFM image (force mode, air) of Pt/diamond composite electrode which reveals the dispersed metal deposits. The larger deposits are located almost exclusively at grain boundaries and other extended defects. There are also many smaller deposits dispersed on the facets. These smaller deposits have diameters ranging from 10 to 50 nm.

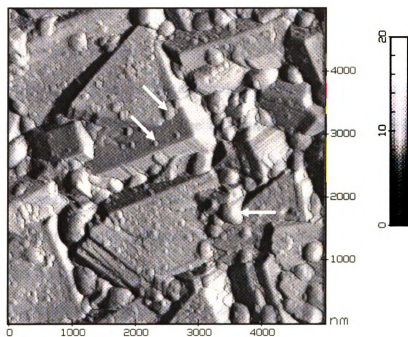


Figure 3.3. AFM force-mode image (contact mode, air) of a Pt/diamond composite electrode. The z-axis is 40 nN full-scale.

Energy dispersive x-ray analysis (EDX) data, combined with SEM, and AES results confirmed that the spherical particles were Pt. In the EDX microanalysis

spectrum, the C K α (0.277 KeV), O K α (0.525 KeV), and Pt M α (2.05 KeV) and L α (9.44 KeV) emissions were observed. The atomic percentages of each element present were ca. 95, 2 and 3, respectively. These values are semi-quantitative because there is typically a 1 to 5% error in the determination of the lighter elements and a ca. 0.5% error in the determination of the heavier elements by this method. The estimated Pt/C and O/C atomic ratios were 0.033 and 0.024, respectively. For comparison, AES analysis of a larger region on the surface indicated a Pt/C ratio of 0.071. The approximately equal amounts of Pt and O is not surprising because this electrode was used extensively in electrochemical measurements prior to making the EDX measurements. Consequently, the surface of the Pt particles and the local diamond support would be expected to possess some chemisorbed oxygen.

Raman spectra for composite electrodes, fabricated with and without the incorporated Pt, are shown in Figure 3.4. The spectrum for the metal-containing electrode shows an intense peak at 1336.8 cm⁻¹, which is attributed to the first-order diamond phonon mode. The peak position is shifted some 5 cm⁻¹ toward higher energy due to the compressive stress within the film because of (i) platinum's higher thermal expansion coefficient and (ii) the incorporation of the Pt particles.^{13,14} The first-order diamond line intensity and position are sensitive to factors such as the crystallite size, optical density, film quality, and net stress.¹⁵ The intrinsic stress (compressive or tensile) in a film can be determined by the shift of the diamond line from the 1332.5 cm⁻¹ position expected for stress-free, phase-pure diamond.^{13,16} The linewidth (FWHM) of the peak is 9.2 cm⁻¹, which is larger than the 2-3 cm⁻¹ linewidth observed for single crystal diamond. The linewidth is a measure of the crystalline perfection, being inversely related to the phonon

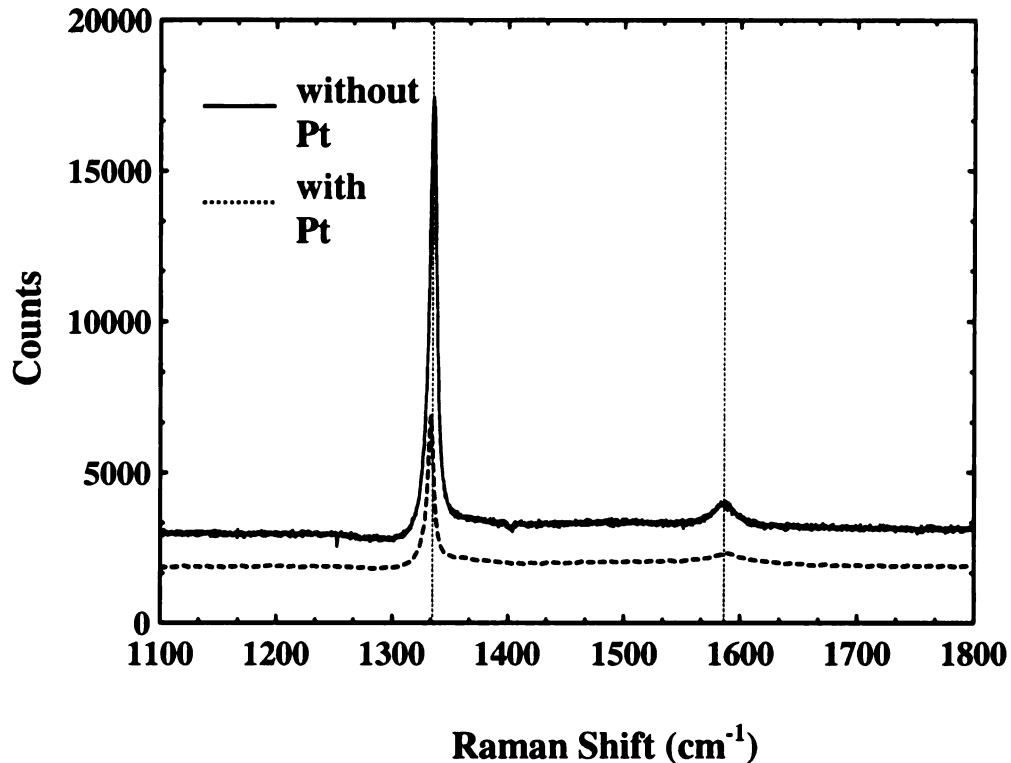


Figure 3.4. Raman spectra for diamond composite electrodes fabricated with and without Pt. Excitation = 514.5 nm. Integration time = 10 s. The laser power density at the sample was estimated to be ca. 150 kW/cm².

lifetime. There is a weak scattering intensity at 1589.9 cm⁻¹, which is attributable to non-diamond *sp*²-bonded carbon impurity domains. The peak position is such that these non-diamond impurities appear graphitic in nature, and probably exist at the interface between the Pt substrate and the diamond. TEM analysis revealed a 100-300 nm region at the diamond/substrate interface that consists of graphitic carbon.¹⁴ The ratio of the 1589 to 1337 cm⁻¹ peak areas is 0.006. It should be noted that the scattering cross section coefficient for graphite (a model for the *sp*²-bonded carbon impurity) is 50 times larger than that for diamond using visible excitation, thus the spectra reveal the film is largely

diamond in character.¹⁷ The spectrum for the composite electrode without Pt shows an intense diamond line at 1335.7 cm^{-1} with a linewidth of 7.3 cm^{-1} . The diamond line is much more intense for this film because the optical density is much lower (i.e., sampling volume of the excitation light is larger) without the Pt particles. A peak at 1587.3 cm^{-1} , associated with scattering from graphitic carbon impurities, is also observed. The ratio of the 1587 to 1336 cm^{-1} peak areas is 0.002. The larger linewidth for the composite electrode with Pt reflects a higher degree of crystalline imperfection due to the incorporated metal deposits.

The diamond films are clearly well faceted with different exposed primary crystallographic orientations. Powder XRD was used to determine the crystallographic orientations of the diamond as well as Pt particles. The major diamond reflections were observed at 43.9 degrees (111-orientation), 75.5 degrees (220-orientation), and 91.7 (311-orientation). Reflections associated with the Pt (either the Pt particles or the Pt substrate) were observed at 39.5 degrees (111-orientation), 46.3 degrees (200-orientation), 67.5 degrees (220-orientation), 81.5 degrees (311-orientation), 86.0 degrees (222-orientation), 108.8 degrees (400-orientation), and 123.0 degrees (420-orientation).¹ There was also some weak diffraction intensity detected at 26.5 degrees associated with the graphitic carbon impurities, probably located either at the diamond/Pt substrate interface. This peak intensity was about 5% as intense as the diamond (111) line at 43.9 degrees. These data confirm the crystalline nature of the diamond, the Pt nanoparticles, and the Pt substrate.

Figure 3.5A and B show dynamic SIMS profiles (positive ion mode) for several of the major ions sputtered from composite electrodes deposited with and without Pt,

respectively. The major ion profiles are shown for C (m/z 12), B (m/z 11), O (m/z 16), N (m/z 14), Si (m/z 29), and Pt (m/z 195). The profile for the composite electrode containing Pt shows significantly increased levels of B, O, Si, and particularly Pt, in the near-surface region. The Pt relative ion intensity is about 5 orders of magnitude larger at the surface than in the diamond film bulk. The Pt does appear to be distributed in the near-surface region of the film because 1000 seconds of sputtering time corresponds to about 820 nm, and the microcrystallite height is approximately 1 μm . It should be mentioned that Pt particles trapped in the diamond matrix, away from the Pt substrate, have been observed by TEM.¹⁴ Most interesting is the significant increase in the boron signal near the surface, concomitant with the increase in Pt. The surface B signal is some 2 to 3 orders of magnitude larger at the surface than in the bulk. This is a very interesting observation and may result from the formation of a "Pt-boride" complex at some of the Pt sites. The SIMS profile for the composite electrodes deposited without Pt reveals the same major ion profiles, but the signal for Pt is near the baseline level at all depths. Very interestingly, the B signal decreases in the near surface region, from that of the bulk, and then increases at the surface. The reason for this fluctuation in the B concentration is unknown at present. The other elements have constant ion intensity profiles from the surface into the bulk. The N concentration at the surface slightly decrease from that observed in the bulk.

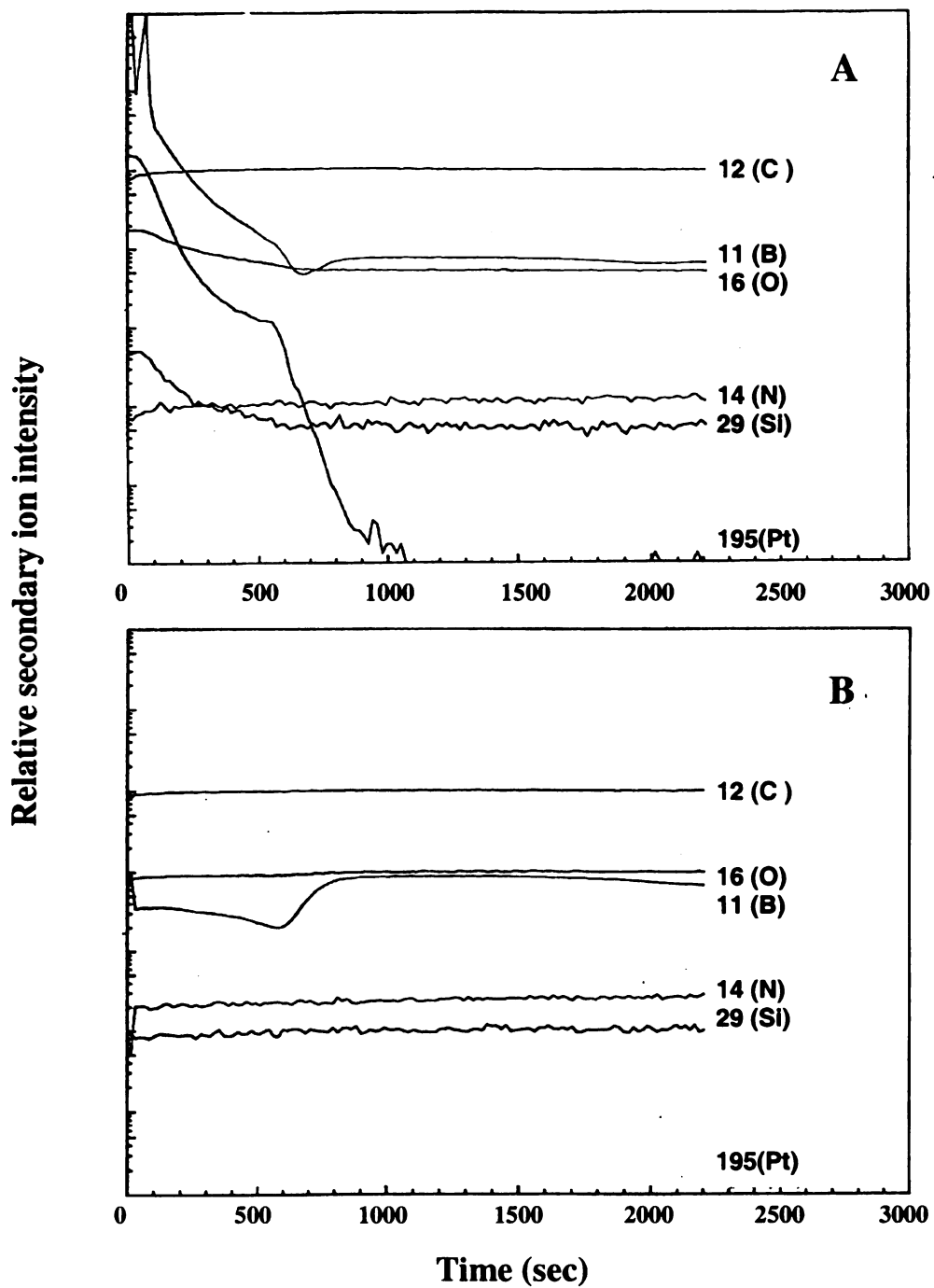


Figure 3.5. Dynamic SIMS profiles (positive ion mode) for diamond composite electrodes prepared (A) with and (B) without Pt.

3.3.2 Electrochemical Characterization

The as-deposited Pt/diamond composite electrode was initially conditioned in 0.1 M HClO₄ by potential cycling between -300 mV and 1500 mV vs. Ag/AgCl. Figure 3.6A shows a background cyclic voltammetric i-E curve in 0.1 M HClO₄ for a Pt/diamond composite electrode obtained after 50 cycles. Figure 3.6B shows a similar curve in 1 M H₂SO₄. The potential sweep rate for both was 50 mV/s and the sweeps were initiated at 0 mV and scanned in the positive direction. The voltammetric features are all characteristic of polycrystalline Pt with the Pt oxide formation and oxygen evolution at potentials positive of 900 mV, the reduction of Pt oxide at *ca.* 400 mV, the adsorption and desorption of hydrogen between 0 and -250 mV, and the double layer region between *ca.* 100 and 250 mV. Integration of the oxidation charge associated with the desorption of hydrogen between 100 and -250 mV yields a value of 120 $\mu\text{C}/\text{cm}^2$. This charge can be used to calculate the *active* Pt metal loading of 242 ng/cm² (diamond electrode geometric area), assuming a 1 x 1 H:Pt surface structure.^{18,19} These features demonstrate the composite electrode contains active Pt particles at the surface that are in good electronic communication with the current collecting substrate, through the boron-doped film.

Figure 3.7A and B show background cyclic voltammetric i-E curves in 0.1 M HClO₄ (first scan) and 1 M H₂SO₄ for a composite electrode deposited without incorporated Pt, respectively. These voltammograms show no evidence for Pt. These results indicate that the diamond film completely covers the Pt substrate, and that the substrate does not directly influence the electrochemical response of the electrodes.

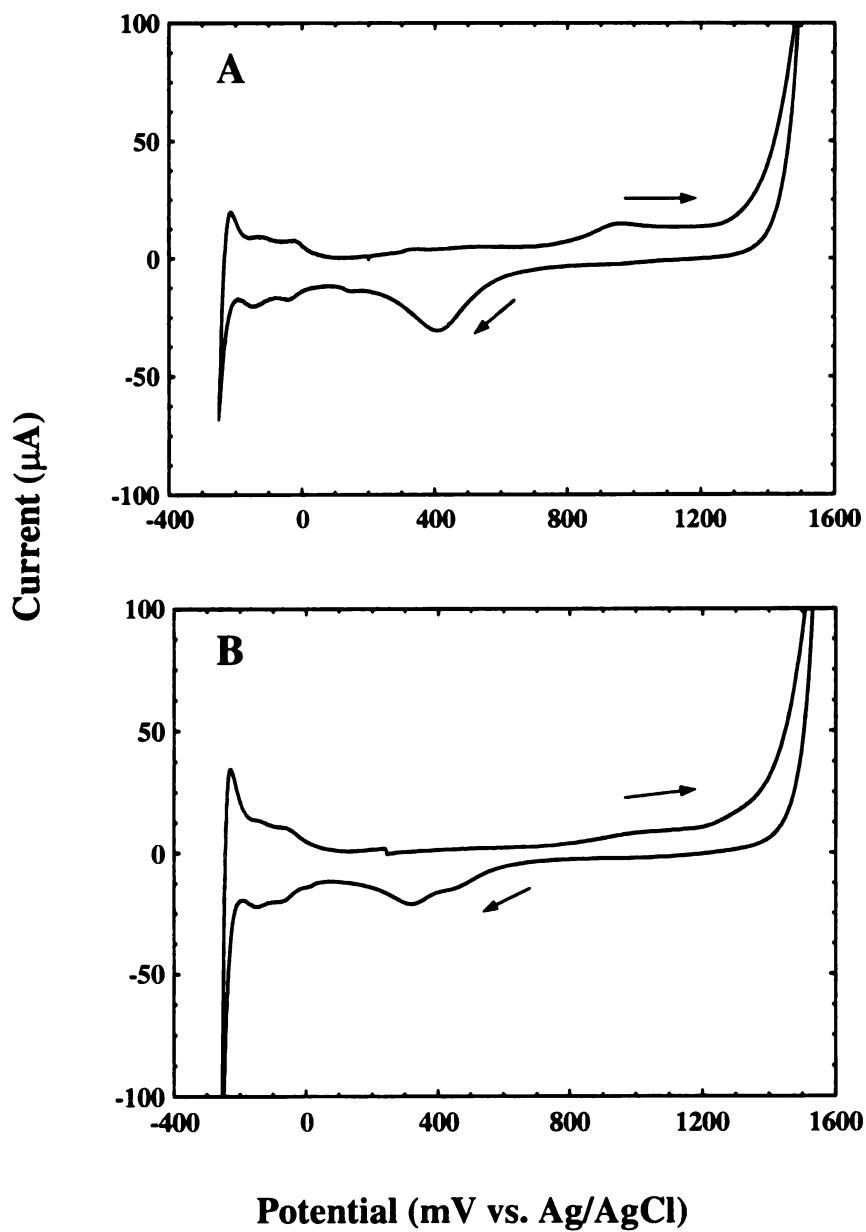


Figure 3.6. Cyclic voltammetric i-E curves for a Pt/diamond composite electrode in (A) 0.1 M HClO_4 and (B) 1 M H_2SO_4 . Scan rate = 50 mV/s.

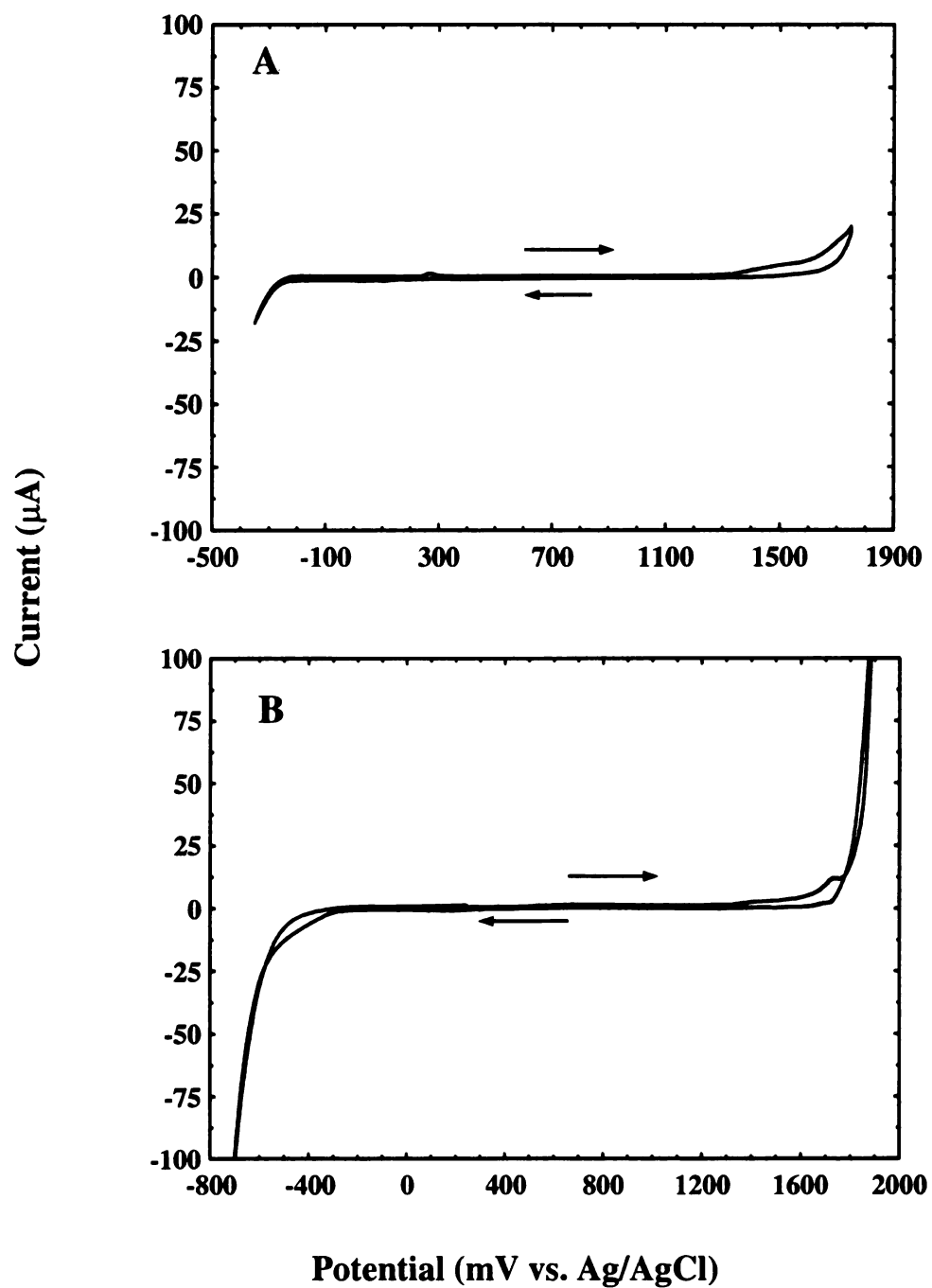


Figure 3.7. Cyclic voltammetric *i*-E curves in (A) 0.1 M HClO₄ and (B) 1 M H₂SO₄ for a composite electrode prepared without Pt. Scan rate = 50 mV/s.

There are no pinholes or voids in the diamond film. In fact, the curves are rather featureless between the solvent electrolysis potentials; that is the oxidation of water to oxygen at 1700 mV and the reduction of water to hydrogen at -700 mV, yielding a working potential window of 2.4 V. This window is smaller than the 3 to 4 V typically observed for high quality, polycrystalline diamond,^{7,20} and probably results from the defects and the graphitic impurities present in the film, formed as a result of the growth on the Pt substrate (see evidence for this in the Raman data).¹⁴ There is some anodic charge passed at ca. 1400 mV, just prior to the onset of oxygen evolution. This is likely due to the oxidation of the surface at exposed non-diamond carbon impurity sites.

It is our supposition that polycrystalline diamond could function well as a catalyst support. The fact that the Pt particles are anchored into the diamond matrix could lead to a high degree of electrode stability and durability.^{21,22} Some of the problems, such as catalyst mobility, aggregation and detachment, that can occur with sp^2 -carbon-supported catalysts, particular when operated at elevated temperature in aggressive chemical environments, may be alleviated by incorporating the catalyst particles into the diamond surface microstructure. The stability of the a Pt/diamond composite electrode was investigated at room temperature in 0.1 M HClO₄ during long-term potential cycling between -400 mV and 1500 mV vs. Ag/AgCl. One thousand cycles were performed at a potential scan rate of 50 mV/s. Figure 3.8 shows cyclic voltammetric i-E curves before and after the cycling. The maximum current density achieved at the anodic and cathodic potential limits was ca. 1 mA/cm². The open circuit potential before cycling was 454 mV vs. Ag/AgCl and increased only slightly to 467 mV after cycling. This minimal change in

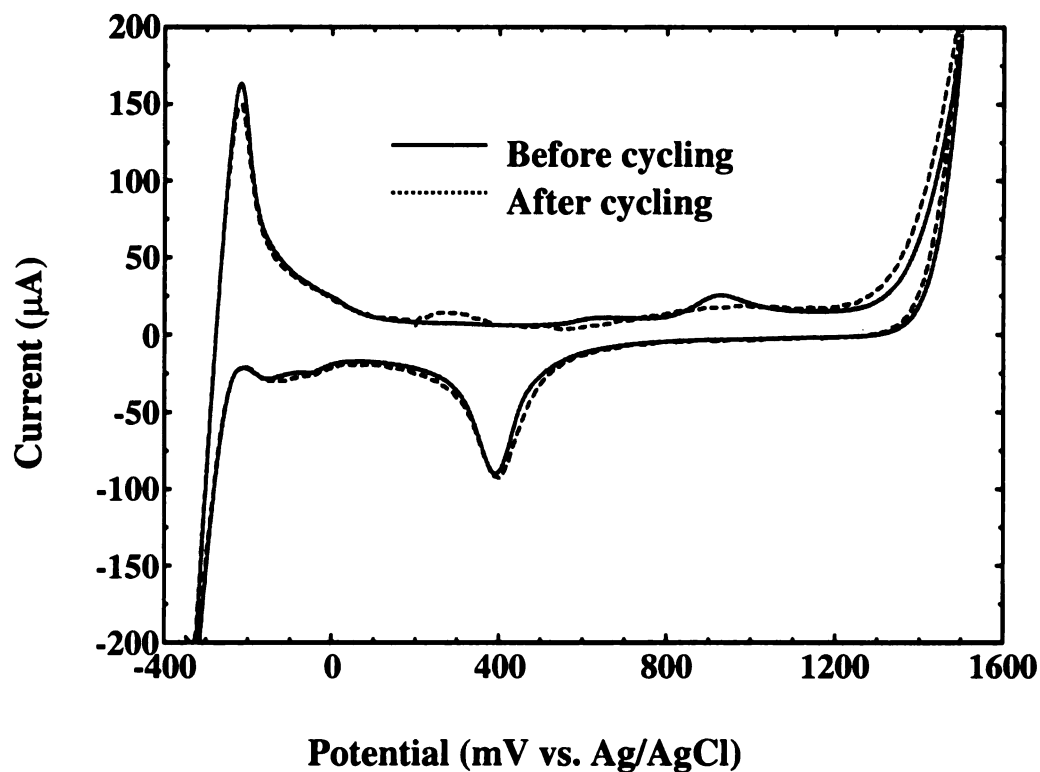


Figure 3.8. Cyclic voltammetric i-E curves in 0.1 M HClO₄ for a Pt/diamond composite electrode before and after 1000 potential cycles between -400 and 1500 mV vs. Ag/AgCl. Scan rate = 50 mV/s. The maximum anodic and or cathodic current density during the cycling was ~1 mA/cm².

potential indicates the absence of significant alterations in the physical and chemical properties of the surface. The charge associated with the oxidative desorption of adsorbed hydrogen was measured before and after cycling. This charge is a good measure of the *active* Pt exposed.^{20,21} The charge before cycling was 175 µC/cm² (353 ng/cm²) and after cycling increased to 210 µC/cm² (424 ng/cm²). The loading values reflect the mass of the electrochemically *active* Pt normalized to the diamond film geometric area. The increase indicates that metal dispersions were not lost during the cycling, but rather the active

catalyst area increased. This increase is attributable to (i) the surface roughening that occurs during the potential cycling through the Pt-oxide/oxygen and hydrogen evolution regimes, and (ii) the cleaning effect brought about by the oxygen and hydrogen gas evolution (i.e., removal of hydrocarbon contaminants or Pt-boride complexes). The hydrogen desorption charge after the extended cycling is much larger than the $120 \mu\text{C}/\text{cm}^2$ reported in Figure 3.6. This is because the electrode was used in numerous electrochemical measurements between the time the data in Figures 3.6 and 3.8 were obtained, such that significant cleaning occurred.

Further evidence for the electrode stability and durability comes from electrochemical AFM investigations of the composite electrode during long-term potential cycling between the same potential limits as measured in the previous figure. Figure 3.9A shows a $5 \times 5 \mu\text{m}^2$ image of the electrode surface in 0.1 M HClO_4 prior to any cycling. The well faceted diamond morphology can be seen along with the Pt metal dispersions. The metal particles are distributed in the grain boundaries and at defects on the grains. The deposits range in diameter from about 100 to 500 nm. Figure 3.9B shows a $5 \times 5 \mu\text{m}^2$ image of the same region of the electrode after one thousand potential cycles. No alterations in the diamond morphology or in the size, distribution and location of the metal deposits are seen. These observations support the notion that the metal deposits are strongly anchored into the diamond surface microstructure by virtue of the secondary diamond growth, and that the electrode structure is very stable.

The electrocatalytic activity of the Pt/diamond composite electrode for the electrooxidation of methanol was examined. Figure 3.10 shows cyclic voltammetric i-E

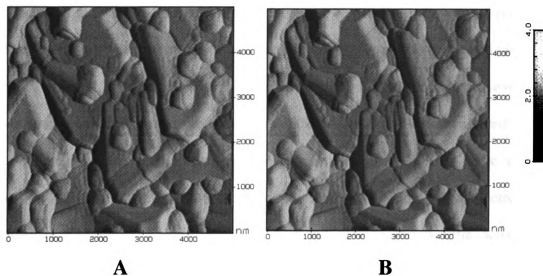


Figure 3.9. Electrochemical AFM images for a Pt/diamond composite electrode in 0.1 M HClO₄ (A) before and (B) after 1000 potential cycles between -400 and 1500 mV vs. Ag/AgCl. Scan rate = 50 mV/s. The z-axis is 4 nN full-scale. The images were acquired at 350 mV vs. Ag/AgCl.

curves for electrodes, with and without incorporated Pt, in 0.6 M CH₃OH + 0.1 M HClO₄. Methanol is considered to be a useful fuel for fuel cells, and Pt is known to catalyze the oxidation of methanol.²³⁻²⁵ The oxidation reaction is complex, the oxidation current depends on the crystallographic orientation of the Pt electrode, and several different products can form (e.g., carbon monoxide, carbon dioxide, formaldehyde, etc.).²³⁻²⁵ No attempt was made to identify the product(s) in the present work. Comparing the two voltammograms, one can see that the Pt-containing electrode is electroactive for methanol oxidation while the bare diamond electrode is not. The methanol oxidation current at the Pt/diamond composite electrode commences at 400 mV on the forward sweep and reaches a maximum current density of ca. 0.9 mA · cm⁻² (geometric area of

diamond film) at 650 mV. The current then decreases on the forward sweep at potentials positive of 650 mV as some of the surface sites, previously available for coordinating the methanol reactant, become blocked by the forming Pt-oxides. Upon scan reversal, a second oxidation maximum is observed at ca. 500 mV as the Pt-oxides are reductively removed making sites available again for coordinating methanol. A more detailed discussion of the methanol electrooxidation at Pt/diamond composite electrodes is provided in Chapter 6. Clearly, the bare diamond surface shows little activity for methanol oxidation.

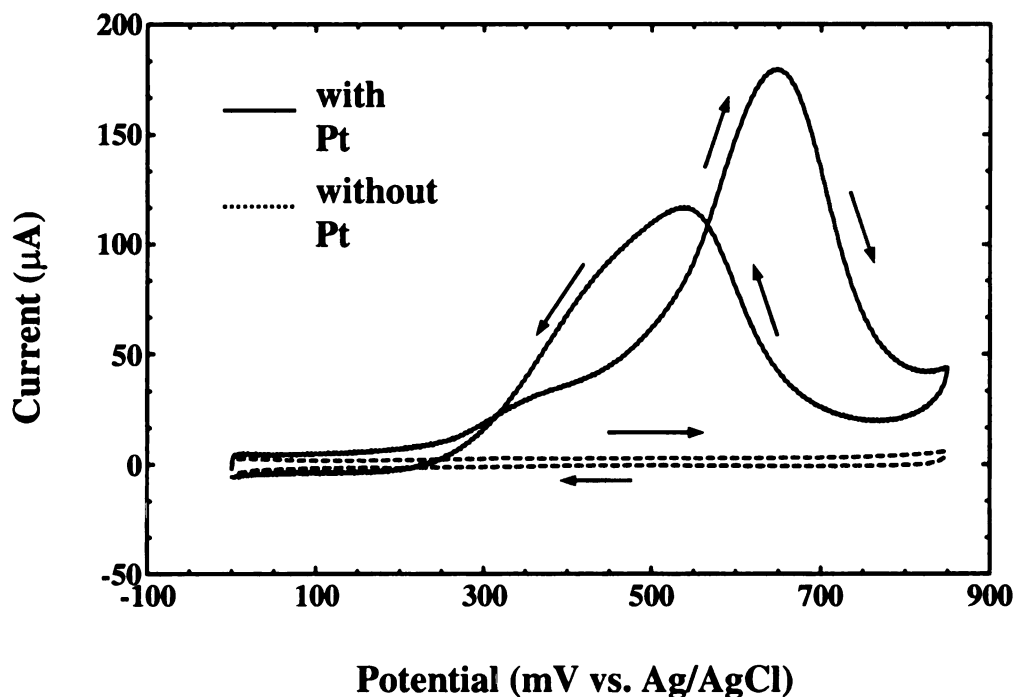


Figure 3.10. Cyclic voltammetric i-E curves for boron-doped diamond composite electrodes with and without deposited with Pt in 0.6 M CH₃OH + 0.1 M HClO₄. Scan rate = 50 mV/s.

The electrocatalytic activity of the Pt/diamond composite electrode for oxygen reduction was also examined. The oxygen reduction reaction is the anodic reaction in fuel

cells and platinum is the best-known electrocatalyst.²⁶⁻²⁸ The potential sweep was initiated at 600 mV and scanned in the positive direction at a scan rate of 50 mV/s. During the cathodic scan, the reduction current commences at ca. 600 mV and reaches a maximum of 215 μA at ca. 280 mV. It should be noted that the cathodic current is a sum of the oxygen reduction current, the current due to Pt oxide reduction, and the double-layer charging current. Clearly, the oxygen reduction current at 250 mV is due solely to the activity of the Pt catalyst. This is evident by comparing the cyclic voltammetric i-E curve for the diamond composite electrode without incorporated Pt. This response of the bare electrode is featureless from -400 mV to 1500 mV with no reduction current at 250 mV. Diamond is known to have a large overpotential for oxygen reduction in both acidic²⁹ and basic media.³⁰ Detailed kinetic data for oxygen reduction at Pt/diamond composite electrodes are reported in Chapter 5.

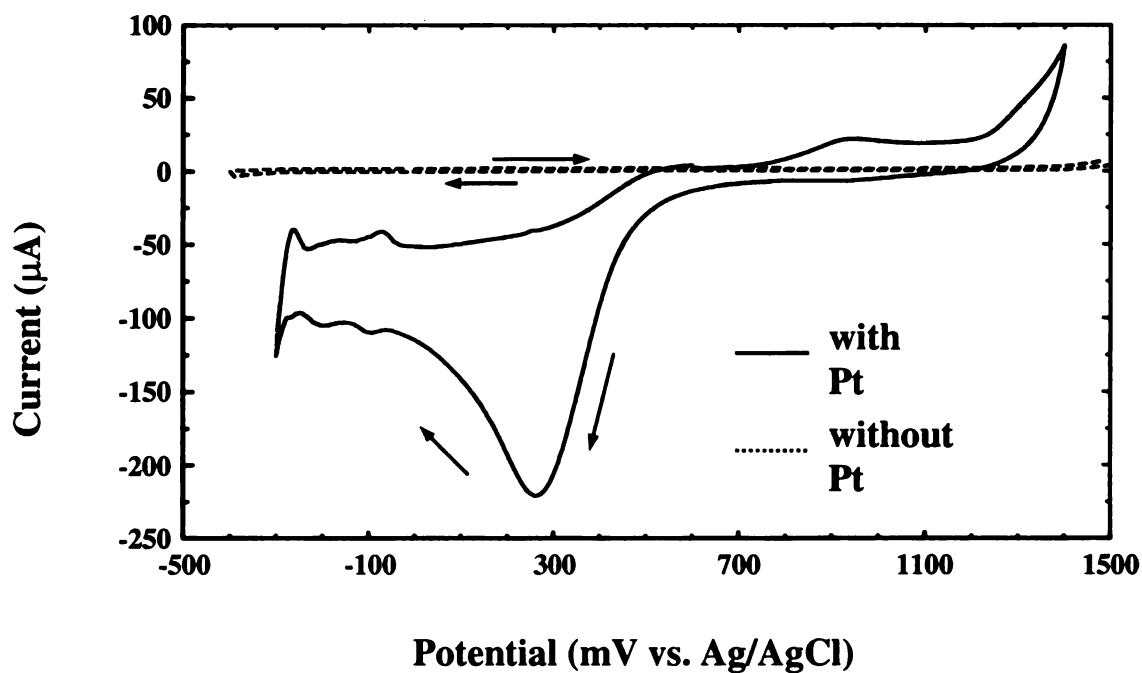


Figure 3.11. Cyclic voltammetric i-E curves for diamond composite electrodes, with and without Pt, in O_2 -saturated 0.1 M HClO_4 . Scan rate = 50 mV/s.

3.4 Conclusions

A new electrocatalytic composite electrode was prepared and characterized – a boron-doped diamond thin film containing incorporated Pt nanoparticles. The composite electrodes were fabricated by a multistep procedure (1. diamond growth, 2. metal deposition, 3. secondary diamond growth), in which the Pt catalyst was deposited by DC magnetron sputtering. The composite electrodes were characterized by scanning electron microscopy, energy dispersive x-ray analysis, atomic force microscopy, auger electron spectroscopy, Raman spectroscopy, powder x-ray diffraction, secondary ion mass spectrometry, and cyclic voltammetry. The dimensionally stable, corrosion-resistant, and electrically conductive composite electrode consists of well-faceted diamond microcrystallites with dispersed Pt particles incorporated into the surface microstructure. These particles range widely in diameter from 10 to 500 nm, and practically speaking, are too large for real world application. Nevertheless, the Pt nanoparticles are strongly anchored into the surface region because of their location at the intercrystalline grain boundaries, and because the diamond film appears to grow around their base. Most interestingly, the Pt nanoparticles at the film surface are in electronic communication with the current collecting Si or Pt substrate through the boron-doped diamond matrix, and they are electroactive for the UPD of hydrogen, the reduction of oxygen, and the oxidation of methanol. The dispersed Pt particles in the diamond microstructure are extremely stable as no decrease in the activity was observed after 1000 potential cycles between the oxygen and hydrogen evolution regimes ($\sim 1-6 \text{ mA}\cdot\text{cm}^{-2}$) in 0.1 M HClO₄.

References:

1. K. Kinoshita and P. Stonehart, in *Modern Aspects of Electrochemistry*, J. O. M. Brokris, B. E. Conway and R. E. White, Editors, Plenum, New York, **12**, 183 (1977).
2. K. Kinoshita, in *Modern Aspects of Electrochemistry*, J. O. M. Brokris, B. E. Conway and R. E. White, Editors, Plenum, New York, **14**, 53 (1982).
3. T. D. Jarvi and E. M. Stuve, in *Electrocatalysis*, J. Lipkowski and P. N. Ross, Editors, Wiley-VCH, New York, 75 (1998).
4. C. Lamy, J. M. Leger, and S. Srinivasan, in *Modern Aspects of Electrochemistry*, J. O. M. Brokris, B. E. Conway and R. E. White, Editors, Plenum, New York, **34**, 53 (2001).
5. J. Xu, M. C. Granger, Q. Chen, J. W. Strojek, T. E. Lister, and G. M. Swain, *Anal. Chem.*, **69**, 591A (1997).
6. R. Tenne and C. Levy-Clement, *Israel Journal of Chemistry*, **38**, 57 (1998).
7. G. M. Swain, A. B. Anderson, and J. C. Angus, *MRS Bulletin*, **23**, 56 (1998).
8. A. B. Anderson, *Electrochim. Acta*, **44**, 1441 (1998).
9. A. Berthet, A. L. Thomann, F. J. Cadete Santos Aires, M. Brun, C. Deranlot, J. C. Bertolini, J. P. Rozenbaum, P. Brault, and P. Andrezza, *J. Catal.*, **190**, 49 (2000).
10. P. E. Viljoen, E. S. Lambers, and P. H. Holloway, *J. Vac. Sci. Technol.*, **B12**, 1997 (1994).
11. L. L. Moazed, J. R. Zeidler, and M. J. Taylor, *J. Appl. Phys.*, **68**, 2246 (1990).
12. C. Wang and T. Ito, *Appl. Phys. Lett.*, **75**, 1920 (1999).
13. L. Bergman and R. J. Nemanich, *J. Appl. Phys.*, **78**, 6709 (1995).
14. T. Tachibana, Y. Yokota, K. Miyata, T. Onishi, K. Kobashi, M. Tartunati, Y. Takai, R. Shimizu, and Y. Shitani, *Phys. Rev. B*, **56**, 15967 (1997).
15. W. Yarbrough and R. J. Messier, *Science*, **247**, 688 (1990).
16. J. R. Dennison, M. Holtz, and G. M. Swain, *Spectroscopy*, **11**, 38 (1996).
17. D. S. Knight and W. B. White, *J. Mater. Res.*, **4**, 385 (1989).

18.

19.

20.

21.

22.

23.

24.

25.

26.

27.

18. J. Clavilier, J. P. Ganon, and M. Petit, *J. Electroanal. Chem.*, **265**, 231 (1985).
19. W. Chrzanowski, H. Kim, and A. Wieckowski, *Catalysis Lett.*, **50**, 69 (1998).
20. J. Xu, Q. Chen, and G. M. Swain, *Anal. Chem.*, **70**, 3146 (1998).
21. N. L. Pocard, D. C. Alsmeyer, R. L. McCreery, T. X. Neenan, and M. R. Callstrom, *J. Am. Chem. Soc.*, **114**, 769 (1992).
22. M. R. Callstrom, T. X. Neenan, R. L. McCreery, and D. C. Alsmeyer, *J. Am. Chem. Soc.*, **112**, 4955 (1990).
23. W. Chrzanowaki and A. Wieckowski, *Langmuir*, **14**, 1967 (1998).
24. W. Chrzanowaki and A. Wieckowski, in *Interfacial Electrochemistry: Theory, Experiment, and Applications*, A. Wieckowski, Editor, Marcel Dekker, New York, 937 (1999).
25. W. Chrzanowski, H. Kim, G. Tremiliosi-Filho, A. Wieckowski, B. Grzybowska, and P. Kulesza, *J. New Mater. Electrochem. Sys.*, **1**, 31 (1998).
26. N. M. Markovic, H. A. Gasteiger, and P. N. Ross, Jr., *J. Phys. Chem.*, **99**, 3411 (1995).
27. N. Markovic, H. Gasteiger, and P. N. Ross, *J. Electrochem. Soc.*, **144**, 1591 (1997).
28. J. Perez, E. R. Gonzalez, and E. A. Ticianelli, *Electrochim. Acta*, **44**, 1329 (1998).
29. T. Yano, E. Popa, D. A. Tryk, K. Hashimoto, and A. Fujishima, *J. Electrochem. Soc.*, **146**, 1081 (1999).
30. T. Yano, D. A. Tryk, K. Hashimoto, and A. Fujishima, *J. Electrochem. Soc.*, **145**, 1870 (1998).

Ch

Fa

Di

El

El

4.1

lab

co

is

it

co

et

an

ch

st

pr

an

the

co

Chapter 4

Fabrication and Characterization of Dimensionally Stable Pt/Diamond Composite Electrodes for Electrocatalysis — The Electrodeposition Approach

4.1 Introduction

A new type of carbon electrocatalyst support/host is under development in our laboratory; electrically conducting diamond thin films.^{1,2} The use of electrically conducting microcrystalline and nanocrystalline diamond electrodes in electrochemistry is a relatively new field of research.³⁻⁸ The properties of this new electrode material make it ideally suited for electrochemical applications, particularly demanding ones (*i.e.*, complex matrix, high current density, and potential, high temperature, extremes in pH, etc.).

The preparation technique is crucial in order to improve both the catalytic activity and reduce the cost of the diamond film supported noble metal catalyst. In the preceding chapter, we demonstrated that nanometer-sized Pt particles could be incorporated into the surface microstructure of boron-doped diamond thin films via a multistep fabrication procedure. The dispersed Pt particles were achieved by magnetron sputtering deposition and further stabilized by the growth of a thin film of diamond around their base. While the catalyst particles are stably anchored, the magnetron sputtering approach affords poor control over the particle size and distribution.

m

e

a

l

n

th

e

d

a

n

a

a

i

s

.

n

s

f

c

f

The preparation of supported catalyst nanoparticles using electrochemical methods has recently attracted much attention.⁹⁻¹⁴ Compared with methods involving evaporation of metal in vacuum, electrodeposition is a relatively simple, cost-efficient, and versatile technique that allows the preparation of large bulk samples with high purity, low porosity, and enhanced thermal stability.¹² Furthermore, the control of the nanomaterial properties, e.g., grain size, distribution, and crystallite shape, is possible through manipulation of the deposition conditions. There is another nice feature of the electrochemical procedure with respect to electrocatalysis. Metal particles are exclusively deposited on the active sites of the support material where both facile electron transfer and electrolyte accessibility are possible. Hence, the incorporation of unusable noble metal catalyst, a problem often encountered during the preparation of current state-of-the-art electrodes, is avoided, and the overall catalyst cost is substantially reduced.

The control over the particle size and distribution via an electrodeposition approach is apparent in the electrochemical version of the Gibbs-Thomson equation:^{14,15}

$$r_c = \frac{2\sigma V_m}{ze|\eta|} \quad (4.1)$$

in which r_c is the size of critical nucleus (grains with $r > r_c$ are stable), σ the specific surface energy, V_m the atomic volume in the crystal lattice, z the number of electrons, and η the overpotential. One can see that high overpotential is necessary to maintain a high nucleation rate in order to achieve small particles. However, the nucleation rate is strongly limited by the rapid buildup of a depletion layer in the vicinity of the electrode at high overpotential. Therefore, either forced convection in constant current/potential mode or pulsed current/potential should be applied in order to minimize the concentration polarization.

using

com

dop

fron

con

gre

wi

T

e

F

n

t

4

s

In this chapter, we report on the fabrication of Pt/diamond composite electrodes using an electrodeposition approach. The same multistep procedure for fabricating the composite electrode was employed. The dispersion of Pt nanoparticles onto the boron-doped diamond thin film surface was accomplished by galvanostatic electrodeposition from a dilute PtCl_6^{2-} solution. The size and distribution of the metal particles can be controlled, to some extent, by adjusting the electrodeposition and secondary diamond growth conditions. Potentiodynamic deposition of the metal was also investigated and will be briefly discussed herein, but was found to be inferior to galvanostatic deposition. The morphology, microstructure, and catalytic activity of the composite electrodes were examined by scanning electron microscopy (SEM), atomic force microscopy (AFM), powder x-ray diffraction (XRD), Raman spectroscopy, and cyclic voltammetry (CV), respectively. The resulting Pt/diamond composite electrodes have metal catalyst particles that are strongly anchored into the surface microstructure, and are extremely stable with unchanging catalytic activity even after 2 h of anodic polarization in 85% H_3PO_4 at 170°C and $0.1 \text{ A}\cdot\text{cm}^{-2}$. An acid etching experiment confirmed that the secondary diamond deposition results in film growth around the base of the metal deposits, stably anchoring them into the surface microstructure.

4.2 Experimental

Preparation of Pt/diamond composite electrodes. Diamond thin films were deposited by microwave-assisted chemical vapor deposition (1.5 kW, 2.54 GHz, ASTeX, Inc., Lowell, MA) on highly conducting p-Si (100) substrates ($\sim 10^{-3} \text{ }\Omega\cdot\text{cm}$). The substrates (0.1 cm thick x 1 cm^2 in area, Virginia Semiconductor, Inc.) were pretreated by rinsing in toluene, methylene chloride, acetone, isopropanol and methanol. They were

then etched in concentrated HF for 60 s, rinsed with ultrapure water and air dried. The cleaned substrates were then sonicated in a diamond powder/acetone slurry (0.1 μm diam., GE Superabrasives, Worthington, OH) for 20 min. followed by a rinse with clean acetone. The sonication scratches the surface and leaves “seed” crystals ($>10^8$ particles/ cm^2), both of which serve as nucleation sites during film growth. The seeded substrates were then placed in the CVD reactor and the system pressure reduced to about 10 mTorr. Ultrahigh-purity (99.999%) methane and hydrogen were used as the source gases. The hydrogen flow rate was 200 sccm and the methane flow rate was 0.70 sccm during the deposition. Prior to introducing methane, the substrates were heated to the growth temperature in a hydrogen plasma for 10 min. The plasma was formed with a system pressure of 40 Torr and a power of 1000 W. The substrate temperature was approximately 850 $^\circ\text{C}$, as measured using a disappearing filament optical pyrometer. The films were doped using solid-state boron dopant sources: a boron diffusion source (GS-126, BoronPlusTM, Techniglas, Inc., Perrysburg, OH) and a small piece of boron nitride (Goodfellow, Ltd., England). Boron dopant concentrations were estimated to be approximately 10^{19} to 10^{20} B/ cm^3 (300~3000 ppm B/C), based on boron nuclear reaction analysis of other films deposited using similar conditions. The apparent in-plane film resistivities ranged from 0.1 to 0.01 $\Omega\text{-cm}$, and were measured using a tungsten four-point probe (0.1 cm probe spacing) with the diamond film attached to the conducting Si substrate.

The fabrication of the Pt/diamond composite electrode follows the same stepwise procedure as described in the previous chapter, except that the substrate was the Si (100) and the Pt was deposited electrochemically. A boron-doped diamond thin film was

initially deposited onto a Si(100) substrate for 12 h. The thickness of the film was about 4-6 μm . The diamond growth was then stopped and the substrate cooled to less than 300 $^{\circ}\text{C}$ in the presence of atomic hydrogen. After completely cooling to room temperature, the coated substrate was removed from the reactor. Metal particles were then electrodeposited onto the surface, galvanostatically, from 1 mM K_2PtCl_6 + 0.1 M HClO_4 at 0.5 mA/cm^2 . Both diffusion and convection influenced the deposition as nitrogen was slowly bubbled through the solution during the process. This current, and all others in the text unless otherwise stated, are normalized to the geometric area of the electrode (0.2 cm^2). Four diamond films from the same batch were employed using Pt deposition times of 100, 200, 300, and 400 s each. Some experiments involved potentiodynamically depositing the metal particles from the same solution while scanning the potential between 0.8 and -0.3 V vs. Ag/AgCl at 50 mV/s . The Pt-coated film was then placed back in the reactor and boron-doped diamond deposited for additional 1-3 h, using the same conditions as described above. During this step, the diamond film grows around the base of the particles, anchoring and stabilizing them within the surface microstructure. The secondary diamond film thickness is less than 1 μm .

Film characterization. The atomic force microscopy (AFM) was performed with a Nanoscope II instrument (Digital Instruments, Santa Barbara, CA) in the contact mode. Pyramidal Si_3N_4 tips, mounted on gold cantilevers (200 μm legs, 0.38 N/m spring constant), were used to acquire topographical images in air. Raman spectra were obtained at room temperature with a Chromex RAMAN 2000 system (Chromex Inc., Albuquerque, NM) consisting of a diode-pumped, frequency-doubled CW Nd:YAG laser (500 mW at 532 nm, COHERENT), a Chromex 500is spectrometer ($f/4$, 600 grooves/mm

holographic grating), and a thermoelectrically-cooled 1024 x 256 CCD detector (ANDOR Tech., Ltd.). Spectra were collected with an incident power density of ca. 500 kW/cm² (100 mW at the sample and 5 μm diam. spot size).

Electrochemical measurements. The Pt electrodeposition and cyclic voltammetry were performed in a single-compartment glass cell using a CYSY-2000 computer-controlled potentiostat (Cypress Systems, Inc., Lawrence, KS). A Ag/AgCl (in sat. KCl) electrode was used as the reference and a large-area carbon rod served as the counter electrode. The Pt/diamond composite working electrode was pressed against the bottom of the glass cell using an Al plate current collector with the fluid being contained by a Viton[®] o-ring. Silver paste was applied to the center portion of the backside of the Si substrate, after cleaning for electrical connection. The electrode's geometric area was 0.2 cm², and all currents are normalized to this area. The diamond film working electrode was cleaned, once mounted in the cell, by a thorough rinse with ultrapure water (>17 MΩ-cm, Barnstead E-Pure), a 20-min. soak in distilled isopropanol, followed by another thorough rinse with ultrapure water. The electrolyte was deoxygenated with nitrogen (99.9%, BOC Gases) for 20 min. prior to any electrochemical measurements, and the solution was blanketed with the gas during the measurements.

Chemicals. All chemicals were reagent-grade quality or better, and used without additional purification. The HClO₄ (Aldrich) was ultrahigh purity (99.999%). The HCl (Aldrich), HNO₃ (Aldrich), H₃PO₄ (Aldrich), and K₂PtCl₆ (Aldrich) were all of reagent grade quality. All solutions were prepared with ultrapure water from a Barnstead E-Pure purification system (>17 MΩ-cm).

4.3 Results and Discussion

4.3.1 Electrodeposition of Pt on Diamond Thin Films

Both potentiodynamic and galvanostatic deposition of Pt were investigated in order to examine the influence of the deposition method and conditions upon the morphology, size, and distribution of the metal deposits.

Potentiodynamic deposition. Figure 4.1A shows cyclic voltammetric i-E curves obtained during the metal deposition in 1mM K₂PtCl₆ + 0.1M HClO₄. A total twenty-five potential sweeps were made and the i-E curves for the 1st, 5th, 10th, 15th, 20th and 25th scans are presented. The potential sweep was initiated at 800 mV and scanned in the negative direction to -300 mV at a scan rate of 50 mV/s. During the first cycle (innermost curve), the cathodic current for the metal deposition begins to gradually increase at ca. 350 mV vs. Ag/AgCl, with the significant current onset at 0 mV. Based on the redox reaction,¹⁶



this represents an overpotential of over 200 mV for the deposition of Pt on diamond. The result is in agreement with the observation of copper electrodeposition. The large overpotential is attributed, in a very general way, to the inertness of hydrogen-terminated diamond surface. The metal deposition likely proceeds by two irreversible reactions, corresponding to sequential two-electron transfers ($\text{PtCl}_6^{2-} \rightarrow \text{PtCl}_4^{2-} \rightarrow \text{Pt}$), as has been proposed for Pt electrodeposition on carbon fiber electrodes.¹⁷ The reactions occur at potentials sufficiently close such that each step was not well resolved for diamond (50 mV/s). The reduction peak at -240 mV is attributed to the adsorption of hydrogen on the electrodeposited Pt particles, a reaction that is occurring simultaneously with the metal

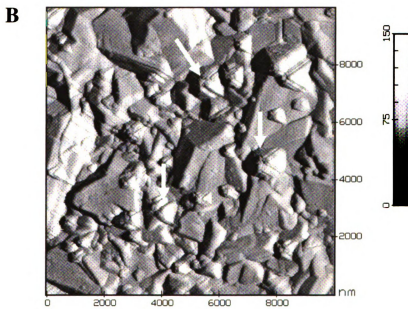
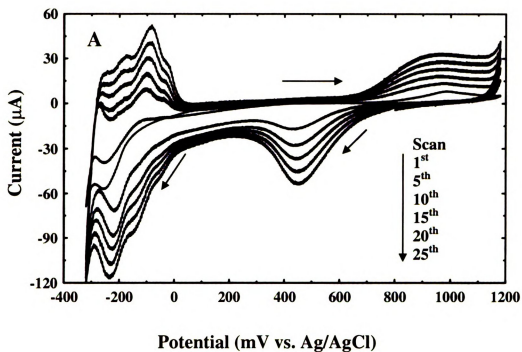


Figure 4.1. (A) Successive potentiodynamic i-E curves for a boron-doped diamond thin film in 1mM K_2PtCl_6 + 0.1M $HClO_4$. Scan rate = 50mV/s. (B) AFM force-mode image (air) of the diamond thin film after 25 potential cycles.

deposition. The current crossover seen during the reverse sweep is a characteristic feature of metal nucleation and growth.¹⁸ The voltammetric currents grow with cycle number (the 25th scan is the outermost curve) due to the progressive increase in metal particle size and distribution. All voltammograms, after the initial one, show the characteristic current features for Pt: Pt oxide formation (700 – 1200 mV), oxygen evolution (1200 mV), Pt oxide reduction (500 mV), hydrogen adsorption and desorption (0 – -300 mV), and hydrogen evolution (-300 mV).

Figure 4.1B shows a top-view, $10 \times 10 \mu\text{m}^2$ AFM image (force mode, air) of the diamond surface after 25 potential cycles. A well-faceted, polycrystalline film morphology is observed with cubic, octahedral, and cubo-octahedral microcrystallites. Also present are the intercrystalline grain boundaries where the microcrystallites join together. The Pt deposits are not uniformly distributed over the surface but rather are located almost exclusively at grain boundaries and other visible extended defects (see arrows). The particle diameters range from 0.3 to 2 μm with a distribution density of ca. $4 \times 10^7 \text{ cm}^{-2}$ (geometric area). After 25 potential cycles, most of the surface is still void of Pt and many of the particles have diameters up to ca. 2 μm . These observations, and others, suggest that the metal deposition preferentially initiates, under these conditions, at the grain boundaries, or other surface defects during the first cathodic scan, with a limited number of Pt nuclei formed. 3D growth of the metal particles from these nuclei then dominates the successive potential sweeps.

Galvanostatic deposition. It is clear the potentiodynamic deposition produced particles with large diameters and poor distribution. A recent study has demonstrated that constant current, as well as pulsed current, deposition can be used to successfully prepare

highly dispersed Pt nanoparticles on porous carbon substrates.¹⁴ Galvanostatic deposition of Pt was carried out in 1mM K₂PtCl₆ + 0.1M HClO₄ with a constant current density of 0.5 mA·cm⁻². Forced convection (N₂ bubbling) was employed in order to maintain the electrode potential between from -100 to -300 mV vs. Ag/AgCl during the deposition. Figure 4.2A-D shows top-view, 10 × 10 μm² AFM images (force mode, air) of diamond surfaces after deposition for 100, 200, 300, and 400 s, respectively. The nominal particle size, variances, and distribution density for each deposition time are summarized in Table 4.1.

The metal particles decorate the entire surface with much better distribution than was achieved with the potentiodynamic method. The nominal particle size is also smaller. Both are desirable trends for a catalytic electrode. After 100 s of deposition (Figure 4.2A), distinguishable Pt particles are uniformly dispersed over the diamond surface decorating both the microcrystallite facets and the grain boundaries. The particle size ranges from 20-200 nm with an average particle distribution of $0.5 \times 10^9 \text{ cm}^{-2}$. The distribution was determined by manually counting the particles in AFM images from multiple sites on the surface. Slightly higher distribution is observed after 200 s of deposition (Figure 4.2B). The particle size ranges from 10 – 250 nm and the distribution increases to $0.8 \times 10^9 \text{ cm}^{-2}$. A further increase in the distribution is seen after 300 s of deposition (Figure 4.2C). The particle size ranges from 50 - 300 nm and the distribution is $1.0 \times 10^9 \text{ cm}^{-2}$. Finally, somewhat larger particles and a higher distribution are observed after 400 s of deposition (Figure 4.2D). The particle size ranges from 60 - 500 nm and the distribution is $1.2 \times 10^9 \text{ cm}^{-2}$. The image features are consistent with a progressive nucleation and 3D growth mechanism,¹⁸ in which new Pt nuclei form progressively as a

function of time while the existing nuclei increase in size. Nuclei form on both the grain boundaries and the facet surfaces. This indicates that both regions are electrochemically active and support the flow of current.

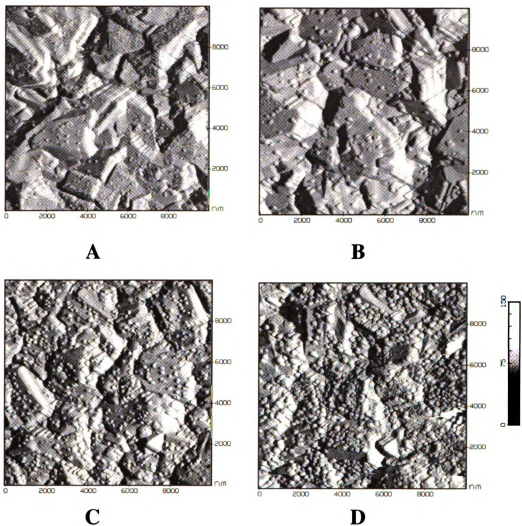


Figure 4.2. AFM force-mode images (air) of boron-doped diamond thin films after galvanostatic deposition of Pt from a solution of 1 mM K_2PtCl_6 + 0.1M $HClO_4$. The deposition times are (A) 100, (B) 200, (C), 300 and (D) 400 s, respectively.

Table 4.1. Pt particle size, distribution, hydrogen desorption charge and roughness factor (RF) for the Pt/diamond composite electrodes before and after the secondary diamond growth.

Deposition Time (s)	Before				After				Surface Loss (%)
	Particle Size (nm)	Distribution Density (10^9cm^{-2})	Hydrogen Desorption Charge (mC/cm^2)	RF	Particle Size (nm)	Distribution Density (10^8cm^{-2})	Hydrogen Desorption Charge (mC/cm^2)	RF	
100	20-200	0.5 ± 0.10	0.51	2.4	30-250	3.0 ± 1.5	0.32	1.5	37.3
200	10-250	0.8 ± 0.04	0.80	3.8	50-300	5.1 ± 0.7	0.56	2.7	30.0
300	50-300	1.0 ± 0.05	1.19	5.7	50-350	8.0 ± 0.3	0.81	3.9	31.9
400	50-500	1.2 ± 0.09	1.43	6.8	60-500	8.5 ± 0.4	0.92	4.4	35.7

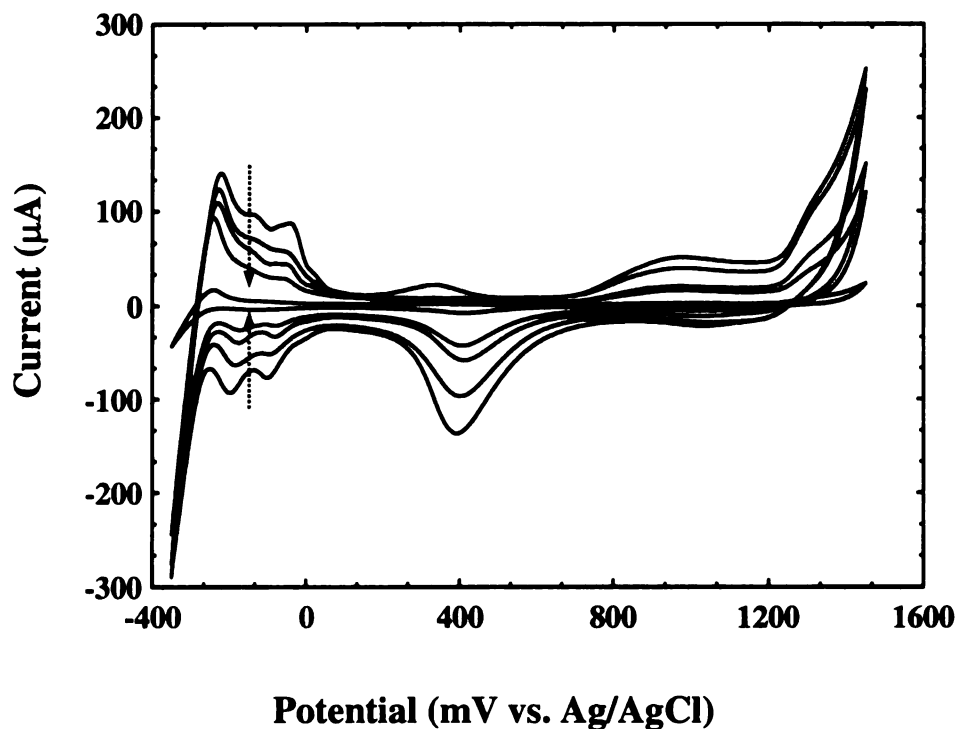


Figure 4.3. Cyclic voltammetric i-E curves in 0.1 M HClO₄ for a boron-doped diamond thin film electrodeposited with Pt, during 1000 potential cycles between -400 and 1500 mV vs. Ag/AgCl at 50 mV/s. Dashed arrows show the decrease in current response with scan number. The maximum anodic and/or cathodic current density during the cycling was ca. 1 mA/cm².

Stability of the electrodeposited Pt particles. Weak adhesion of electrodeposited metal particles to the diamond surface is a common observation,^{19,20} which is presumably attributed to the lack of strong interaction between the deposits and the non-polar, hydrogen-terminated diamond surface. The stability of the electrodeposited Pt particles was investigated, immersing the coated film in 0.1 M HClO₄ and applying a series of potential cycles between -400 and 1500 mV vs. Ag/AgCl. These potentials were extreme enough to result in the cyclic generation of oxygen and hydrogen gas. One

thousand cycles were performed at a scan rate of 50 mV/s. Figure 4.3 shows a series of cyclic voltammetric i-E curves recorded during the cycling period. There is a progressive loss of the Pt features with cycle number. The hydrogen desorption charge prior to cycling is $800 \mu\text{C}/\text{cm}^2$ and decreases significantly to $25 \mu\text{C}/\text{cm}^2$ after cycling. This represents a decrease of over 96%. The loss of electrodeposited Pt results from the turbulence of the gas evolution, which physically dislodges the weakly adhering deposits.

4.3.2 Secondary Diamond Growth

Structural characterization. The secondary diamond growth is necessary to stabilize the electrodeposited Pt particles by anchoring them into the surface microstructure. The secondary growth is accomplished by placing the Pt-coated film back into the CVD reactor and depositing boron-doped diamond for a short period of time, such that the film does not completely cover the metal particles but only surrounds their base. Figure 4.4A-D shows $5 \times 5 \mu\text{m}^2$ AFM images (force mode, air) of Pt-coated films after 3 additional hours of diamond growth. The images are of the same Pt-coated films shown in Figure 4.2. Numerous particles are randomly distributed over the surface on both the microcrystallite facets and in the grain boundaries, particularly for 200, 300, and 400 s electrodeposition times. The nominal particle size is slightly increased by the secondary diamond growth, ranging from 30 - 500 nm, but the distribution is lower. The process of entrapping the particles with diamond reduces the total active Pt exposed. This is seen by comparing the hydrogen desorption charge in Table 4.1. There is a 30-37% loss in Pt activity, as measured in the hydrogen desorption voltammetric charge between

0 and -300 mV. This is consistent with the secondary diamond growth around the base of the metal deposits. The loss is further discussed below.

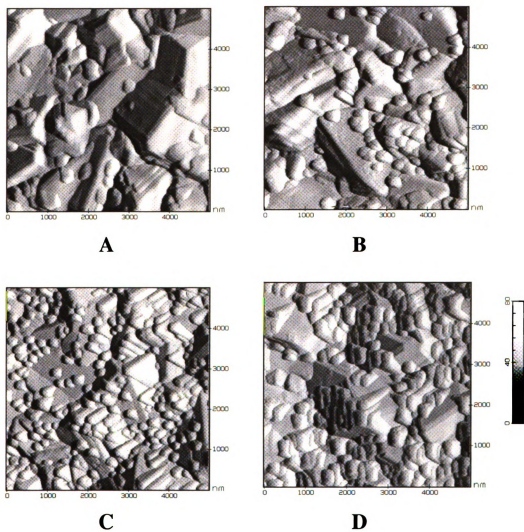


Figure 4.4. AFM force-mode images (air) of Pt coated diamond thin films (as indicated in Figure 4.2) after a 3 h secondary diamond growth. The corresponding Pt deposition times are (A) 100, (B) 200, (C), 300 and (D) 400 s, respectively.

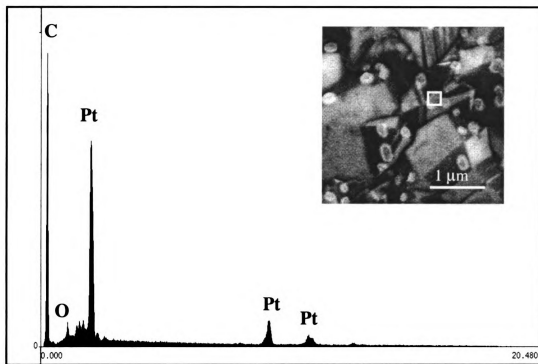


Figure 4.5. Energy dispersive x-ray analysis spectrum for a Pt metal particle shown in the SEM image (inset).

SEM and semiquantitative x-ray fluorescence measurements confirmed the deposits are Pt. Figure 4.5 shows an SEM image of a composite diamond film and the corresponding energy dispersive x-ray analysis spectrum taken from one of the metal deposits on the film surface. The deposits occupy sites on both the facet surfaces and in the grain boundaries. As stated above, this general observation indicates that both the grains and the grain boundaries are electrically conductive with a low nominal resistance to the flow of current. It is most probable that film defects serve as the nucleation sites for metal deposition. The C $K\alpha$ (0.277 KeV), O $K\alpha$ (0.525 KeV) and Pt $M\alpha$ (2.05 KeV), $L\alpha$ (9.44 KeV) emissions are observed in the EDX spectrum. The estimated atomic

percentage of each element is 94, 2, and 4, respectively, yielding Pt/C and O/C atomic ratios of 0.04 and 0.02.

The x-ray diffraction spectrum (Cu source) of a Pt/diamond composite electrode is presented in Figure 4.6, revealing the primary crystallographic orientations of the Pt particles and the diamond microcrystallites. The Pt electrocatalyst displayed the characteristic diffraction peaks of the Pt fcc structure, i.e., peaks at 40.2 degrees (111-orientation), 46.6 degrees (200-orientation), and 67.8 degrees (220-orientation). It is clear that the diamond (111) orientation dominates in the film, with strong diffraction intensity observed at 44.2 degrees. These data confirm the crystalline nature of the diamond and the incorporated Pt particles.

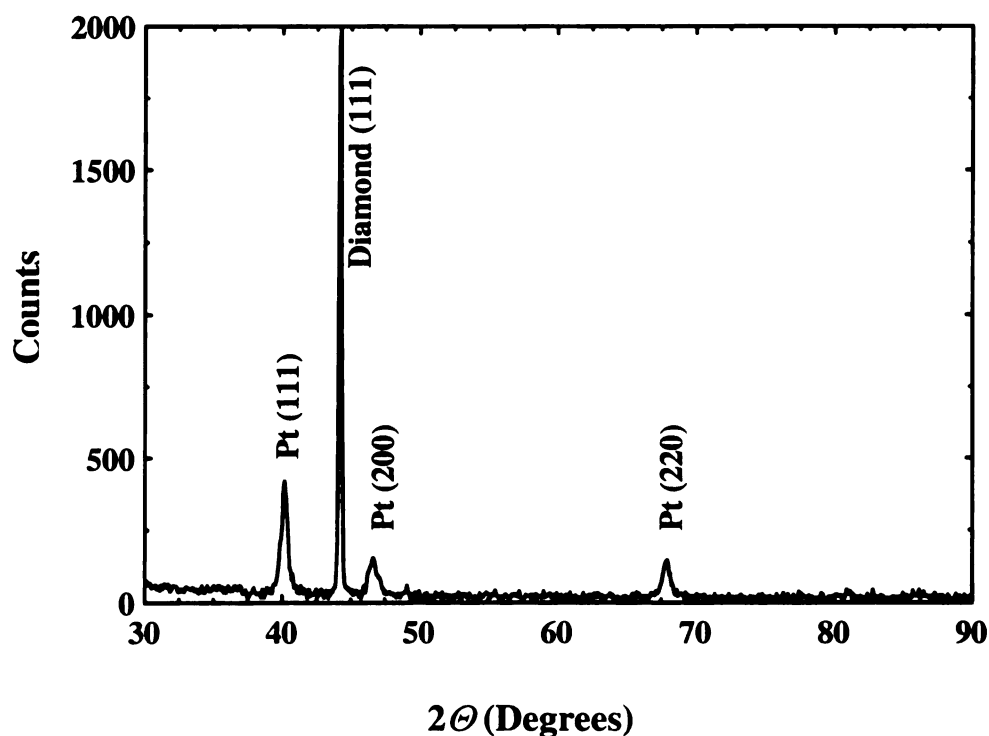


Figure 4.6. XRD pattern of a Pt/diamond composite electrode.

Basic electrochemical properties. Figure 4.7 shows the typical cyclic voltammetric i-E curves for the Pt/diamond composite electrode in N₂-purged 0.1 M HClO₄, before and after the secondary diamond growth. The potential sweep was initiated at 200 mV and scanned in the positive direction at a scan rate of 50 mV/s. All the characteristic current features of polycrystalline Pt are present. Two reversible hydrogen adsorption/desorption peaks are evident in the potential region from 0 and -300 mV.

Integration of the area under these peaks can be used to estimate the electrochemically active surface area (or real surface area) of the Pt particles using the equation²¹

$$S_r = \frac{Q_m}{ed_m} \quad (4.3)$$

in which S_r is the real surface area, Q_m is the charge associated with the formation of a monolayer of adsorbates, e is the electron charge, and d_m is the surface metal atom density.

In the case for Pt, d_m takes a value of $1.3 \times 10^{15} \text{ cm}^{-2}$, then

$$S_r (\text{cm}^2) = \frac{Q_m (\mu\text{C})}{210 (\mu\text{C} \cdot \text{cm}^{-2})} \quad (4.4)$$

From the knowledge of S_r , the roughness factor ρ can be calculated as

$$\rho = \frac{S_r}{S_g} \quad (4.5)$$

where S_g is the geometric area of the diamond electrode.

The results are presented in Table 4.1. Both the hydrogen desorption charge and the roughness factor increase with the deposition time (i.e., Pt loading). Assuming a

100% current efficiency, the mass of Pt deposited is calculated to be 25.2, 50.3, 75.8 and 100.1 $\mu\text{g}\cdot\text{cm}^{-2}$ for the 100, 200, 300 and 400 s deposition times, respectively. Thus, the hydrogen desorption charge per mass of Pt, after the secondary diamond growth, is calculated to be 12.6, 11.1, 10.7, and 9.2 $\text{C}\cdot\text{g}^{-1}$, respectively. The decreasing ratio reflects the increasing nominal metal particle size.

The voltammetric curve for the Pt-coated diamond film, prior to the secondary growth (solid line), was obtained after the first scan, and the shape remained unchanged during 10 subsequent scans. However, the voltammetric curve for the Pt-coated diamond film, after the secondary diamond growth (dashed line), had a poor first scan, especially in the hydrogen adsorption/desorption region. In fact, many scans (100 cycles) were required for the characteristic Pt features to develop. This observation is consistent with the removal of surface contamination formed during the diamond deposition. It is highly probable that some of the Pt surfaces are initially covered with adsorbed carbon and/or hydrocarbon moieties, and these contaminants block surface sites for the hydrogen adsorption. The contaminants are effectively removed by potential cycling between the oxygen and hydrogen evolution regimes¹. Hence, potential cycling is the normal protocol for cleaning and activating the Pt surface after the secondary diamond film growth. The potential cycling (50-100 cycles) is performed in 0.1M HClO_4 at scan rate of 50 mV/s between -400 mV and 1500 mV. The voltammogram shown for the Pt-diamond composite electrode is for the 100th cycle. The flat oxide-formation region at potentials between 700 and 1200 mV indicates that the oxidation of adsorbed contaminants is not occurring to any appreciable extent.

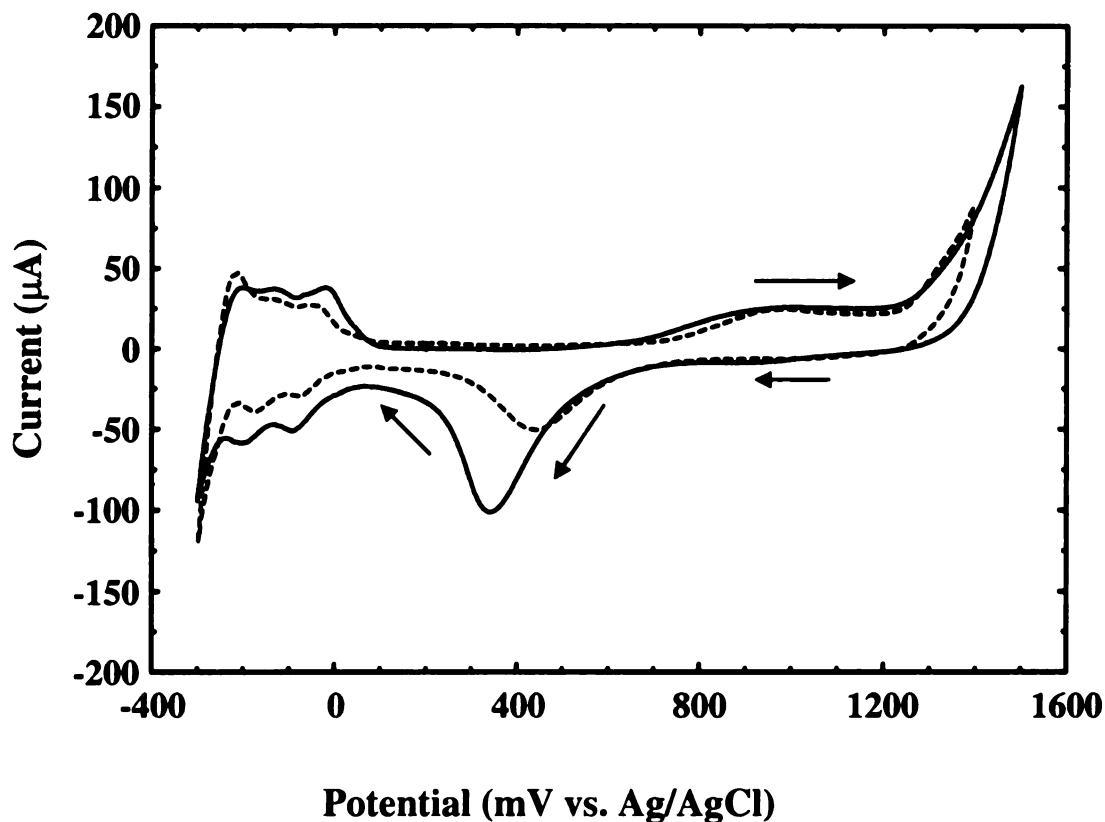


Figure 4.7. Cyclic voltammetric i-E curves for a Pt-coated diamond thin film in 0.1M HClO₄ before (solid line) and after (dashed line) a 3 h of secondary diamond growth. The Pt deposition time was 200s. Scan rate = 50 mV/s.

There are, however, some notable differences between the two voltammograms. The hydrogen adsorption/desorption peaks, the Pt oxide formation/reduction waves, and the double-layer charging current between 100 and 250 mV are reduced after the secondary diamond growth, indicating a reduction in the active Pt surface area. As indicated in Table 4.1, an average of 34% of the active surface atoms are lost, based on the reduction in the hydrogen desorption charge.

Mechanistic aspects of secondary diamond growth. Several possible causes for the reduced Pt activity were systematically investigated. One possibility was particle

aggregation on the diamond surface at the deposition temperature of ca. 850 °C. Another possibility was gasification or sputtering of the Pt by the atomic hydrogen present in the plasma. An experiment was performed to examine these two possibilities, in which another set of Pt-coated diamond films, similar to those shown in Figure 4.2, were placed into the CVD reactor. The electrodes were then exposed to the conditions used for the secondary diamond growth except that no CH₄ was added. The absence of CH₄ did not significantly affect the substrate temperature, at least as determined by an optical pyrometer. Again the morphology was examined by AFM and the active surface area was determined from the hydrogen adsorption/desorption voltammetric charge in 0.1M HClO₄ before and after a 3-h hydrogen plasma treatment. No significant change in either the particle size or voltammetric charge for hydrogen desorption was observed (AFM images not shown here), at least for Pt particles with diameters from 20 to 300 nm. Therefore, the loss in active Pt was not due to particle aggregation, gasification or sputtering. Voltammetric measurements indicated that only 2-4%, not 30-37%, of the active Pt was lost during the 3-h hydrogen plasma treatment. The melting and smoothing of small particles may contribute to this slight activity loss. Although the melting temperature of bulk Pt is 1772 °C, nanometer-sized Pt particles have a much lower melting temperature, as indicated by the size-dependent melting temperature theory.²² As the size of the particle decreases, an increased proportion of atoms occupy surface or interfacial sites. These atoms are more loosely bound than bulk atoms, which facilitates the melting.²³ Pt particles with diameters of less than 2 nm have a melting point less than 850 °C, based on the application of the theory. It should also be noted that segregated Pt particles, rather than a continuous film, can be formed on different substrates by high

temperature annealing in vacuum.^{24,25} The break-up of an initially continuous or quasi-continuous Pt film into individual Pt aggregates on a quartz substrate has been achieved by vacuum heat treatment at 600 K.²⁴

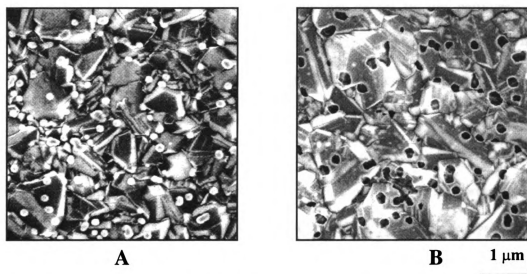


Figure 4.8. SEM images of a Pt/diamond composite electrode (A) before and (B) after etching in aqua regia. The Pt deposition time was 200 s.

Confirmation that the secondary diamond growth causes the loss of active Pt by covering the base of the metal deposits was next addressed. In the experiment, a Pt/diamond composite electrode was etched in hot aqua regia (3 HCl : 1 HNO₃ (v/v)) to dissolve the Pt particles. The diamond lattice is quite stable in this solution and undergoes no morphological alteration. SEM images of the composite electrode, before and after the acid etching, are presented in Figure 4.8A and B. Pt particles with diameters of 50 - 300 nm are seen on the surface prior to the chemical treatment (Fig. 4.8A). Numerous pits are observed in the diamond film after treatment. These pits are the voids left after dissolving the metal, and have diameters of approximately the same range. This observation confirms that the diamond film does surround the base of the metal particles entrapping

and anchoring them in the surface microstructure. The depth of the pits depends on the secondary diamond growth time.

The secondary diamond growth can also completely cover some of the small Pt particles, once the thickness of the film exceeds the height of the particles. This postulation has been confirmed by the cross-section analysis using SEM. Figure 4.9A shows a cross sectional image of an acid-etched Pt/diamond composite electrode. The corresponding back scattering SEM image is shown in Figure 4.9B. Elements with higher atomic number yield brighter images than lighter elements in the back-scattered electron imaging mode. Three bright spots are observed in Figure 4.9B, which corresponds to three metal particles indicated as 1, 2, and 3 in Figure 4.9A. EDX analysis further confirmed the particles are Pt. The fact that these particles were not dissolved during the acid-etching procedure indicates they are completely covered by the corrosion-resistant diamond film.

The thickness of the secondary diamond film, and thus the growth rate, can be estimated from the vertical distance between the film surface and the bottom of the particles or the pit (see arrow 4). The growth rate, ca. $0.04\text{-}0.1\ \mu\text{m}\cdot\text{h}^{-1}$, is far less than the growth rate, ca. $0.3\ \mu\text{m}\cdot\text{h}^{-1}$, generally observed for diamond growth on Si in our reactors. Mechanistic studies are in progress focused on understanding the influence of the foreign metal particles on the diamond nucleation and growth. It is supposed that the above observations are attributable to at least two reasons. First, the diamond nucleation and growth rate, in the presence of Pt, is rather low. The assessment is based on observations made by Belton et al.,²⁶ and Tachibana et al.²⁷ during the study of diamond growth on Pt.

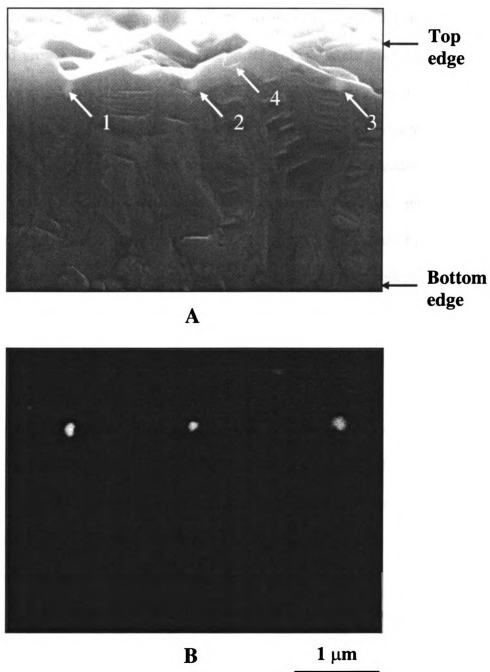


Figure 4.9. Cross-sectional SEM images of an acid-etched Pt/diamond composite electrode. (A) Secondary electron imaging mode. (B) Back-scattered electron imaging mode. The secondary diamond growth time was 3 h. Arrow 1-3 show three Pt particles covered by the diamond film. Arrow 4 shows a cavity after dissolving Pt.

Pt could catalyze the conversion of diamond to graphite, a process that competes with the diamond growth. The early stage of diamond growth likely involves the formation of thin-layer of graphitic carbon on the Pt surface, followed by etching of surface graphite and formation of adsorbed hydrocarbon deposits as the growth continues. Therefore, the fact that sufficient time is needed to etch the graphitic species, leads to an apparent low growth rate during the early stage. Second, an “undergrowth” mechanism may be involved. As demonstrated in the electrochemical study, the hydrogen-terminated diamond surface lacks anchoring sites to stabilize the electrodeposited Pt particles. Therefore, the secondary diamond film could be deposited beneath the particles, as well as surrounding the base.

4.3.3 Stability of the Pt/Diamond Composite Electrode

The dimensional stability of the Pt/diamond composite electrodes was examined during a 2-h exposure to 85% H₃PO₄ acid at 170 °C and 0.1A/cm². Electrochemical and AFM measurements revealed no loss in Pt activity and no degradation of the diamond microstructure after 2 h of electrolysis.

Figure 4.10 shows cyclic voltammetric i-E curves for a Pt/diamond composite electrode in 0.1 M HClO₄ before and after two 1-h periods of anodic polarization. The curve for the electrode prior to the polarization (dashed line) reveals the presence of Pt with the expected features. After the two 1-h polarizations, the voltammetric features are unchanged and revealing that there is no loss of catalyst activity due to degradation of the diamond microstructure and morphology. Importantly, there is no loss in the charge associated with hydrogen ion adsorption and desorption. Such loss would be expected if

the Pt catalyst particles were detached from the surface due to an oxidizing and corroding diamond support. In fact, the charge associated with the hydrogen ion adsorption actually increases after the electrolysis. The cathodic charge is $355 \mu\text{C}\cdot\text{cm}^{-2}$ before and increases to 420 and $455 \mu\text{C}\cdot\text{cm}^{-2}$ after the two 1-h polarizations, respectively. The increased charge is attributed to minor surface cleaning and crystallographic changes in the deposits that occur during the vigorous gas evolution. One type of minor cleaning that is possible is the oxidative removal of residual carbon deposits formed during the secondary diamond deposition. These deposits do not affect the stability of the metal particles but, rather, influence their surface activity toward faradaic electron transfer processes. There is no significant change in the particle size and coverage after polarization, at least as revealed by AFM. Some representative images are shown below. The most significant change in the voltammograms is the reduced overpotential for oxygen evolution after the polarizations. The current associated with the Pt-oxide reduction increases after the electrolysis and the current maximum shifts to slightly more negative potentials. There is also a minor decrease in the overpotential for hydrogen evolution after the polarization.

Figure 4.11A and B show *ex situ* AFM images of the Pt/diamond composite electrode before and after the two 1-h polarizations. A well faceted, polycrystalline morphology is observed before and after electrolysis. The crystallites are randomly oriented with hemispherical Pt dispersions decorating both the facets and grain boundaries. Clearly, there is no evidence of any severe morphological or microstructural damage such as film delamination, grain roughening, or pitting. The similarity of the image features before and after polarization is consistent with the voltammetric data.

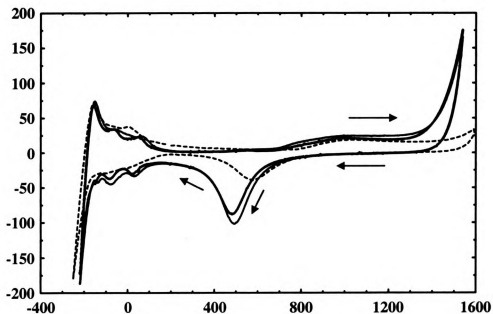


Figure 4.10. Cyclic voltammetric i-E curves for a Pt/diamond composite electrode in 0.1 M HClO₄ before (dashed line) and after two 1-h polarizations (solid lines) in 85 wt % H₃PO₄ at 170 °C and 0.1 A·cm⁻². The Pt deposition time was 200 s.

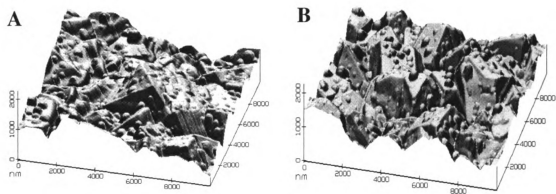


Figure 4.11. AFM images (air) of the Pt/diamond composite electrode (A) before and (B) after 2-h anodic polarization in 85 wt % H₃PO₄ at 170 °C and 0.1 A·cm⁻².

4.4 Conclusions

We report on a new, dimensionally stable Pt/diamond composite electrode that is fabricated by using a multistep procedure of diamond deposition, Pt electrochemical deposition, and diamond deposition. Dispersed Pt particles are galvanostatically deposited onto a boron-doped polycrystalline diamond thin-film surface and entrapped within the dimensionally stable microstructure by a subsequent diamond deposition. The second, short deposition serves to anchor many of the metal particles into the diamond microstructure by surrounding their base. The number of exposed particles, particle size, and distribution can be controlled, to some extent, by adjusting the galvanostatic deposition time and secondary diamond growth conditions. Particle sizes are in the range of 30 – 500 nm with a distribution of $\sim 10^9 \text{ cm}^{-2}$. This nominal particle size is still too large for a real catalytic electrode, and work is ongoing to reduce the particle size to the 10 nm range. About 34% of the active Pt surface is lost after the secondary diamond deposition due to a combination of complete coverage of some of the smaller particles and partial coverage of the base of the larger particles. The catalytic activity of the composite electrodes is extremely stable, as no microstructural alterations or activity losses were observed during a 2 h anodic polarization in 85% H_3PO_4 at $0.1 \text{ A}\cdot\text{cm}^{-2}$ and 170°C .

References:

1. J. Wang, G. M. Swain, T. Tachibana, and K. Kobashi, *Electrochem. Solid State Lett.*, **3**, 286 (2000).
2. J. Wang, G. M. Swain, T. Tachibana, and K. Kobashi, *J. New Mater. Electrochem. Sys.*, **3**, 75 (2000).
3. J. S. Xu, M. C. Granger, Q. Y. Chen, J. W. Strojek, T. E. Lister, and G. M. Swain, *Anal. Chem.*, **69**, A591 (1997).
4. G. M. Swain, A. B. Anderson, and J. C. Angus, *Mrs. Bulletin*, **23**, 56 (1998).
5. G. M. Swain, *J. Electrochem. Soc.*, **141**, 3382 (1994).
6. R. Tenne and C. Levy-Clement, *Israel J. Chem.*, **38**, 57 (1998).
7. Y. V. Pleskov, *Russian Chemical Reviews*, **68**, 381 (1999).
8. T. Yano, D. A. Tryk, K. Hashimoto, and A. Fujishima, *J. Electrochem. Soc.*, **145**, 1870 (1998).
9. J. V. Zoval, J. Lee, S. Gorer, and R. M. Penner, *J. Phys. Chem. B*, **102**, 1166 (1998).
10. J. V. Zoval, R. M. Sriger, P. R. Biernacki, and R. M. Penner, *J. Phys. Chem.*, **100**, 837 (1996).
11. H. Natter and R. Hempelmann, *J. Phys. Chem.*, **100**, 19525 (1996).
12. H. Natter, M. Schmelzer, and R. Hempelmann, *J. Mater. Res.*, **13**, 1186 (1998).
13. M. W. Verbrugge, *J. Electroanal. Chem.*, **141**, 46 (1994).
14. M. S. Loffler, B. Grob, H. Natter, R. Hempelmann, T. Krajewski, and J. Divisek, *Phys. Chem. Chem. Phys.*, **3**, 333 (2001).
15. E. Budevki, G. Staikov, and W. J. Lorenz, *Electrochemical Phase Formation and Growth*, VCH, New York, 1996.
16. A. J. Bard and L. R. Faulkner, *Electrochemical Methods, Fundamentals and Applications*, John Wiley & Sons, Inc, New York, 2001.
17. N. Georgolios, D. Jannakoudakis, and P. Karabinas, *J. Electroanal. Chem.*, **264**, 235 (1989).

18. B. Scharifker and G. Hills, *Electrochim. Acta*, **28**, 879 (1983).
19. S. Nakabayashi, D. A. Tryk, A. Fujishima, and N. Ohta, *Chem. Phys. Lett.*, **300**, 409 (1999).
20. N. Vinokur, B. Miller, Y. Avyigal, and R. Kalish, *J. Electrochem. Soc.*, **146**, 125 (1999).
21. J. M. D. Rodriguez, J. A. H. Melian, and J. P. Pena, *J. Chem. Ed.*, **77**, 1195 (2000).
22. K. F. Peters, J. B. Cohen, and Y. W. Chung, *Phys. Rev. B*, **57**, 13430 (1998).
23. M. Zhang, M. Y. Efremov, F. Schiettekatte, E. A. Olson, A. T. Kwan, S. L. Lai, T. Wisleder, J. E. Greene, and L. H. Allen, *Phys. Rev. B*, **62**, 10548 (2000).
24. W. Romanowski and R. Lamber, *Thin Solid Films*, **127**, 129 (1985).
25. E.I. Altman and R. J. Gorte, *Surf. Sci.*, **172**, 71 (1986).
26. D. Belton and S. Schmeig, *Surf. Sci.*, **233**, 131 (1990).
27. T. Tachibana, Y. Yokota, K. Miyata, T. Onishi, K. Kobashi, M. Tartutani, Y. Takai, R. Shimizu, and Y. Shintani, *Phys. Rev. B*, **56**, 15967 (1997).

Chapter 5

Oxygen Reduction Reaction on Pt/Diamond Composite Electrodes — A Rotating Disk Voltammetric Study

5.1 Introduction

The oxygen reduction reaction (ORR) is one of the most widely studied electrochemical reactions due to its considerable importance in several fields of research, including metal corrosion, electrolysis, and electrochemical energy conversion and storage.¹⁻⁴ Despite the considerable attention paid by electrochemists during the past three decades, the ORR remains an important field of research due to the complex reaction kinetics and the need for improved electrocatalysts.⁴ The reaction kinetics and mechanism are known to be influenced by several factors, including the type of cathode material (e.g., electrocatalyst), supporting electrolyte, and pH. For example, the reaction may involve a 2-electron pathway, in which oxygen is reduced to peroxide. This is the primary reaction on most carbon, gold, mercury, and transition-metal oxide electrodes.² The reaction may also involve a 4-electron pathway, in which oxygen is directly reduced to water. This is the primary reaction on noble metals (e.g. Pt, Pd, Ag), metal oxide, and some transition-metal macrocyclics.² The 4-electron pathway is preferred for many applications, such as fuel cells, because it leads to a high power density and a non-polluting final product (H₂O).

Platinum dispersed on high-surface-area carbon supports is still the best electrocatalyst employed in low temperature proton exchange membrane fuel cells (PEM-FC) for oxygen reduction. The ORR on Pt proceeds principally through the 4-electron pathway with a thermodynamic electrode potential of 1.23 V vs. SHE in acid solution (pH = 0).⁵ However, the electrode kinetics are rather slow at high potentials because of chemisorbed species on Pt surface (PtO and PtOH). The surface oxides inhibit the ORR and reduce the operating potential of the electrode to ca. 0.8 V vs. SHE.⁶ Since the overpotential for the anodic reaction is negligible when pure hydrogen is used as the fuel, the slow ORR kinetics is the major factor limiting the overall energy conversion efficiency in the PEM-FC.⁷ Another limitation is the susceptibility of the carbon support material to electrochemical corrosion. The oxygen cathode is exposed to oxidizing conditions, which can cause damaging corrosion of carbon, particularly at elevated temperatures.⁸ Electrochemical corrosion can limit the cathode potential and produce microstructural degradation and surface chemical changes, which cause significant loss in the catalytic activity.⁸

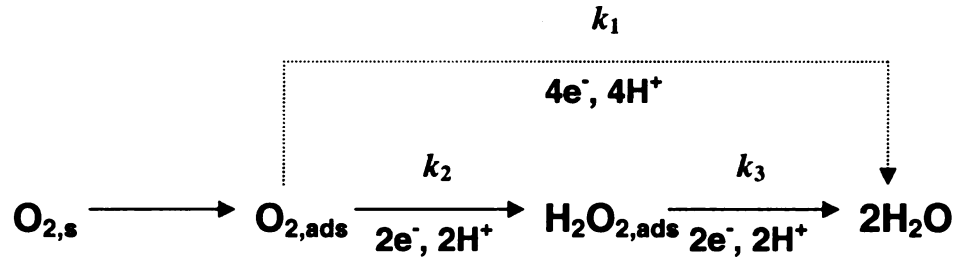
As described in Chapters 3 and 4, conductive diamond thin films are an advanced material that serves as a superb electrocatalyst support/host. Nanometer-sized Pt particles can be incorporated into the surface microstructure of boron-doped microcrystalline diamond thin films via a multistep diamond deposition/ Pt deposition/ diamond deposition procedure. The dispersed Pt particles are stabilized by the growth of a thin-film of diamond around their base and are in good electrical communication with the current collecting substrate through the boron-doped diamond base. The resulting dimensionally stable electrode can withstand high current densities ($\geq 0.1 \text{ Acm}^{-2}$), both

anodically and cathodically, without any morphological and microstructural degradation, even under demanding conditions (e.g., 85% H₃PO₄ and 170 °C).

In this chapter, results from the study of the ORR at Pt/diamond composite electrodes in acidic media using rotating disk voltammetry are presented. Rotating disk voltammetry is commonly used to study this reaction, because it allows for the separation of the mass-transfer effects from the electron transfer kinetics, and provides a measurement of the true catalytic activity.⁵ The composite films were deposited on molybdenum disks (5mm diameter) rather than Si wafers because of the hardness of the metal, which allows for the easy assembly as a rotating disk electrode (RDE). The open circuit potential was measured in oxygen-saturated 0.1 M H₃PO₄, H₂SO₄, and HClO₄ at room temperature. The kinetic parameters (e.g. Tafel slope and exchange current density) were determined as a function of the electrolyte composition and Pt loading in the same acid solutions.

5.2 Mechanism and Kinetics of ORR

Mechanism. The ORR on Pt in acid solution follows a complicated reaction mechanism which includes a number of elementary steps involving different reaction intermediates. A simplified reaction scheme is given below.⁴ The ORR proceeds through either a “direct” 4-electron pathway, in which oxygen is reduced to water with a rate constant, k_1 , without any intermediate formation, or a “series” 4-electron pathway, in which oxygen is first reduced to H₂O_{2,ads} with a rate constant, k_2 , and adsorbed peroxy species are further reduced to water with a rate constant, k_3 , before they desorb.



It is widely accepted that these two pathways generally occur simultaneously.⁴ However, the reaction rate is rather structure sensitive. Whether splitting of the O-O bond occurs before the peroxide formation is strongly dependent on the arrangement of the atoms on the electrode surface and anion adsorption. For example, strongly adsorbed Cl⁻ and Br⁻ can block the Pt sites needed for the dissociative chemisorption of O₂, favoring the “series” reaction pathway.^{9,10}

In either case, the following reaction steps take place⁴



Kinetics. The rate-determining step is the first charge transfer to O₂ (Reaction 5.2) with the approximate rate expression being¹⁰

$$i = nFkC_{\text{O}_2} (1 - \Theta_{\text{ad}})^x \exp\left(\frac{-\beta FE}{RT}\right) \exp\left(\frac{-\gamma r \Theta_{\text{ad}}}{RT}\right) \quad (5.4)$$

in which n is the number of electrons, k is the rate constant, C_{O₂} is the concentration of O₂ in the solution, Θ_{ad} is the total surface coverage by adsorbed species, x is the number

of Pt sites occupied by the adsorbed ion, β and γ are the symmetry factors (assumed to be $\frac{1}{2}$), and $r\Theta_{ad}$ is the parameter characterizing the rate of change of apparent standard Gibbs free energy of adsorption with the surface coverage by adsorbing species. In deriving equation 5.4, it is assumed that the reaction intermediates (e.g., $O_2^{\cdot-}_{ads}$, $HO_2^{\cdot-}_{ads}$ and $HO_2^{\cdot-}_{ads}$, etc) are adsorbed at low coverage, i.e. they are not a significant part of Θ_{ad} . Therefore, the kinetics of the ORR are largely determined either by free platinum sites available for adsorption of O_2 ($1-\Theta_{ad}$ term in Equation 5.4) and the Gibbs free energy of adsorption of reaction intermediates by adsorbing anions and/or surface oxides ($r\Theta_{ad}$ term in Equation 5.4). In other words, the case of $r = 0$ is synonymous with Langmuir adsorption conditions (i.e., no interaction takes place between the adsorbed molecules), whereas for $r \neq 0$ Temkin adsorption conditions are obtained (i.e., the Gibbs energy of adsorption of the reaction intermediates is dependent on the surface coverage of adsorbates).

5.3 Experimental

Electrode preparation. Diamond thin films were deposited on polycrystalline Mo disks following the same procedure as described in Chapter 4. The substrates (2 mm thick \times 5 mm in diameter, Aldrich, Inc.) were polished first with 800-grit sandpaper, then successively with Al_2O_3 water suspensions (particle size 1.0, 0.3, 0.05 μm), and cleaned ultrasonically in ultrapure water for 5 min after each polishing step. The substrates were rinsed in toluene, methylene chloride, acetone, isopropanol, and methanol. The cleaned substrates were then sonicated in a diamond powder/acetone slurry (0.1 μm diam., GE

Superabrasives, Worthington, OH) for 20 min followed by a rinse with clean acetone. The seeded substrates were then placed in the CVD reactor, allowing for a 15-h diamond deposition with the hydrogen flow rate of 200 sccm and methane of 0.70 sccm. The Pt/diamond composite electrodes were then fabricated following the same procedure described in Chapter 5 with the Pt deposition time ranging from 100 to 500 s.

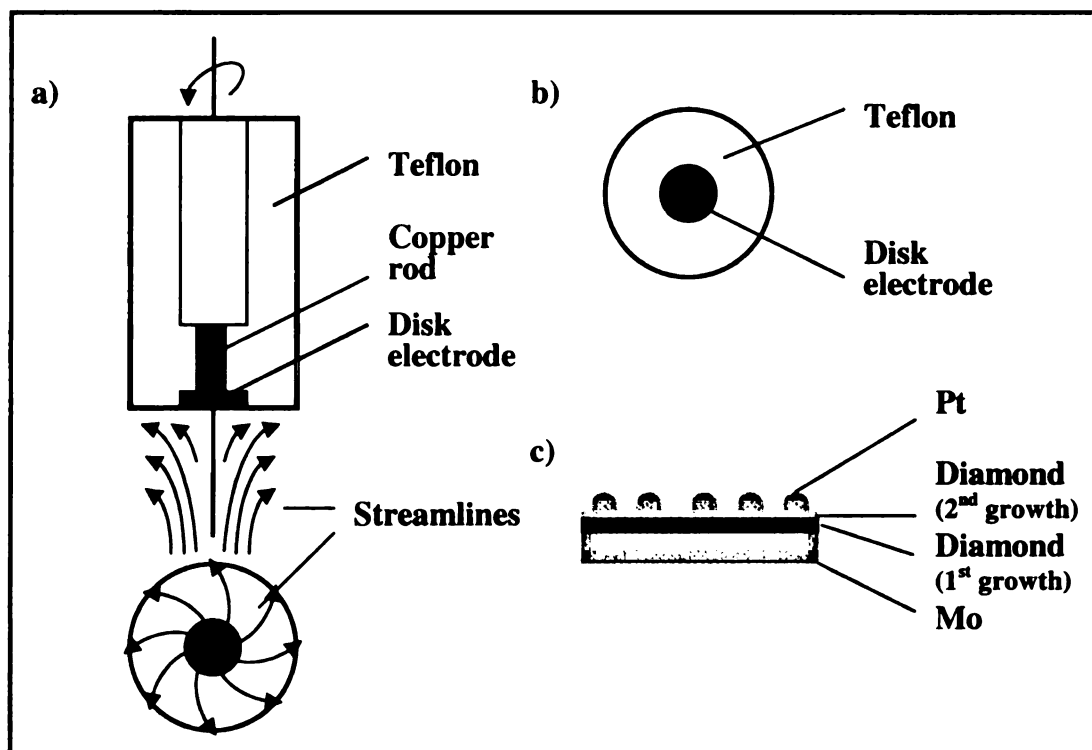


Figure 5.1. Schematic diagram of a rotating disk Pt/diamond composite electrode: a) a top and side view showing the direction of mass transport; b) a view of the electrode mounted in Teflon; c) a side view of the composite disk electrode architecture.

The schematic diagram of a rotating disk Pt/diamond composite electrode is shown in Figure 5.1. The electrode was mounted into the disk position of an insulating

mantle. The geometric area of the electrode is 0.196 cm^2 . A piece of copper rod was soldered to the backside of the Mo disk substrate in order to reduce the contact resistance. The RDE was controlled by a Metrohm 628-10 RDE controller (Metrohm, Switzerland) with a rotation rate from 500 to 3000 rpm.

Instruments and chemicals. All the electrochemical measurements were performed in conventional three-compartment electrochemical cell with a CHI 650A digital potentiostat (CH Instruments, Austin, TX). A Ag/AgCl electrode served as reference electrode. In order to avoid the contamination of the electrolyte, a glass junction containing the electrolyte was used to connect the reference electrode to the cell. For the ORR experiments, the solution was saturated with oxygen gas (99.9%, BOC Gases) by bubbling for 30 min. prior to any electrochemical measurement. All solutions were prepared with ultrapure water from a Barnstead E-Pure purification system ($>17 \text{ M}\Omega\text{-cm}$). The HClO_4 , H_2SO_4 , and H_3PO_4 were ultrahigh purity grade (99.999% Aldrich). All glassware was cleaned in a KOH/methanol bath prior to use.

5.4 Results and Discussion

5.4.1 Characterization of the Diamond Film on Mo Disk

Prior to performing the Pt electrodeposition, structural and electrochemical characterization of the diamond films was conducted. An important consideration is the uniformity of the diamond coating as pinholes and small crevices can provide pathways for solution to permeate through the film and reach the underlying substrate. In such cases, electroactive substrates will directly participate in the electrochemical reactions, and the potential-dependent current will be enhanced.

Figure 5.2 shows a typical SEM image of the polycrystalline diamond film deposited on Mo disk substrate. The image reveals a well-faceted film composed of octahedral, cubic, and cubo-octahedral microcrystallites, grain boundaries, some secondary growths (i.e., smaller growth features on top of the large facets and grain boundaries), and growth hillocks. The grain size is in the range of several hundreds of nanometers to 2 μm . The grains are heavily twinned. The diamond (111) orientation is dominant in this film, as inferred from the x-ray diffraction measurement. The diamond film is continuous over the substrate with no pinholes and crevices observed. Diamond growth on the molybdenum substrate is preceded by the formation of an intermediate layer of MoC which is electrically conductive. The conducting interlayer ensures good electrical and mechanical connection between the Mo substrate and the diamond coating.

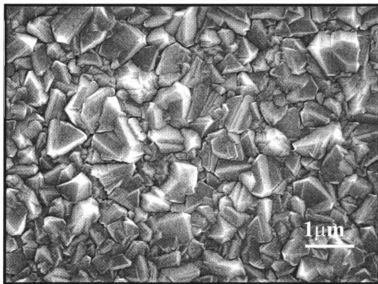


Figure 5.2. SEM image of a boron-doped diamond thin film deposited on a Mo disk. The diamond deposition time was 15 h and methane-to-hydrogen ratio was 0.35%.

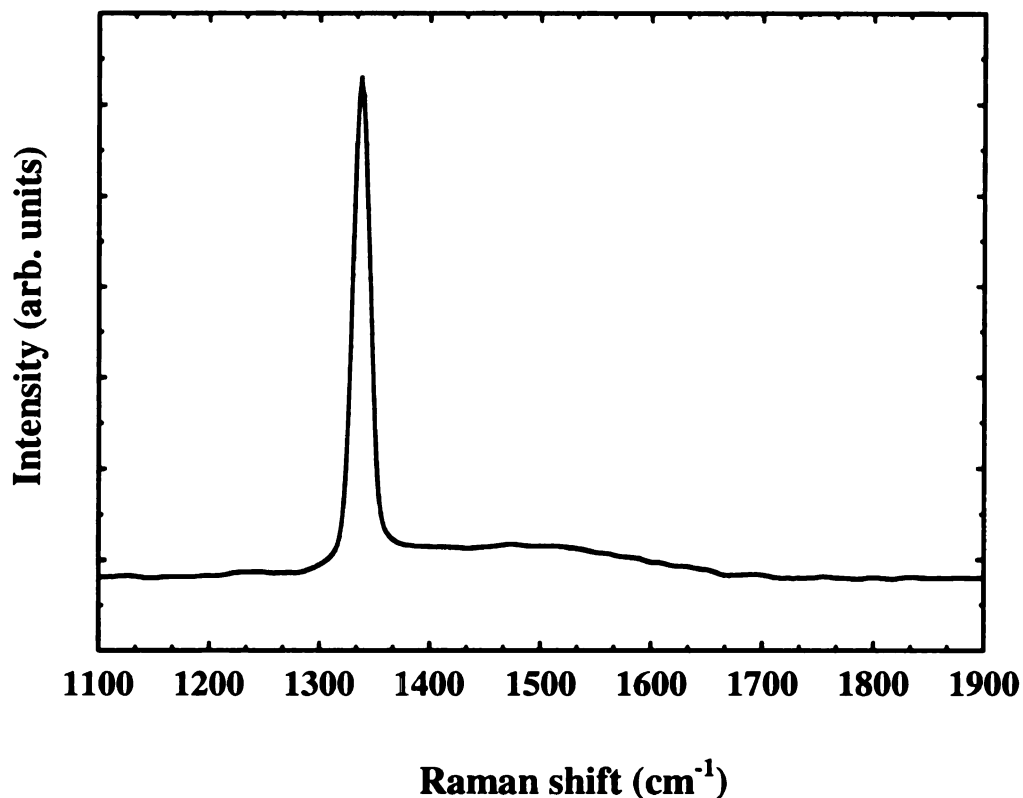


Figure 5.3. Raman spectrum for a boron-doped diamond thin film deposited on a Mo disk. Excitation wavelength = 532 nm. Incident power density = 500 kWcm^{-2} . Integration time = 10 s.

A characteristic Raman spectrum for the diamond film is presented in Figure 5.3. The first-order diamond phonon line is observed at 1337.2 cm^{-1} and has a full width at half maximum (FWHM) of 10.1 cm^{-1} . The peak position is shifted some 5 cm^{-1} toward higher wave numbers, indicating the presence of compressive stress within the film. Compressive stress is expected because of the difference of the thermal expansion coefficient for the film and substrate. The FWHM is much larger than the value of $2\text{-}3 \text{ cm}^{-1}$ that is routinely observed for single crystal diamond. The increased width partially results from stress heterogeneities and stress induced splitting of the triplet zero phonon

line into a singlet and a doublet.¹¹ The FWHM is also a measure of the crystalline perfection, and to a first approximation, is inversely related to the phonon lifetime (i.e., defect density). Another main feature in the spectrum is the broad band in the range of the 1450-1650 cm^{-1} that is assigned to the nondiamond carbon impurity in the film. However, the level of this impurity is very low considering that the peak intensity is weak and the scattering cross-section for graphite (a model for the nondiamond carbon impurity) is ca. 50 times larger than that for diamond.

Electrochemical methods of analysis are quite sensitive probes of the physicochemical properties of diamond electrode. Cyclic voltammetry can be used to ascertain information about the diamond film quality, as the background current and the working potential window are highly sensitive to the presence of the electroactive substrate material, as well as the nondiamond carbon impurity. Figure 5.4 shows a typical cyclic voltammetric *i*-*E* curve for a diamond film deposited on a Mo disk in 0.1 M HClO_4 . The *i*-*E* curve is flat and featureless over a wide potential range (3.4 V at $\pm 50 \mu\text{A}$). The scans are stable with multiple sweeps and no background features associated with Mo are evident, indicating that there is no penetration of the electrolyte solution through the grain boundaries or defects to the reactive substrate. In other words, the molybdenum substrate is completely coated with the diamond film. However, the background current for diamond films deposited on Mo is 3 μA at 250 mV, slightly larger than the current for the films deposited on Si. The slightly larger current is most likely due to some nondiamond carbon impurities at the grain boundaries and defect sites, consonant with the observations obtained in the Raman spectrum.

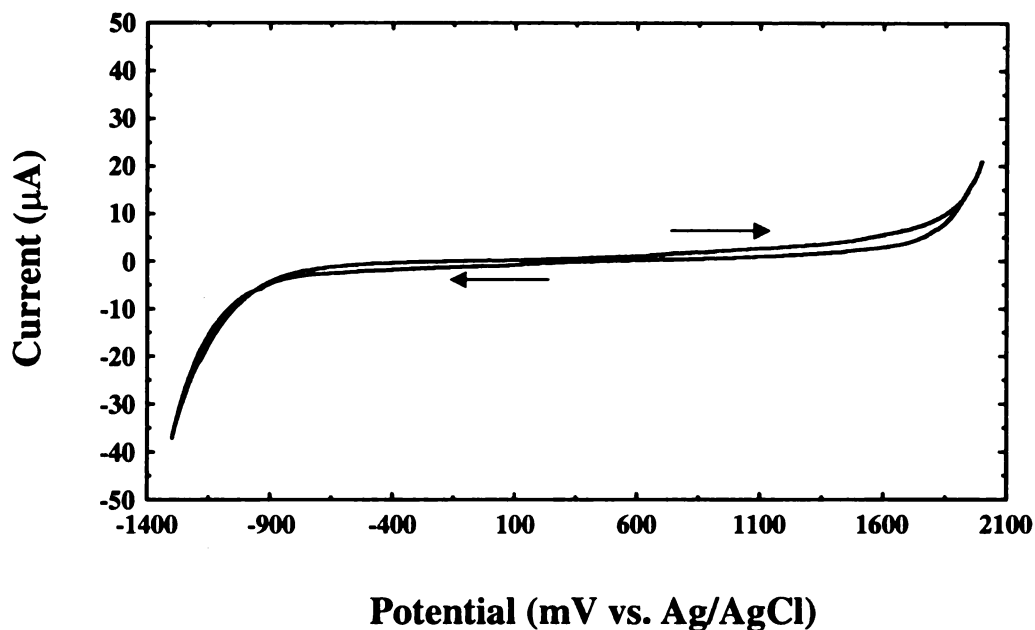


Figure 5.4. Cyclic voltammetric i-E curves for a boron-doped diamond thin film deposited on a Mo disk in 0.1 M HClO₄. Scan rate = 100 mV/s.

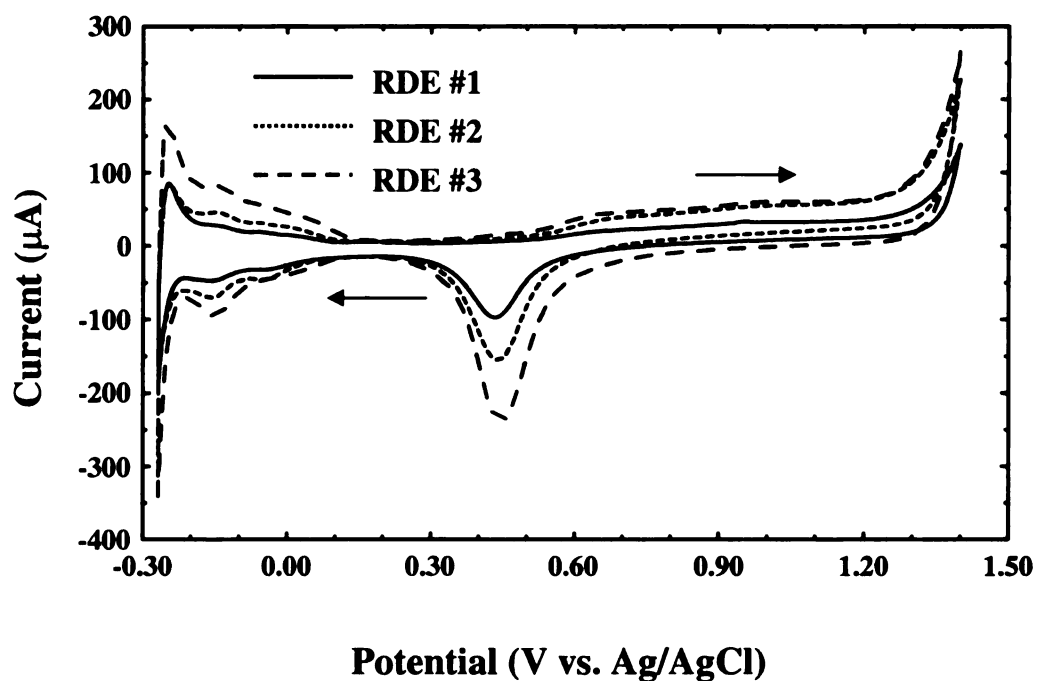


Figure 5.5. Cyclic voltammetric i-E curves for Pt/diamond composite electrodes in 0.1 M HClO₄. The Pt deposition times were 200, 300, and 400 s, respectively. Scan rate = 50 mV/s.

Table 5.1. Electrochemically active surface area and roughness factor for the Pt/diamond composite RDEs with different Pt loadings.

Electrode	Pt deposition time (s)	Maximum Pt loading ^a ($\mu\text{g}/\text{cm}^2$) ^b	Hydrogen adsorption/desorption charge (mC/cm^2) ^b	Roughness factor	Active surface area (cm^2)
RDE #1	200	50.3	0.50	2.4	0.48
RDE #2	300	75.8	0.71	3.4	0.68
RDE #3	400	101.1	0.84	4.0	0.80

- a. Assuming 100% current efficiency for the 4-electron transfer reaction ($\text{Pt}^{4+} \rightarrow \text{Pt}$).
- b. Referred to the geometric surface area of the electrode (0.196 cm^2).

Based on these observations, it can be concluded that the diamond film is continuous over the surface, and the morphology and microstructure are stable such that solvent/electrolyte does not permeate the film and attack the electroactive substrate. The Pt/diamond composite rotating disk electrodes were next fabricated. Figure 5.5 presents the cyclic voltammetric *i*-E curves for three Pt/diamond composite RDEs with varying Pt loadings. The curves were recorded after 100 cycles in 0.1 M HClO₄ at a scan rate of 50 mV/s. Potential cycling between the hydrogen and oxygen evolution region (-0.3 V to 1.5 V) is an efficient way to clean the Pt surface of residual amorphous carbon and other impurities deposited during the secondary diamond growth. The characteristic electrochemical features of clean platinum (poly) gradually develop with potential cycling. As expected, the charge for the hydrogen adsorption/desorption (between -0.25

V and 0.1 V), Pt oxide formation (at ca. 0.65 V) and Pt oxide reduction (at ca. 0.45 V) all increase with increasing Pt loading. The double layer charging current observed between 0.1 and 0.25 V also increases due to the increase in Pt surface area as the loading increases. The hydrogen adsorption/desorption charge was used to estimate the active Pt surface area and the surface roughness factor. The results are presented in Table 5.1.

5.4.2 ORR at Stationary Pt/Diamond Composite Electrodes

Measurement of the open circuit potential. The open circuit potential (OCP) is often used as an indicator of the electrocatalytic activity of an electrode. After the extended potential cycling, the open circuit potential was measured in oxygen-saturated 0.1 M acid solutions at room temperature. An immediate decay of the OCP was observed in all the solutions before the potential reached a steady-state value. Steady-state OCPs in the different acid solutions, for the electrodes varying in Pt loading, are presented in Table 5.2. The OCP is, on average, ca. 0.74 V vs. Ag/AgCl (0.94 V vs. SHE) for all the electrodes in 0.1 M HClO₄, similar to values reported for polycrystalline Pt and Pt coated with Nafion[®].¹² The equilibrium potential is 0.972 V vs. Ag/AgCl for the four-electron transfer ORR in acid solution (pH = 1) at room temperature.⁵ Therefore, the Pt/diamond composite electrodes attain an overpotential loss of ca. 0.23 V in 0.1 M HClO₄, corresponding to a 24% efficiency loss. The overpotential losses have been attributed mainly to the mixed potential that is established at the electrodes.⁶ The mixed potential is due to the cathodic process, i.e., slow oxygen reduction and the competing anodic process, such as the platinum oxide formation and/or impurity oxidation.⁶

Results in Table 5.2 also indicate that the OCPs are independent of the Pt loading in a particular acid solution. However, the OCP values do depend on the electrolyte type. The nominal OCP is ca. 10 mV more negative in 0.1M H₂SO₄ and ca. 25 mV more negative in 0.1 M H₃PO₄. The negative shift is attributed to the anion adsorption effect.¹³ The specific adsorption of these anions increases in the order H₂PO₄⁻ > SO₄²⁻ (or HSO₄)⁻ > ClO₄⁻. The specific adsorption of anions blocks the active sites needed for the chemisorption of oxygen, resulting in more sluggish electrode kinetics.

Table 5.2. Open circuit potentials (25 °C) for the Pt/diamond composite RDEs in different acid electrolytes.

Electrode	0.1 M HClO ₄	0.1 M H ₂ SO ₄	0.1 M H ₃ PO ₄
RDE#1	0.742	0.727	0.720
RDE#2	0.748	0.735	0.721
RDE#3	0.744	0.738	0.718

Note: Values are V vs. Ag/AgCl.

Voltammetric studies of ORR. The ORR at Pt/diamond composite RDEs was initially studied by cyclic voltammetry in quiescent solution. Figure 5.6A (solid line) shows a typical cyclic voltammetric i-E curve for ORR on a Pt/diamond composite electrode. For comparison, the voltammetric response for a polycrystalline Pt foil electrode is shown in Figure 5.6B. The experiments were carried out in O₂-saturated 0.1 M HClO₄ at room temperature. The potential sweep initiated at 1.2 V, whereupon the Pt surface is covered with a thin oxide film, scanned to -0.25 V, and then scanned back to

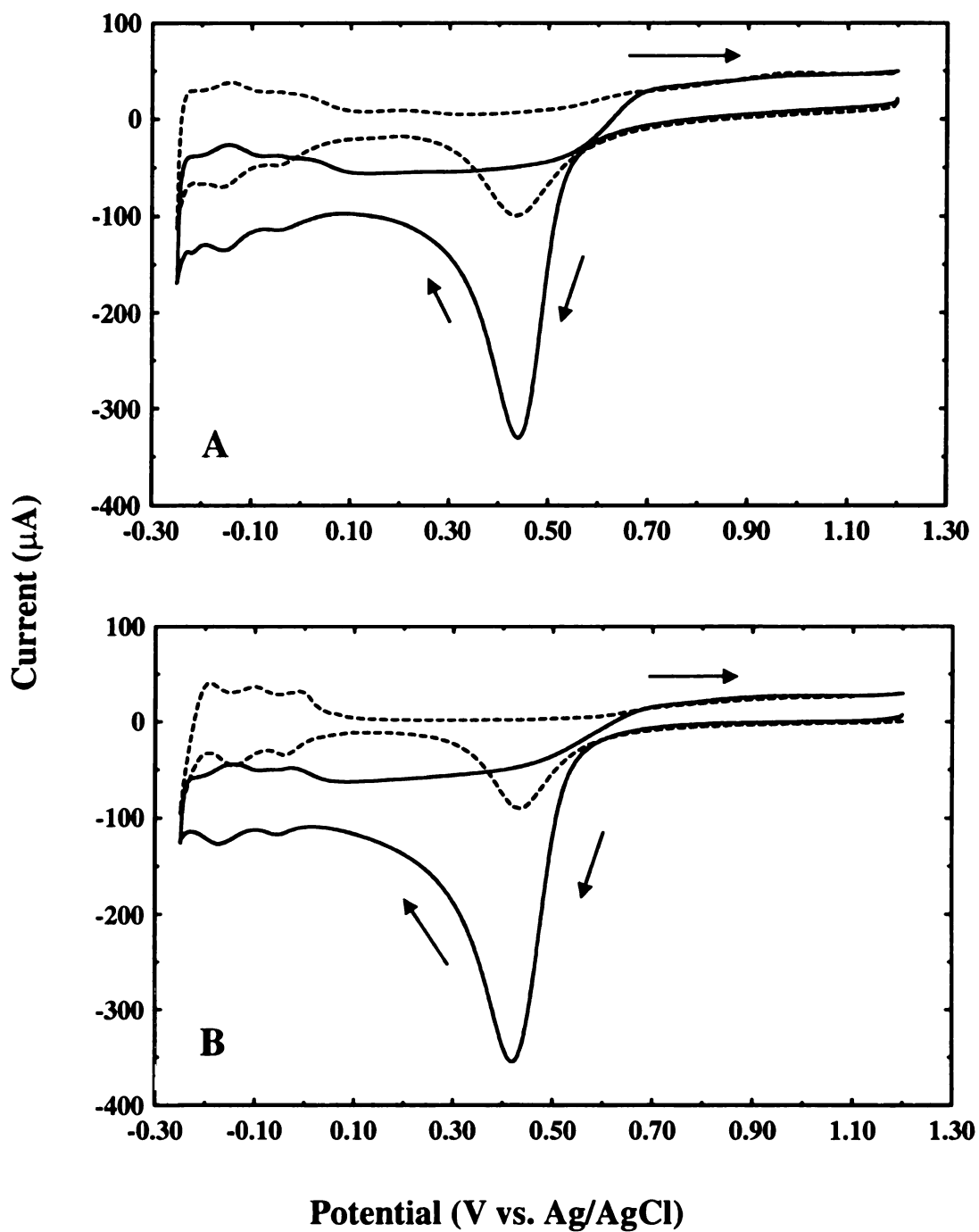


Figure 5.6. Cyclic voltammetric *i*-E curves for (A) RDE #1 and (B) polycrystalline Pt foil electrode in N₂-purged (dashed line) and O₂-saturated (solid line) 0.1 M HClO₄. Scan rate 50 mV/s. Active surface area of the Pt foil electrode is 0.43 cm² (geometric area is 0.2 cm²).

1.2 V. The response for the Pt/diamond composite electrode resembles that for the clean Pt foil. During the cathodic scan direction, discernible reduction current commences at ca. 0.72 V, close to the open circuit potential in this electrolyte. A dramatic increase in the cathodic current is observed at potentials below 0.55 V, accompanied with the reductive removal of the Pt oxide, in agreement with the fast ORR kinetics on oxide-free Pt surface. The current reaches a maximum of 0.33 mA at ca. 0.45 V, and decays rapidly on the low potential side of the peak due to the depletion of oxygen at the electrode surface (diffusion controlled). Evidently, oxygen reduction continuously contributes to the total current, even during the reverse scan, until the Pt oxides begin to form on the electrode surface.

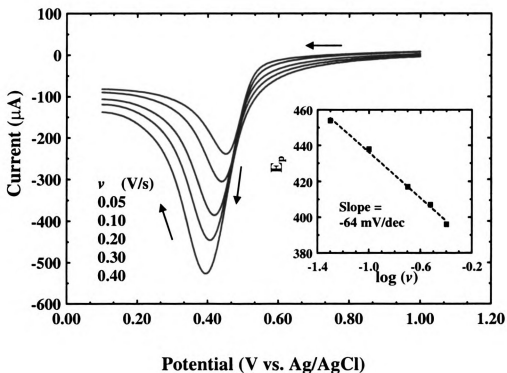


Figure 5.7. Linear potential sweep voltammetric i - E curves for RDE #1 in O_2 -saturated 0.1 M HClO_4 at different scan rates. Inset shows the plot of peak potential vs. logarithm of scan rate.

The rate of ORR on oxide-free Pt surface is limited by the mass transport of dissolved oxygen to the electrode surface. The dependence of the oxygen reduction on the scan rate, ν , was examined. Figure 5.7 shows the linear potential sweep voltammetric i - E curves for a Pt/diamond composite electrode in O_2 -saturated 0.1 M $HClO_4$. The peak current, i_p , increases linearly with $\nu^{1/2}$ when the scan rate changes from 50 to 400 mV/s, indicative of a semi-infinite linear diffusion controlled process. However, i_p rather approaches a proportionality with ν at scan rates higher than 400 mV/s. This is expected as the reaction shifts from being mass transport limited to control by the surface adsorption process.⁵

Along with the increase in peak current, the peak potential, E_p , shifts positively with a scan rate increase. The relationship between the peak potential and the scan rate for an irreversible reaction is¹⁴

$$E_p = E_{1/2} + \frac{b}{2} \left[1.04 - \log \frac{b}{D} - 2 \log k_f + \log \nu \right] \quad (5.5)$$

in which $E_{1/2}$ is the half-wave potential, b is the Tafel slope, D is the diffusion coefficient, and k_f is the rate constant. Therefore, the Tafel slope can be determined by plotting the peak potential vs. the logarithm of scan rate, which is shown as the inset in Figure 5.7. The estimated Tafel slope is -128 mV/dec, close to the value of -120 mV/dec that is expected for ORR on oxide-free Pt surface under Langmuirian conditions.¹⁵ It is also in agreement with the results obtained from the RDE studies describe below.

5.4.3 ORR at Pt/Diamond Composite RDEs

Polarization curves for ORR. The ORR at Pt/diamond composite RDEs was initially studied by cyclic voltammetry. Figure 5.8 shows the cyclic voltammetric *i*-*E* curve for a composite electrode (RDE #3). The response was recorded in O₂-saturated 0.1 M HClO₄ using a rotating rate of 1000 rpm. For comparison, the voltammetric response in N₂-purged electrolyte is also shown. Prior to each measurement, the electrode potential was held at 1.2 V for 2 min., allowing for the formation of well-defined Pt oxide film. The potential scan was then initiated at this potential and scanned in the negative direction. Similar to the voltammetric response in quiescent solution, drastic increase in cathodic current was not observed until the reductive removal of the Pt oxide at a

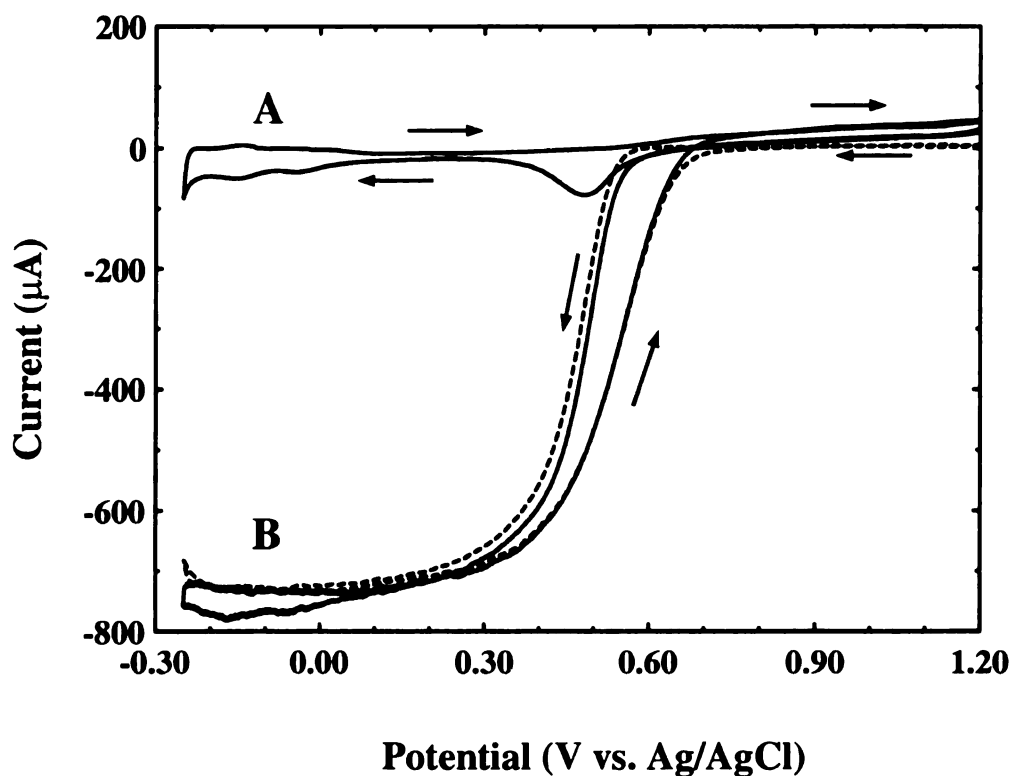


Figure 5.8. Cyclic voltammetric *i*-*E* curves for RDE #3 in (A) N₂-purged and (B) O₂-saturated 0.1 M HClO₄. The dashed line is the curve for oxygen reduction after background correction. Scan rate = 20 mV/s. Rotation rate = 1000 rpm.

potential of ca. 0.55 V. The oxygen reduction is then under combined kinetic and diffusion control at potentials between 0.30 and 0.55 V. As the electrode potential approaches the potential region where clean Pt is formed, a limiting current of ca. 0.7 mA is observed, indicating the ORR is controlled by mass transport.

A notable feature in the *i*-*E* curve is that the ORR kinetics are different depending on potential sweep direction. The onset potential for ORR is more negative by about 0.1 V during the forward sweep than during reverse sweep. This hysteresis is also a characteristic feature of single crystal Pt,¹⁶ Pt supported on high-surface-area carbon,¹⁷ and a Pt electrode coated with Nafion[®].¹⁸ The *i*-*E* curve recorded in the negative sweep reflects the onset of ORR on a partially oxidized Pt surface while during the reverse sweep the ORR occurs on a surface that is essentially oxide-free. Recent studies have suggested that the Pt oxides impede the ORR in two ways: oxides block the active Pt sites and thus hinder the chemisorption of oxygen, and/or increase the adsorption energy of the reaction intermediates which are formed during the ORR on bare Pt sites.¹⁰

The current magnitude of the background *i*-*E* curve does not change with rotation rate because the hydrogen adsorption/desorption, Pt oxidation/reduction are all surface-controlled reactions. The well defined shape of the voltammogram also indicates that the electrolyte is pure, without mass-transfer controlled impurity adsorption process taking place. The hydrogen adsorption is not significantly affected by the presence of dissolved oxygen. Rather, the adsorbed hydrogen suppresses the ORR, and even alters the reaction pathway.¹⁶ Since the current recorded in O₂-saturated electrolyte is a sum of the oxygen reduction current, the current due to Pt oxide formation and reduction, and double-layer

charging current, the i - E curve has been corrected for the background current, which is shown as the dashed curve in Figure 5.8.

A series of background-corrected linear sweep voltammetric i - E curves recorded at different rotation rates is shown in Figure 5.9. All the curves were recorded during the cathodic potential sweep direction. Well-defined, limiting current plateaus are seen, particularly at low rotation rates. At high rotation rates, the potential region for combined kinetic-diffusion control is markedly extended. For a first-order reaction mechanism, the limiting current is proportional to the concentration of dissolved oxygen and the square root of the rotation rate, as predicted by the Levich equation⁵

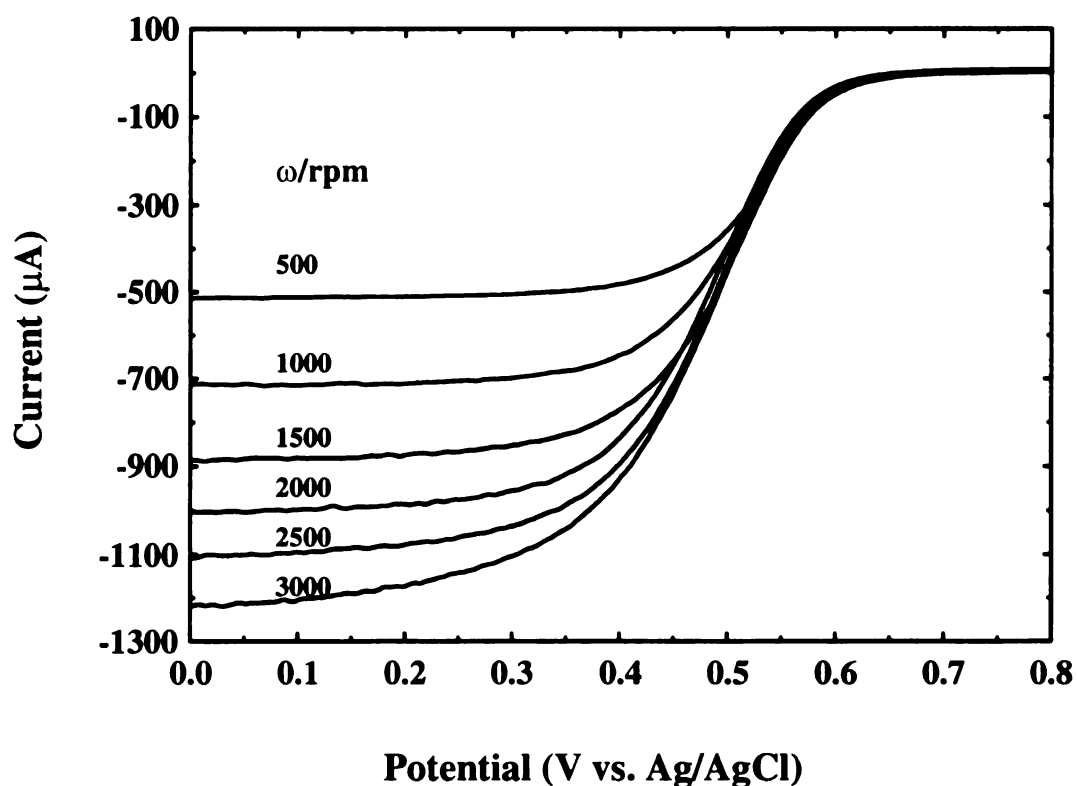


Figure 5.9. Linear sweep voltammetric i - E curves for RDE#3 in O_2 -saturated 0.1 M $HClO_4$ as a function of the rotation rate. Scan rate = 20 mV/s.

$$i_L = 0.62nFAD^{2/3}\nu^{-1/6}\omega^{1/2}C \quad (5.6)$$

or in short form

$$i_L = B\omega^{1/2} \quad (5.7)$$

where n is the number of electrons transferred per O_2 molecule, F is the Faraday's constant, A the electrode surface area, C the concentration of dissolved O_2 in solution, D the diffusion coefficient of dissolved O_2 , ν the viscosity of the solution, and ω the rotation rate of the RDE. B is the so-called Levich slope. If the rotation rate is given in revolutions per minute and C in moles per liter, B , given in $\text{mA} \cdot \text{rpm}^{-1/2}$, can be expressed as

$$B = 0.20nFAD^{2/3}\nu^{-1/6}C \quad (5.8)$$

For this study, the theoretical B value can be calculated for $n = 4$, $A = 0.2 \text{ cm}^2$, using the literature data¹⁹ for $\nu = 0.0087 \text{ cm}^2 \cdot \text{s}^{-1}$, and $CD^{2/3} = 7.6 \times 10^{-10} \text{ mol} \cdot \text{cm}^{-5/3} \cdot \text{s}^{-2/3}$, yielding a value of $2.5 \times 10^{-2} \text{ mA} \cdot \text{rpm}^{-1/2}$.

As mentioned above, the ORR is under mixed kinetic-diffusion control over a wide potential range. Extracting the kinetically-controlled current at different potentials can be made using the Koutecky-Levich equation⁵,

$$\frac{1}{i} = \frac{1}{i_{kin}} + \frac{1}{i_L} \quad \text{or} \quad \frac{1}{i} = \frac{1}{i_{kin}} + \frac{1}{B\omega^{1/2}} \quad (5.9)$$

where i is the total current, i_L is the limiting current, and i_{kin} represents the current in the absence of any mass transfer effects, which gives the order of absolute kinetic activity of the surface. Plotting i^{-1} vs. $\omega^{-1/2}$ yields a y-axis intercept equal to i_{kin}^{-1} and slope equal to B^{-1} .

Koutecky-Levich plots for ORR on a Pt/diamond composite RDE in 0.1 M HClO₄ are presented in Figure 5.10. These plots were constructed from the current values at 0.46, 0.40, 0.30, and 0 V in the polarization curves shown in Figure 5.9. All the plots are straight lines with the same slope. Similar results were also obtained for other electrodes and acid electrolytes. The y-intercept is 0.54 mA⁻¹ for 0.46 V, 0.21 for 0.40 V, 0.07 for 0.30 V and 0.02 for 0 V, respectively. The corresponding slopes are 40.3 mA⁻¹·rpm^{1/2}, 40.8, 41.1 and 41.2, respectively. The B values, 2.43 - 2.48 × 10⁻² mA·rpm^{-1/2}, are in agreement with the theoretical value (2.5 × 10⁻² mA·rpm^{-1/2}), suggesting that the ORR on the Pt/diamond composite electrode involves a 4-electron reduction pathway.

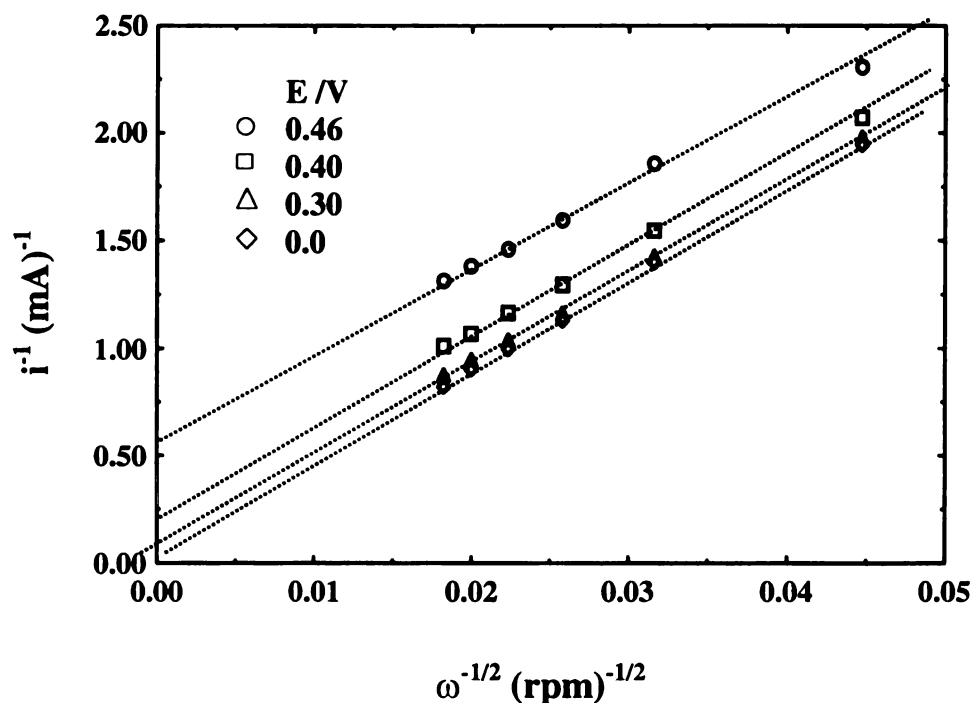


Figure 5.10. Koutecky-Levich plots for the oxygen reduction reaction in 0.1 M HClO₄. Data taken from the polarization curves shown in Figure 5.9.

Tafel plots. The kinetic parameters, the exchange current densities and Tafel slopes, were obtained from mass-transfer-corrected Tafel plots ($\log i$ vs. η). The overpotential for the oxygen reduction, η , was determined by subtracting the equilibrium potential, E_{eq} , from the applied potential, E_{app} . The kinetically-controlled currents can be calculated using Equation 5.9, $i_{kin} = i_L i / (i_L - i)$. The current densities are normalized to the real electrochemically active surface area of the composite electrode (0.80 cm^2 , as estimated from the roughness factor and geometric area),

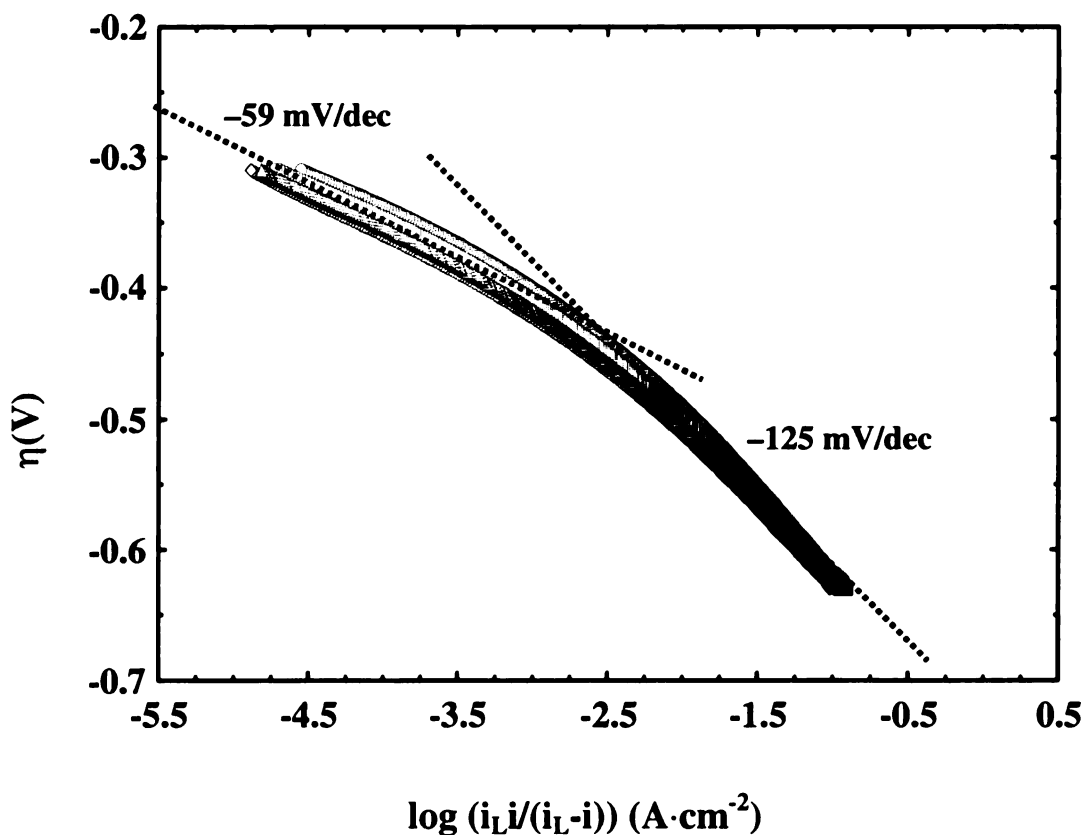


Figure 5.11. Tafel plots for the oxygen reduction reaction in 0.1 M HClO_4 . Data taken from the polarization curves shown in Figure 5.9.

Figure 5.11 shows the set of Tafel plots constructed from the polarization curves presented in Figure 5.9. The plots for different rotation rates overlap and two distinct

Tafel slopes are observed. The break in the Tafel plot, which occurs at an overpotential between -0.45 and -0.50 V, has been previously reported and interpreted as a change in the oxygen chemisorption mechanism.^{20,21} At low overpotentials, the Pt surface is completely or partially covered with oxide film. A low Tafel slope of -60 mV/dec ($-2.3RT/F$) is accounted for by assuming oxygen chemisorption under Temkin conditions in the potential range of oxide formation. At high overpotentials, the coverage of adsorbed oxygen-containing species becomes negligible, and a high Tafel slope of -120 mV/dec ($-2 \times 2.3RT/F$) corresponds to a potential regime where oxygen reduction is under Langmuirian conditions. The kinetic data from each region were independently analyzed and the exchange current density corresponding to each Tafel slope was calculated by extrapolating the potential to $\eta = 0$, i.e. the equilibrium potential. As illustrated in Table 5.3, a Tafel slope of -59 mV/dec at low overpotentials and -125 mV/dec at high overpotentials is seen for ORR in 0.1 M HClO₄. The exchange current densities, i_0 , are 1.9×10^{-10} and 3.1×10^{-7} A·cm⁻², respectively.

Effect of anion adsorption. There are several ways in which the electrolyte can influence the ORR pathway and kinetics. These include changes in the concentration and activity coefficients of the reactants and intermediates, the transition states, solution pH, and the anion adsorption.⁴ A well-known phenomenon for smooth Pt surfaces is the specific adsorption of anions, such as sulfate/bisulfate and phosphate/biphosphate, which competes with the oxygen chemisorption and retards the reaction kinetics.²² Moreover, chemisorbed anions can alter the adsorption energy of the reaction intermediates and thus the reaction pathway.^{10,22} The effect of anion adsorption on the ORR at Pt/diamond composite electrode was examined. Polarization curves were also recorded in 0.1 M

H₂SO₄ and H₃PO₄. The corresponding Tafel plots are shown in Figure 5.12, and the kinetics parameters are summarized in Table 5.3. The overpotential for ORR increases, meaning that the electrode reaction kinetics decrease, in the order of HClO₄ < H₂SO₄ < H₃PO₄. At high overpotentials where the Pt surface is void of oxide, Tafel slopes of -132 and -136 mV/dec, and exchange current densities of 18 and 3.6 × 10⁻⁸ A·cm⁻² are observed in H₂SO₄ and H₃PO₄. At low overpotentials, the exchange current densities are a factor of 30-90 lower in these two acids. Clearly, the specific adsorption of sulfate/bisulfate and phosphate/biphosphate anions inhibits the reaction kinetics, but does not affect the reaction pathway for ORR since similar Tafel slopes are observed for these three acids. These results are consistent with reports in the literature.²³

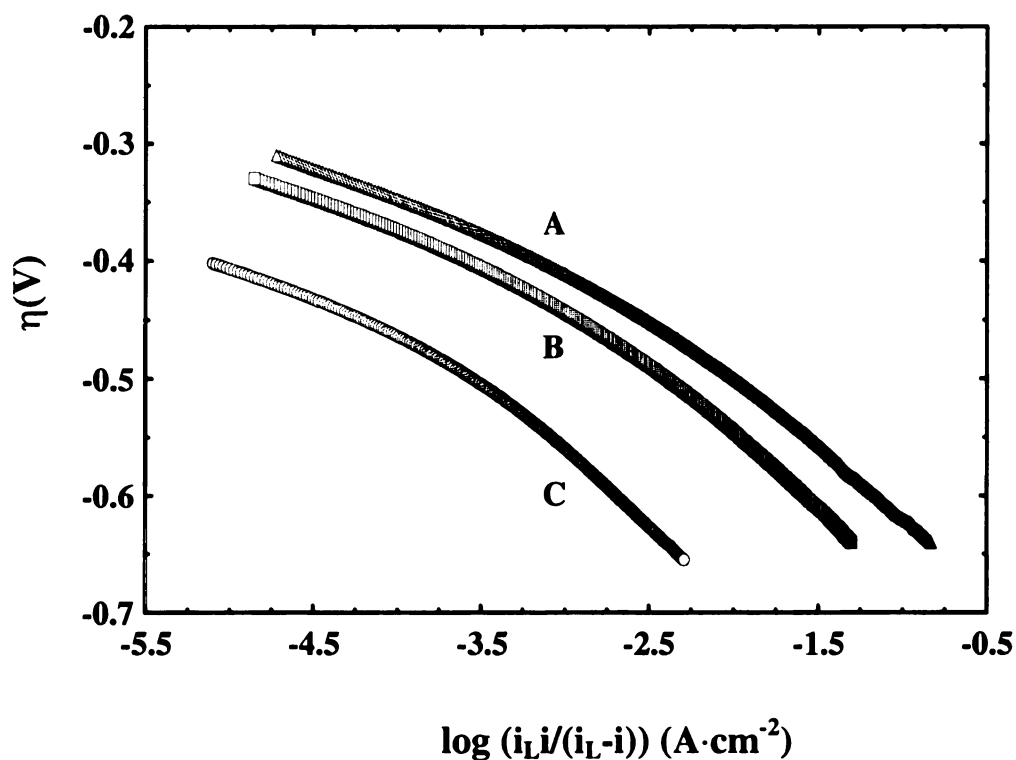


Figure 5.12. Tafel plots for the oxygen reduction reaction at RDE #3 in 0.1 M (A) HClO₄, (B) H₂SO₄ and (C) H₃PO₄. Scan rate = 20 mV/s. Rotation rate = 2500 rpm.

Table 5.3. Comparison of the kinetics parameters for ORR at the Pt/diamond composite electrodes with the literature data reported for single crystal, polycrystalline, and carbon-supported Pt at room temperature.

Electrocatalyst	Electrolyte	Tafel slope (-mV/dec)	i_0 (A·cm ⁻²)	Reference
Pt(111)	1 M H ₂ SO ₄	64.7	2.2×10^{-10}	23
Pt(100)	1 M H ₂ SO ₄	64.5	4.6×10^{-10}	23
Pt(110)	1 M H ₂ SO ₄	64.6	3.4×10^{-10}	23
Pt	0.1 M HClO ₄	60	$\sim 1 \times 10^{-10}$	1
Pt	0.1 M H ₂ SO ₄	70	2×10^{-11}	24
Pt	98% H ₃ PO ₄	99	7.76×10^{-12}	25
Pt	0.05 M H ₂ SO ₄	145	3×10^{-6}	26
Pt/C	1.0 M NaOH	55	1×10^{-8}	27
Pt/C	100% H ₃ PO ₄	90	$(3-7) \times 10^{-8}$	28
Pt/diamond	0.1 M HClO ₄	59	1.9×10^{-10}	This work
		125	3.1×10^{-7}	
Pt/diamond	0.1 M H ₂ SO ₄	62	6.3×10^{-11}	This work
		132	1.8×10^{-7}	
Pt/diamond	0.1 M H ₃ PO ₄	63	2.2×10^{-12}	This work
		136	3.2×10^{-8}	

A comparison of the kinetic parameters for ORR at the Pt/diamond composite electrodes with the literature data reported for single crystal, polycrystalline, and carbon-supported Pt is presented in Table 5.3.^{1,15,24-28} The Tafel slopes and exchange current densities for the Pt/diamond composite electrodes in these acid electrolytes are comparable to those reported for polycrystalline Pt. The results indicate that the Pt

electrocatalyst is not contaminated with the carbon residual from the secondary diamond growth. In addition, the possible contact resistance between the catalyst and the supporting material is negligible. In other words, the diamond matrix exhibits metal-like electrical conductivity as both the support material and the current collector.

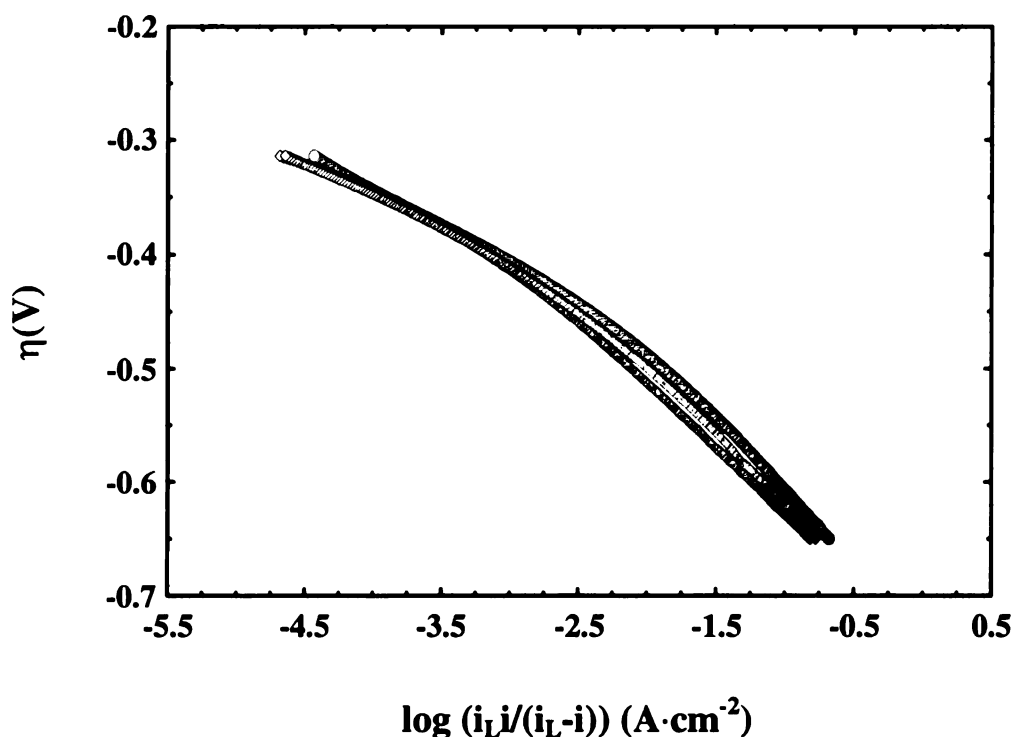


Figure 5.13. Tafel plots for the oxygen reduction reaction in 0.1 M HClO_4 at different Pt/diamond RDEs. Scan rate = 20 mV/s. Rotation rate = 2500 rpm.

Effect of Pt loading. The effect of Pt loading on the ORR at the Pt/diamond composite electrodes was also examined in the three acid electrolytes. Polarization curves for the three composite RDEs (see Table 5.1) were recorded in 0.1 M HClO_4 and the corresponding Tafel plots are shown in Figure 5.13. The kinetically-controlled current densities are normalized to the electrochemically active surface area of the RDEs (0.48,

0.68 and 0.80 cm², respectively). The plots overlap at both low and high overpotentials, meaning that there is no significant influence of Pt loading on the reaction kinetics.

There are two additional parameters that reflect the electrocatalyst activity for the ORR; specific activity (SA) and mass activity (MA). These terms are defined by the following relationships³

$$SA(A/cm^2 Pt) = \frac{\text{current}}{\text{active surface area of Pt}} \quad (5.10)$$

and

$$MA(A/gPt) = \frac{\text{current}}{\text{mass of Pt}} \quad (5.11)$$

The specific activity provides a measure of the electrocatalytic activity of Pt atoms in the particle surface. The mass activity has more practical implications because the cost of the electrode depends on the amount of platinum used. The relationship between the SA and MA can be expressed as

$$MA = SA \times S \quad (5.12)$$

where S is the specific surface area defined as the real surface area of unit mass of Pt (cm²/g).

Therefore, the Tafel plots in Figure 5.12 and 5.13 essentially reflect the dependence of the SA of the Pt/diamond electrocatalyst on the electrolyte type and catalyst loading because all the currents are normalized to the real surface area of Pt. It is a common practice to compare the SA and MA for ORR by measuring the current at 0.9 V vs. SHE (corresponding to an overpotential of ca. -0.33 V), where influences of the mass transport are negligible.^{7,29} The SA and MA of the Pt/diamond composite electrodes in the three acid electrolytes are listed in Table 5.4, along with the literature data reported

for other carbon-supported Pt electrocatalysts.^{7,29-32} Both SA and MA decrease in the order of HClO₄ > H₂SO₄ > H₃PO₄. The SA in 0.1 M HClO₄ is ca. 55 μA/cm², about two orders of magnitude larger than in H₃PO₄.

Table 5.4. Comparison of the specific activity (SA) and mass activity (MA) of the Pt/diamond composite electrode for ORR with the literature data reported for other carbon-supported Pt electrodes.

Electrocatalyst	Temperature (°C)	Electrolyte	SA ^a (μA·cm ⁻²)	MA ^a (A·g ⁻¹)	Reference
Pt/C	70	20% H ₂ SO ₄	0.4-14	0.1-9.1	30
Pt/graphite	25	1 M H ₂ SO ₄	40-70	4-25	29
Pt/Vulcan	50	1 M H ₂ SO ₄	20	—	32
Pt/Vulcan	60	0.5 M HClO ₄	65	—	7
Pt/Vulcan	60	0.5M H ₂ SO ₄	35	—	7
Pt/diamond ^b	25	0.1 M HClO ₄	55	2.2	This work
Pt/diamond	25	0.1 M H ₂ SO ₄	19.3	0.77	This work
Pt/diamond	25	0.1 M H ₃ PO ₄	0.72	0.03	This work

a. Activities measured at 0.9 V vs. SHE (overpotential = - 0.33 V).

b. Composite electrode with a Pt deposition time of 400 s.

As seen in Figure 5.13, the SA of the Pt/diamond composite electrode for ORR is independent on the Pt loading. The value, 55 ± 6 μA·cm⁻², is rather comparable to those reported for carbon-supported Pt. The MA of the electrode slightly decreases from 2.6 to 2.2 A·g⁻¹ while the apparent Pt loading increases from 50.3 to 101.1 g·cm⁻². These results are consistent with those reported in the literature and can be interpreted in terms of

structure sensitivity of the ORR. Recent studies of ORR on low-index Pt single-crystal surfaces indicated that the reaction rate varies with crystallographic orientation. In HClO_4 the specific activity increases in the order $\text{Pt}(100) < \text{Pt}(110) \approx \text{Pt}(111)$. Since small Pt particles are generally treated as an assembly of the low index facets, the ORR on the particles may resemble the behavior of Pt single crystals and the overall activity varies with varying the relative ratio of the low index facets exposed on the particle surface. The XRD measurements reveal that the Pt particles dispersed in the diamond matrix have a predominant fraction of (111) facets. Furthermore, the relative ratio of the three low index facets remains nearly constant while the Pt loading increased from 50.3 to 101.1 $\text{g}\cdot\text{cm}^{-2}$ with Pt particle size ranging from 40 to 500 nm. Therefore, the observed specific activity is expected to be independent on the Pt loading. This is consistent with the studies by Zeliger³³, Bett et al³⁴, Kunz and Gruver³⁵, and Vogel and Baris³⁶, which show that the specific activity of Pt particles larger than 3 nm for oxygen reduction is independent of the particle size and even approximately the same as smooth Pt. However, the MA decreases with Pt loading because the particle size slightly increases, thus the specific surface area decreases, with increased Pt loading.

5.5 Conclusions

Electrochemical measurements of the oxygen reduction kinetics at the Pt/diamond composite electrodes were presented. The results can be summarized as follows:

1. The mechanism of oxygen reduction at the Pt/diamond composite electrode follows that proposed for polycrystalline and carbon-supported Pt catalysts.

Two distinct Tafel slopes were obtained, with the value consistent with $-2.3RT/F$ and $-2 \times 2.3RT/F$, respectively.

2. The exchange current density for the ORR in the fuel cell operative potential region (low overpotential region) is ca. $10^{-10} \text{ A}\cdot\text{cm}^{-2}$ in 0.1 M HClO_4 , two order of magnitude higher than in 0.1 M H_3PO_4 .
3. The specific activity of the composite electrodes is $55 \pm 6 \mu\text{A}\cdot\text{cm}^{-2}$ at 0.9 V vs. SHE in 0.1 M HClO_4 , comparable to those reported for carbon-supported Pt. The effect of the anion adsorption on the specific activity and mass activity are significant. But the specific activity is independent on the Pt loading.
4. The comparable catalytic activity of the composite electrode to the smooth Pt indicates that contamination of the Pt particles by the carbon residues from the secondary diamond growth is negligible. The diamond film exhibits metal-like electrical conductivity as both a support material and current collector.
5. Further work will focus on the optimization of diamond growth conditions and catalyst dispersion procedure in order to reduce the particles size and improve the reactivity of this new type of catalyst.

References:

1. A. Damjanovic and V. Brusic, *Electrochim. Acta*, **12**, 1171 (1967).
2. E. Yeager, *Electrochim. Acta*, **29**, 1527 (1984).
3. K. Kinoshita, *Electrochemical Oxygen Technology*, John Wiley & Sons, Inc., (1992).
4. R. Adzic, in *Electrocatalysis*, J. Lipkowski and P. N. Ross, Editors, Wiley-VCH, New York, 197 (1998).
5. A. J. Bard and L. R. Faulkner, *Electrochemical Methods, Fundamentals and Applications*, John Wiley & Sons, Inc, New York, 2001.
6. A. Parthasarathy, S. Srinivasan, A. J. Appleby, and C. R. Martin, *J. Electroanal. Chem.*, **339**, 101 (1992).
7. U. A. Paulus, T. J. Schmidt, H. A. Gasteiger, and R. J. Behm, *J. Electroanal. Chem.*, **495**, 134 (2001).
8. A. J. Appleby, *Corrosion*, **43**, 398 (1987).
9. V. Stamenkovic, N. M. Markovic, and P. N. Ross, *J. Electroanal. Chem.*, **500**, 44 (2001).
10. N. M. Markovic, H. A. Gasteiger, B. N. Grgur, and P. N. Ross, *J. Electroanal. Chem.*, **467**, 157 (1999).
11. Y. Kaenel, J. Stieger, J. Michler, and E. Blank, *J. Appl. Phys.*, **61**, 1726 (1997).
12. A. Parthasarathy, S. Srinivasan, and A. J. Appleby, *J. Electrochem. Soc.*, **139**, 2530 (1992).
13. P. N. Ross and P. C. Andricacos, *J. Electroanal. Chem.*, **154**, 205 (1983).
14. E. Gileadi, *Electrode Kinetics*, VCH, New York, 173 (1993).
15. A. Damjanovic, M. A. Genshaw, and J. O. M. Bockris, *J. Electrochem. Soc.*, **114**, 466 (1967).
16. N. M. Markovic, H. A. Gasteiger, and P. N. Ross, Jr., *J. Phys. Chem.*, **99**, 3411 (1995).
17. S. L. Gojkovic, S. K. Zecevic, and R. F. Savinell, *J. Electrochem. Soc.*, **145**, 3713 (1998).

18. S. L. Gojkovic, S. K. Zecevic, and R. F. Savinell, *J. Electrochem. Soc.*, **145**, 3713 (1998).
19. N. M. Markovioc, R. R. Adzic, B. D. Cahan, and E. B. Yeager, *J. Electroanal. Chem.*, **377**, 249 (1994).
20. A. Damjanovic and V. Brusic, *Electrochim. Acta*, **12**, 615 (1967).
21. A. Damjanovic and M. A. Genshaw, *Electrochim. Acta*, **12**, 1281 (1970).
22. P. N. Ross and P. C. Andricacos, *J. Electroanal. Chem.*, **154**, 205 (1983).
23. N. Markovic, H. Gasteiger, and P. N. Ross, *J. Electrochem. Soc.*, **144**, 1591 (1997).
24. F. E. Kadiri, R. Faure, and R. Durand, *J. Electroanal. Chem.*, 177 (1991).
25. M. A. Enayetullah, T. D. Devilbiss, and J. O. M. Bockris, *J. Electrochem. Soc.*, **136**, 3369 (1989).
26. P. Fischer and J. Heitbaum, *J. Electroanal. Chem.*, **112**, 231 (1980).
27. J. Perez, A. Tanaka, E. R. Gonzalez, and E. A. Ticianelli, *J. Electrochem. Soc.*, **141**, 431 (1994).
28. H. R. Kunz and G. A. Gruver, *Electrochim. Acta*, **23**, 219 (1978).
29. J. A. Poirier and G. E. Stoner, *J. Electrochem. Soc.*, **141**, 425 (1994).
30. K. F. Blurton, P. Greenburg, H. G. Oswin, and D. R. Rutt, *J. Electrochem. Soc.*, **119**, 559 (1972).
31. J. A. Poirier and G. E. Stoner, *J. Electrochem. Soc.*, **142**, 1127 (1995).
32. J. Bett and J. Lundquist, *Electrochim. Acta*, **18**, 343 (1973).
33. H. Zeligler, *J. Electrochem. Soc.*, **114**, 144 (1967).
34. J. Bett, J. Lundquist, E. Washington, and P. Stonehart, *Electrochim. Acta*, **18**, 343 (1973).
35. H. R. Kunz and G. A. Gruver, *J. Electrochem. Soc.*, **122**, 1279 (1975).
36. W. M. Vogal and J. M. Baris, *Electrochim. Acta*, **22**, 1259 (1977).

Chapter 6

Methanol Oxidation Reaction on Metal/ Diamond Composite Electrodes

6.1 Introduction

During the past three decades, the methanol oxidation reaction (MOR) has been investigated intensively because of its importance as a feedstock in the direct methanol fuel cell (DMFC).¹⁻⁵ There has recently been a resurgence in DMFC R&D in view of its possible use in transportation applications, i.e. electric vehicles.⁶ Methanol is one type of liquid fuel offering several advantages over others with respect to the storage, safe handling and rapid refueling. Its use eliminates the need for a bulky, heavy, and complex fuel processor, which is estimated to have about the same weight and volume as the fuel cell stack. Methanol also has a high energy, gravimetrically and volumetrically. One mL of methanol can deliver about 2.5 Wh of electricity even at 50% efficiency.

There are, however, at least two research challenges that need to be solved in order for the large-scale application of DMFCs to emerge: the sluggish oxidation reaction kinetics at the anode (methanol) and high catalyst cost. Pt-based materials are, to date, the only acceptable catalysts for methanol oxidation. Dissociative chemisorption of methanol can proceed quite rapidly on the platinum surface, particularly at potentials about 0.2 V vs. RHE, forming chemisorbed species such as PtCOH and PtCO. The further conversion of these adsorbates to form the final product, CO₂, requires attack on the carbon by oxygen-containing species that are generated from the dissociative chemisorption of water.⁷ However, this process is rather slow at electrode potentials below ca. 0.4 V vs.

RHE since pure Pt does not efficiently adsorb water over this potential range.⁷ Consequently, the accumulation of CO and other organic residues takes place, which can block the reactive sites and thus plague the overall reaction. In order to overcome the poisoning problem, many efforts have been made to develop binary or ternary catalysts of Pt alloyed with more oxophilic elements, such as Ru^{8,9}, Sn¹⁰, and Mo¹¹, etc. These promoters for methanol oxidation are believed to act primarily either by providing “active” oxygen adducts or by increasing the susceptibility of the carbon-containing intermediates to oxygen-donor attack.

Considering the catalyst cost, noble metals are essentially utilized as nanometer-sized particles dispersed onto a porous supporting material, in order to achieve the highest possible specific surface area (i.e., surface area to mass ratio). The small particle size can also modify the catalytic activity.¹² Some research has been undertaken to examine possible effects of the particle size, but the findings appear to be controversial. Yahikozawa et al. studied Pt deposited on glassy carbon surface by vacuum evaporation and found that the specific activity for methanol electrooxidation increased with increasing Pt particle size from 3.8 to 5.3 nm, approaching the specific activity of smooth Pt.¹³ Kabbabi et al. used Pt supported on Vulcan carbon (E-TEK) with the average Pt particle size from 1.8 to 25 nm. They reported a sharp increase in specific activity with increasing Pt particle size from 1.8 to 6 nm, followed by a nearly constant specific activity up to 25 nm.¹⁴ Gojkovic et al. reported a maximum specific activity for a Pt particle size of 3.5 nm supported on Black Pearls carbon (E-TEK).¹⁵ However, Watanabe et al. observed no particle size effect, even for a particle size as small as 1.4 nm. Therefore, they concluded that increasing the platinum dispersion on carbon is an

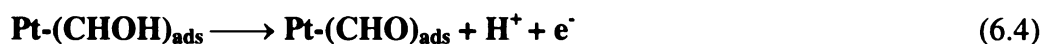
interesting possibility for achieving higher catalytic activity with low amounts of platinum.¹⁶

In Chapter 5, it was shown that the dimensionally stable Pt/diamond composite electrodes exhibit comparable electrocatalytic activity to polycrystalline Pt for the ORR — the cathode reaction in DMFCs. It is of immediate interest to probe the catalytic activity of the composite electrodes toward MOR — the anode reaction in DMFCs. In this chapter, results from studies of MOR at metal/diamond composite electrodes are presented, specifically data from cyclic voltammetric and chronoamperometric measurements. The purpose of the work was to compare the reaction kinetics of Pt supported on diamond with Pt supported on other sp^2 -bonded carbon supports. Efforts to prepare the Pt/Ru/diamond composites were also made. Preliminary results presented below indicate that the electrocatalytic activity for MOR was greatly enhanced by the bimetallic catalyst.

6.2 Mechanism and Kinetics of MOR

Mechanism. Beden et al. proposed a complete and widely accepted mechanism for the electrooxidation of methanol at Pt in acidic media.⁵ The main reaction pathway is the formation of CO_2 via CO as an intermediate, which includes the adsorption of methanol, dehydrogenation of adsorbed methanol, formation of PtCO, and reaction of PtCO with surface bonded hydroxyl radicals, PtOH. The chemical reactions for these steps are written as follows:

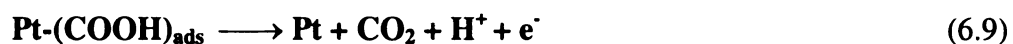
The first step of the electrooxidation reaction is the dissociative chemisorption of methanol, leading to several partially hydrogenated species and CO.



After the Reaction 6.4, the formyl-like species is spontaneously dissociated on platinum according to the reaction:



Oxidation of adsorbed intermediates requires the dissociation of water to form OH species:



Adsorbed CO can be oxidized through the reactions:



This mechanism takes into account the formation of all the products: CO₂, formaldehyde, and formic acid.

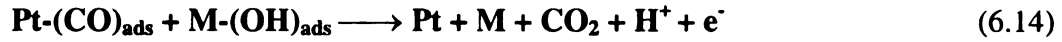
At a bimetallic catalyst, the adsorbed OH_{ads} is formed at lower potentials at the promoter site:



Then, the oxidation reaction can take place



Adsorbed CO can be oxidized at lower potentials through the reactions:



Kinetics. The rate-determining step (rds) of MOR on platinum is the oxidation of adsorbed CO_{ads} with adsorbed hydroxyl species (Reaction 6.10).⁵ The current density for the reaction can be obtained from the following equation

$$i = nFk\Theta_{\text{res}}\Theta_{\text{OH}} \exp\left(\frac{\alpha n_{\text{rds}} FE}{RT}\right) \quad (6.16)$$

where Θ_{res} and Θ_{OH} are the coverages of adsorbed methanol residues and hydroxyl groups, n and n_{rds} are the number of electrons involved in the overall reaction and in the rate-determining step, k is the rate constant, F the Faraday constant, α the transfer coefficient, and E the electrode potential. Clearly, the oxidation rate at constant potential depends on the surface concentration of the adsorbed species, rather than the bulk concentration. As proposed by Bagotzky and Vassilyev, the adsorption of the reaction intermediates is governed by a Temkin-type isotherm:¹⁷

$$\Theta_{\text{res}} = \text{const} + \frac{1}{f} \ln c \quad (6.17)$$

where f is the inhomogeneity factor, and c is the bulk concentration of methanol.

6.3 Experimental

Electrode preparation. The composite electrodes were fabricated via the same stepwise procedure described in Chapter 4, except for the co-deposition of Pt and Ru in the case of the bimetallic catalyst preparation. The co-deposition of Pt and Ru was carried out in N_2 -purged 0.1 M $HClO_4$ containing 1 mM K_2PtCl_6 and $RuCl_3$, with concentrations ranging from 0.2 to 1mM. Deposition was performed galvanostatically at 0.5 mA/cm^2 and the deposition time ranged from 100-700 s. A polycrystalline Pt foil electrode was used for comparison measurements. This Pt surface was pretreated by polishing in successively small alumina/water slurries (particle size 1.0, 0.3, 0.05 μm), and cleaning by ultrasonication in ultrapure water for 5 min after each polishing step. The active surface area and roughness factor for all these electrodes, determined from the hydrogen adsorption/desorption charge, are presented in Table 6.1.

Electrode cleaning procedure. A clean Pt surface is necessary in order to obtain valid and reproducible results for the MOR. Two cleaning procedures were employed according to the type of experiment and solution. In pure electrolyte, a potential cycling procedure was employed. The electrode was subjected to 50 potential cycles between -0.4 and $1.5 \text{ mV vs. Ag/AgCl}$ at a sweep rate of 50 mV/s . The final electrode potential was fixed at $0.2 \text{ V vs. Ag/AgCl}$. In solutions containing methanol, a pulse cleaning procedure was employed for complete oxidative removal of chemisorbed methanol residues. The electrode was subjected to the following potential pulse sequences: 2 s at $-0.3 \text{ V vs. Ag/AgCl}$, 2 s at 1.4 V , 2 s at -0.3 V , 2 s at 1.4 V , and 10 ms at -0.1 V . After each potential step or sweep measurement, in which methanol was oxidized, the pulse sequence given above was reapplied.

Table 6.1. Electrochemically active surface area and roughness factor for the polycrystalline Pt and Pt/diamond composite electrodes with different Pt loadings.

Electrode	Pt deposition time (s)	Hydrogen adsorption/desorption charge (mC/cm ²)	Roughness factor	Active surface area (cm ²)
E1	100	0.25	1.2	0.24
E2	200	0.46	2.2	0.44
E3	300	0.63	3.0	0.60
Pt foil	—	0.40	1.9	0.38

Instruments and chemicals. All the electrochemical measurements were performed with a CHI 650A digital potentiostat (CH Instruments, Austin, TX). All the potentials were recorded vs. a commercial Ag/AgCl reference electrode ($E^0 = 0.197$ V vs. SHE). All solutions were prepared with ultrapure water from a Barnstead E-Pure purification system (>17 M Ω -cm). The HClO₄, H₂SO₄, and H₃PO₄ were ultrahigh purity grade (99.999% Aldrich) and the K₂PtCl₆, RuCl₃ (Aldrich) and CH₃OH (Fisher Scientific) were reagent grade quality. All glassware was cleaned in a KOH/methanol bath prior to use.

6.4 Results and Discussion

6.4.1 Measurement of the Open Circuit Potential

Table 6.2. Open circuit potentials for Pt/diamond composite electrodes in 0.1 M HClO₄ with different methanol concentrations.

Electrode	Methanol Concentration (M)				
	0.2	0.6	1.0	1.5	2.0
E1	0.240	0.221	0.210	0.182	0.169
E2	0.232	0.212	0.200	0.179	0.168
E3	0.230	0.200	0.193	0.178	0.170

Note: Values are in V vs. Ag/AgCl .

Open circuit potential (OCP) measurements are often used as an indicator of the electrocatalytic activity of an electrode. The OCPs for the Pt/diamond composite electrodes with different platinum loadings, were measured in N₂-purged 0.1 M HClO₄ as a function of the CH₃OH concentration. Prior to each measurement, the electrodes were subjected to the potential cycling cleaning procedure, followed by exposure to CH₃OH solution for 10 min. The OCP slowly increased (more positive) during the initial stage of the measurement before reaching a steady state after about 5 min. Steady-state OCP values are presented in Table 6.2. The OCP is, on average, about 0.20 V vs. Ag/AgCl, indicating a ca. 0.4 V positive shift with respect to the equilibrium potential of methanol oxidation (-0.180 V vs. Ag/AgCl).⁶ The gradual positive shift in OCP is presumably due to the dissociative chemisorption of CH₃OH to form CO. The OCP decreases with the increase in the CH₃OH concentration, consistent with the trend predicted by the Nernst equation.

6.4.2 MOR at Pt/Diamond Composite Electrodes

6.4.2.1 Cyclic Voltammetric Studies of MOR

The MOR kinetics were initially studied by cyclic voltammetry. Figure 6.1A (solid line) presents a typical cyclic voltammetric i - E curve for MOR at a Pt/diamond composite electrode. For comparison, the voltammetric response for a polycrystalline Pt foil electrode is shown in Figure 6.1B. The experiments were carried out at room temperature in N_2 -purged 0.1 M $HClO_4$ containing 0.2 M CH_3OH . The potential sweep was initiated at 0 mV and scanned in the positive direction at a scan rate of 50 mV/s. The background i - E curves for both electrodes are shown as dashed lines.

The response for the Pt/diamond composite electrode resembles that for the clean Pt foil. The voltammogram displays peaks that are also characteristic of MOR on supported Pt catalysts in acidic solution.¹⁵ During the forward or anodic sweep, discernible faradaic current begins at ca. 0.25 V, corresponding to the dehydrogenation reactions (Reaction 6.1-4). The current is low due to surface poisoning by the rapid formation of chemisorbed organic residues, mainly CO. As the applied potential becomes more positive, dissociative chemisorption of water takes place (Reaction 6.6). Accordingly, there is a sharp rise in the current at $E > 0.4$ V, which is attributed to the oxidative removal of the adsorbed organic residues (Reaction 6.7-10). An oxidation peak is observed at 0.65 V with a peak current, i_{pl}^{ox} , of 420 μA . The oxidation charge is greater than that predicted for the oxidation of a monolayer of adsorbed CO, so in addition to the oxidation of adsorbed CO, oxidation of additional CH_3OH molecules is occurring.

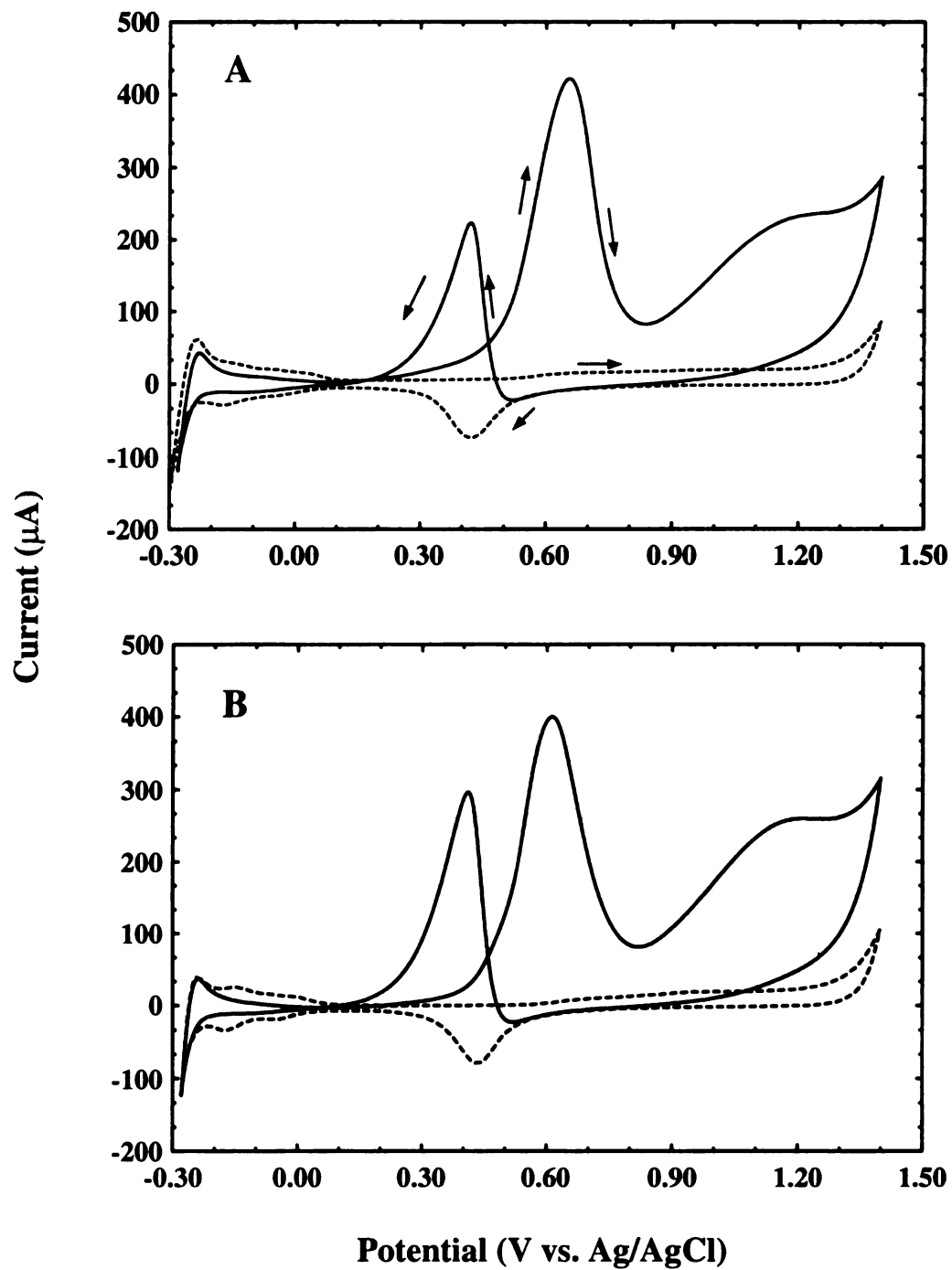


Figure 6.1. Cyclic voltammetric i-E curves for (A) Pt/diamond composite electrode and (B) polycrystalline Pt foil electrode in 0.1 M HClO₄ + 0.2 M CH₃OH (solid line) and 0.1 M HClO₄ (dashed line). Scan rate = 50 mV/s. Active surface area of the composite electrode is 0.44 cm² (Pt deposition time was 200 s).

The decline in current above 0.65 V reflects the inhibition of the MOR by surface oxide formation at these potentials. However, some catalytically active surface oxides are formed again at potentials greater than 0.85 V, accounting for the second anodic peak near 1.2 V (Reaction 6.10). The oxygen evolution reaction takes place at potentials greater than 1.3 V. The surface is inactive toward CH₃OH oxidation on the reverse sweep until the reduction of the surface oxides at 0.55 V (i.e., formation of bare Pt). An oxidation peak is then observed at ca. 0.42 V with a peak current, i_{p2}^{ox} , of 225 μ A. At potentials below 0.2 V, the active surface sites become blocked by CO formation from the dehydrogenation of chemisorbed CH₃OH. Consequently, hydrogen adsorption/desorption is significantly suppressed.

The specific activity (SA) was determined by normalizing the current to the electrochemically active surface area. At 0.6 V vs. Ag/AgCl, the specific activity for the composite electrode (0.75 mA·cm⁻²) is smaller than that for polycrystalline Pt (1.03 mA·cm⁻²). One possible explanation for this difference is that the activity is structure sensitive. Recent work with single crystal Pt surfaces has shown that, in acidic media, the rate of CH₃OH oxidation increases in the order (111) < (100) << (110).¹⁸ The polycrystalline Pt and Pt particle surface can be treated as an ensemble of these low-index facets; therefore, their activity is dependent on the fraction of these facets exposed. XRD measurements indicated that the (110) orientation is dominant on the polycrystalline Pt foil, whereas the (111) and (100) orientations are exposed on the Pt particles. The latter two crystallographic orientations are less active than the (111) orientation for the MOR.

Effect of Pt loading. The possible effect of platinum loading on the MOR kinetics was studied by cyclic voltammetry. Figure 6.2 presents the cyclic voltammetric

i-E curves recorded for the first potential scan in N₂-purged 0.1 M HClO₄ containing 0.6 M CH₃OH. The voltammetric data are summarized in Table 6.3. As seen in Table 6.1, the electrochemically active surface area of the composite electrodes increases with increasing the apparent Pt loading (i.e., increasing deposition time). Accordingly, the peak currents, in both positive and negative scan, follow the same trend. It was also observed that the peak potentials shifted positively with increasing Pt loading due to the increased surface coverage of reactants.

The comparison of the specific activity was made by normalizing the currents obtained at 0.4 V and 0.6 V during the positive scan, with respect to the active Pt surface area. There is no significant change in the specific activity with platinum loading. As discussed earlier, methanol oxidation is a structure-sensitive reaction. The unchanging specific activity implies that the surface structure (crystallographic orientation) of the Pt particles, dispersed onto the diamond, does not change with loading. XRD measurements confirmed that the relative ratio of the low index facets remains nearly constant with varying the Pt loading. For the same reason, the Pt loading also does not considerably influence the onset potential for methanol oxidation.

Effect of anion adsorption. The effect of anion adsorption on the MOR kinetics was examined in 0.1 M HClO₄, H₂SO₄ and H₃PO₄. Figure 6.3 presents the cyclic voltammetric i-E curves for the oxidation of 0.6 M methanol in these media. The main features of the three voltamograms are very similar in potential. However, the anion effect on the peak current is clearly evident. The peak current during the anodic potential scan is ca. 0.68 mA in HClO₄, which is approximately three times higher than in H₂SO₄

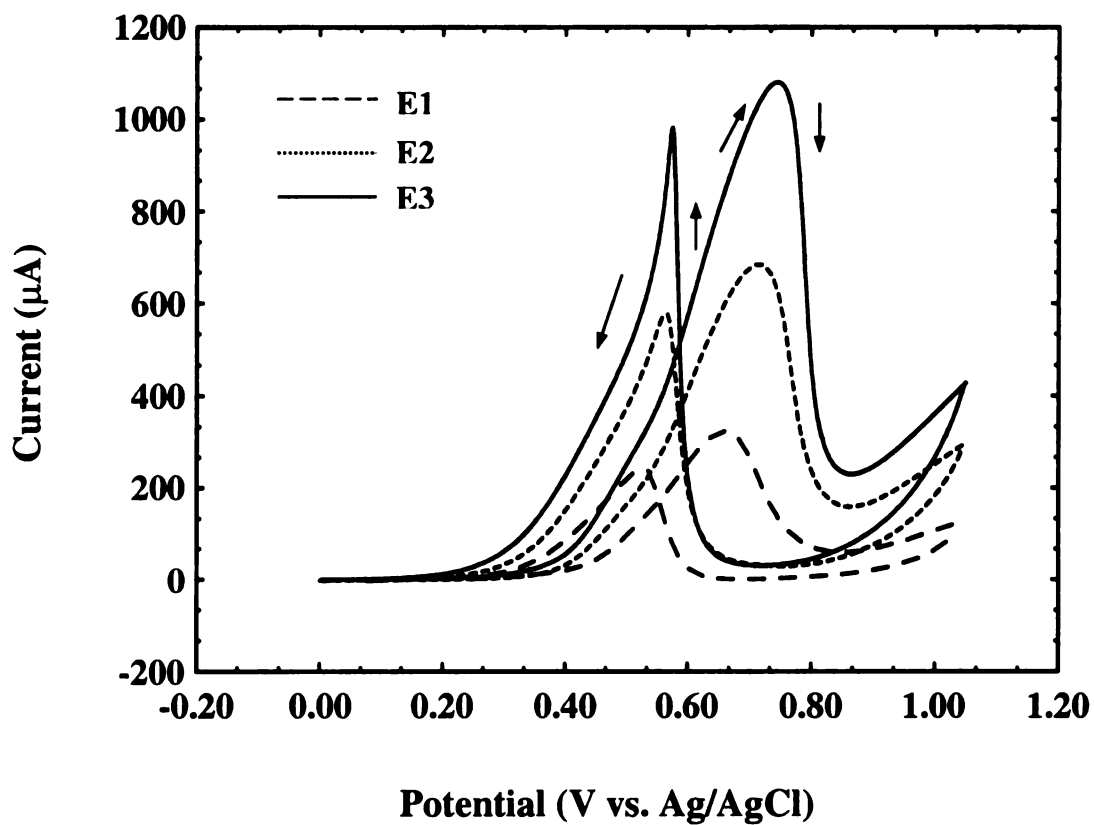


Figure 6.2. Cyclic voltammetric i-E curves for Pt/diamond composite electrodes in 0.1 M HClO₄ + 0.6 M CH₃OH. Scan rate = 50 mV/s.

Table 6.3. Cyclic voltammetric data for the MOR in 0.1 M HClO₄ at Pt/diamond composite electrodes with different Pt loadings.

Electrode	E_{onset} (V)	$E_{\text{p1}}^{\text{ox}}$ (V)	$i_{\text{p1}}^{\text{ox}}$ (mA)	$E_{\text{p2}}^{\text{ox}}$ (V)	$i_{\text{p2}}^{\text{ox}}$ (mA)	SA at $E_a = 0.4\text{V}$ (mA·cm ⁻²)	SA at $E_a = 0.6\text{V}$ (mA·cm ⁻²)
E1	0.23	0.66	0.33	0.52	0.24	0.09	1.05
E2	0.21	0.71	0.68	0.56	0.58	0.08	0.97
E3	0.22	0.74	1.09	0.57	0.98	0.09	0.97

and four times than in H_3PO_4 . The current reduction is due to the fact that sulfate/bisulfate, and phosphate ions are more strongly chemisorbed than are perchlorate ions, and thus, compete with methanol molecules for surface sites leading to a lower oxidation current.

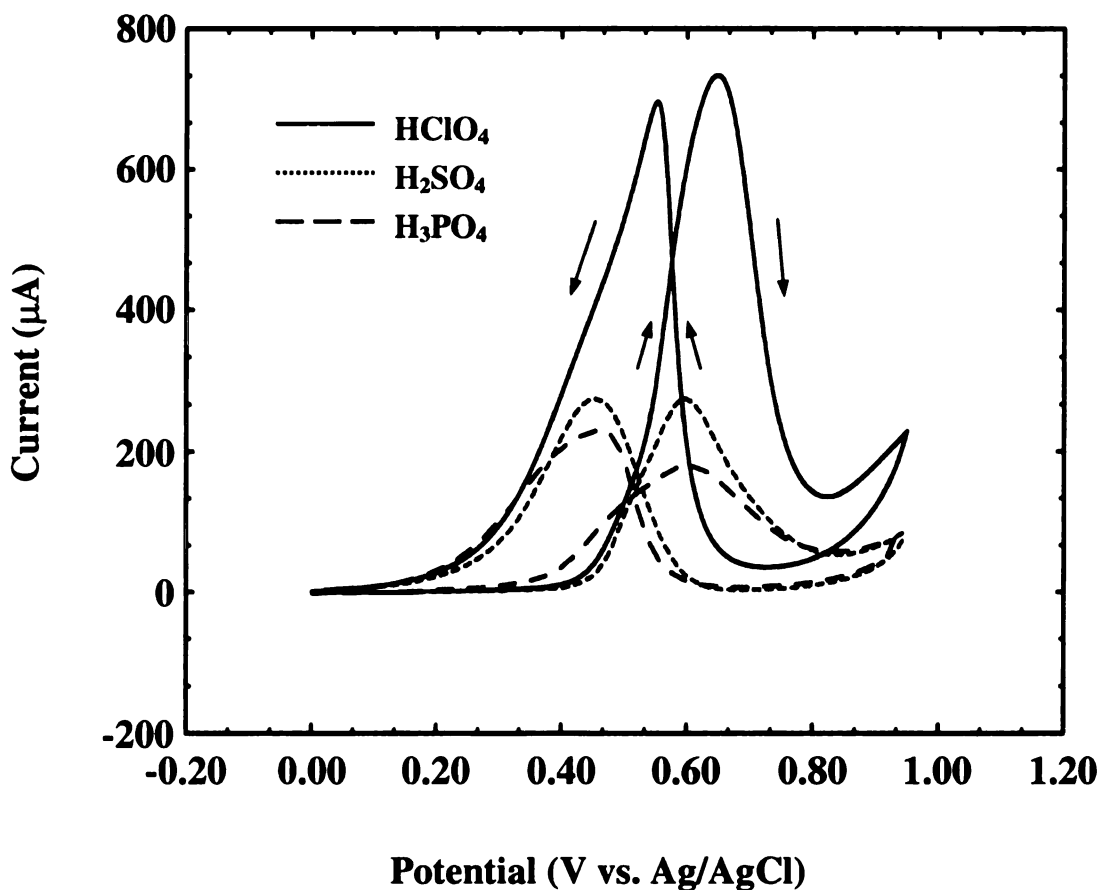


Figure 6.3 Cyclic voltammetric i-E curves for the electrooxidation of 0.6 M CH_3OH in different 0.1 M acid electrolytes at a Pt/diamond composite electrode. Active surface area of the composite electrode is 0.44 cm^2 (Pt deposition time was 200 s). Scan rate = 50 mV/s.

Another interesting feature is observed at low potentials, indicative of a quite different anion effect. At potential less than 0.5 V during the anodic sweep, the highest oxidation current is seen for H₃PO₄. Since only Reactions 6.1-4 take place over this potential range, the observation may suggest that phosphate anion adsorption somehow hinders CO poisoning, which allows for higher rate of methanol adsorption/dehydrogenation. A similar observation was made by Herrero et al. during the study of methanol oxidation on low index Pt surfaces.¹⁸ At low potentials, sulfate/bisulfate adsorption inhibits the methanol oxidation as usual, probably resulting from the enhanced CO formation due to strong lateral CO-bisulfate interaction. This effect was recently confirmed by Ogasawara et al.¹⁹

6.4.2.2 Chronoamperometric Studies of MOR

Cyclic voltammetry is useful for studying the overall reaction kinetics of electrocatalytic reactions, but steady-state chronoamperometric methods offer a more straightforward means to extract detailed mechanistic information about the methanol oxidation process. Two types of chronoamperometric measurements were performed. Analyzing the current decays allows for the Tafel slope, reaction order, and rate-determining step to be determined.

Effect of electrode potential. The current-time transients recorded at different electrode potentials for a Pt/diamond composite electrode immersed in N₂-purged 0.6 M CH₃OH + 0.1 M HClO₄ are presented in Figure 6.4. Prior to each measurement, the electrode was conditioned by the potential pulse cleaning procedure (see experimental section). The potential step was applied from 0 V to the electrode potentials ranging from 0.45 to 0.70 V (refer to Fig. 7.4). The current rises initially due to a combination of

double-layer charging and methanol/adsorbed CO oxidation at a clean electrode surface. The current then decreases as the double layer fully charges and as some sites become blocked by adsorbed organic residues. Possible adsorbates are COH and CO which come

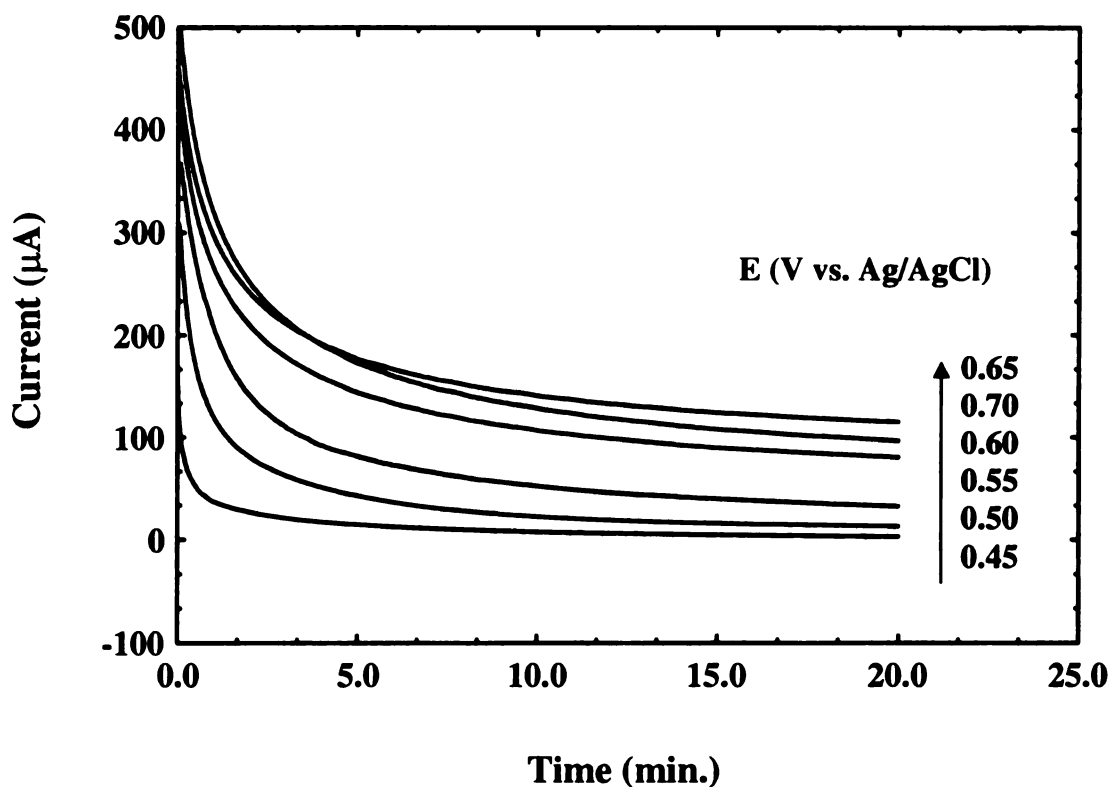


Figure 6.4. Current-time transients for a Pt/diamond composite electrode in 0.1 M HClO₄ + 0.6 M CH₃OH at different electrode potentials. Active surface area of the composite electrode is 0.60 cm².

from the serial reaction pathway. The current-eventually reaches a near steady-state value that depends on the electrode potential. At 0.45 V, the steady-state current at 20 min. is ca. 4 µA. Increasing the electrode potential causes a rise in the reaction rate, consistent with the cyclic voltammetric results. The steady-state current at 0.65 V is ca. 120 µA,

approximately 30 times higher than at 0.45 V. However, further increase in the electrode potential (e.g. 0.7 V) results in a drop in the current, corresponding to the formation of reaction-inhibiting surface oxides.

Effect of methanol concentration. The dependence of the oxidation current on the methanol concentration was investigated by the potential-step method. Figure 6.5 shows a set of current-time transients obtained after the electrode potential was stepped from 0 to 0.6 V vs. Ag/AgCl for a Pt/diamond composite electrode in N₂-purged 0.1 M HClO₄ with methanol concentrations from 0.2 M to 2.0 M. The total oxidation charge and steady-state current density, obtained at 20 min. are listed Table 6.4. The rate of methanol electrooxidation increases with increasing methanol concentration. Evidently, the dependence of the electrooxidation rate upon the bulk concentration is of a fractional order, as even though the methanol concentration is increased by a factor of 10, the oxidation current density in 2 M methanol is only about four times higher than in 0.2 M.

The fractional order of the dependence of the reaction rate upon the bulk concentration of methanol can be interpreted by the Temkin-type methanol adsorption isotherm. It is well known that the rate of methanol electrooxidation depends on the surface concentration rather than bulk concentration of methanol (Equation 6.16). The coverage of methanol residues, however, increases with the bulk concentration in a logarithmic manner (Equation 6.17). Furthermore, the rate of methanol oxidation is controlled by a balance between the adsorbed methanol residues and hydroxyl species, as seen from Equation 6.16. The increase of the coverage of adsorbed methanol residues may block some of the electrode sites, preventing adsorption of hydroxyl species, and therefore, reduce the overall reaction rate.

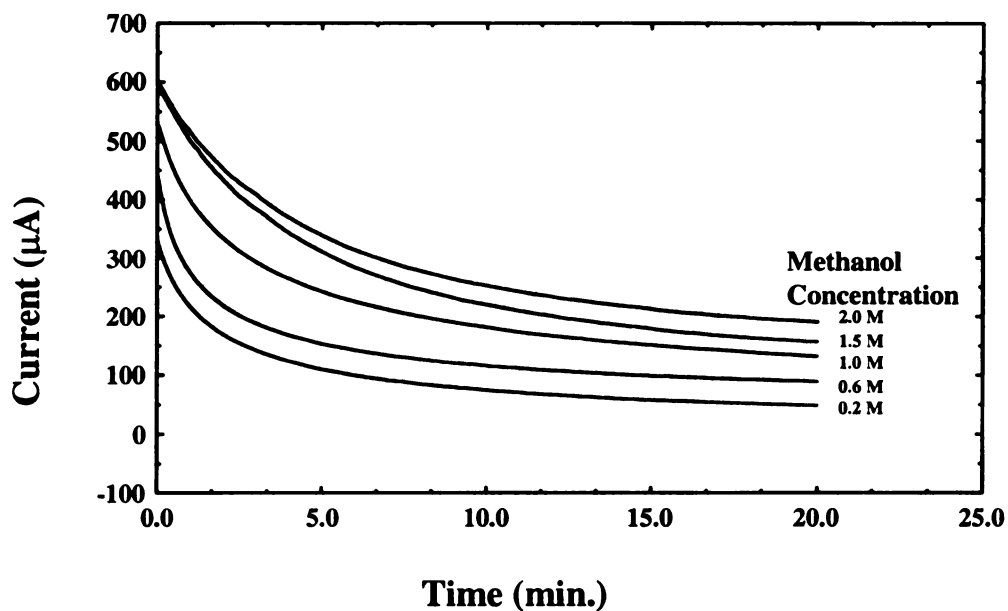


Figure 6.5 Current-time transients for a Pt/diamond composite electrode obtained after a potential step to 0.6 V vs. Ag/AgCl in 0.1 M HClO₄ containing different concentrations of methanol. Active surface area of the composite electrode is 0.60 cm².

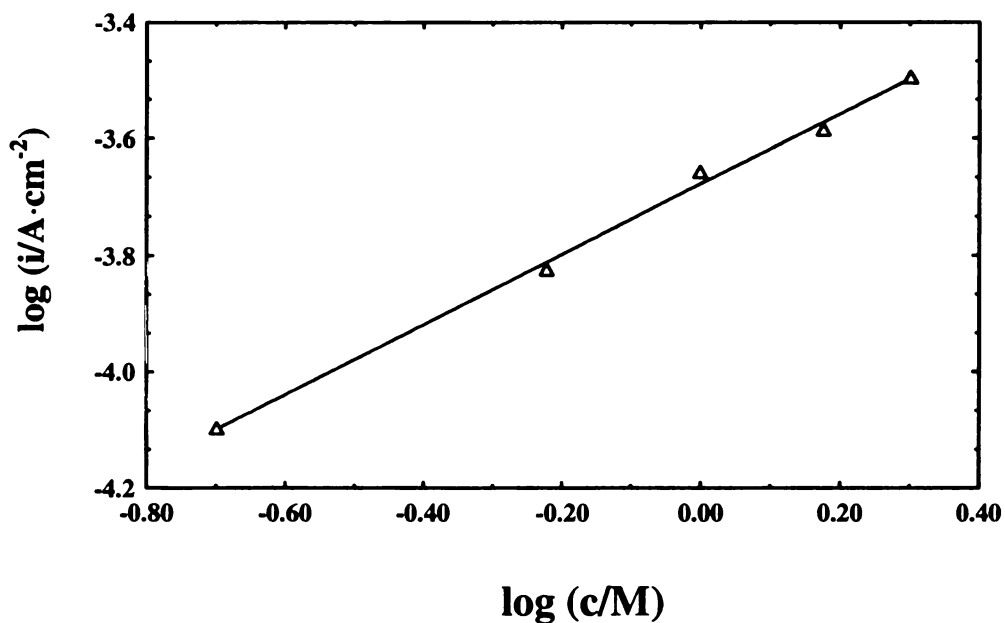


Figure 6.6 Log *i* vs. log *c* plot at 0.6 V vs. Ag/AgCl. Data taken from the current-time transients shown in Figure 6.5.

Nevertheless, the apparent reaction order can be determined by using the following equations. The overall methanol electrooxidation current density can be expressed as²⁰

$$i = nFkC^m \quad (6.18)$$

Where n is the number of electrons, F is the Faraday constant, k is the reaction constant, C is the bulk concentration of methanol, and m is the reaction order, then

$$\log i = \log nFk + m \log C \quad (6.19)$$

and the slope of the $\log i$ vs. $\log C$ at a constant potential gives a apparent reaction order (m) of methanol electro-oxidation reaction with respect to methanol concentration. Using the steady-state current densities, the plot for methanol oxidation is presented in Figure 6.6. A reaction order of 0.6 is estimated, which is similar to that reported by Bagotaky et al.¹⁷ for smooth and platinized Pt electrode.

One of the figures of merit for catalytic activity is the turnover number (tn) defined as the number of the molecules converted per surface site per second. For oxidative heterogeneous catalysis, the turnover number should be in the range from 10 to 100 to make a given material an effective catalyst. However, to date, the turnover number for MOR at the noble metal catalyst in the operational fuel cell is ca. 0.06, still far below the needed performance level. The following formula can be used to calculate the turnover number (tn) from the current density:²¹

$$tn \left(\frac{\text{molecules}}{\text{s} \cdot \text{site}} \right) = \frac{i(\text{mA} \cdot \text{cm}^{-2}) \cdot 6.02 \times 10^{20}}{nF \cdot 1.3 \times 10^{15}} \quad (6.20)$$

There are 1.3×10^{15} platinum sites per 1 cm^2 of the real platinum surface area, and $n = 6$ for the methanol oxidation reaction yielding CO_2 as the product. Collection of the constants yields the formula

$$tn = 0.8 \cdot i(\text{mA} \cdot \text{cm}^{-2}) \quad (6.21)$$

Calculated turnover numbers are listed in Table 6.4. The turnover number increases with methanol concentration as expected.

Table 6.4 Summary of the chronoamperometric i-t data for the oxidation of methanol at a Pt/diamond composite electrode in 0.1 M HClO_4 as a function of the methanol concentration.

Methanol concentration (M)	0.2	0.6	1.0	1.5	2.0
Charge density ($\text{C} \cdot \text{cm}^{-2}$)	0.20	0.30	0.45	0.50	0.55
Steady state current density ($\text{mA} \cdot \text{cm}^{-2}$)	0.08	0.15	0.22	0.26	0.32
Turnover number	0.06	0.12	0.18	0.21	0.26

Note: Data recorded at 20 min. after a potential step from 0 to 0.6 V vs. Ag/AgCl. All measurements were made at room temperature.

6.4.3 MOR at a Bimetallic Catalyst

The best catalyst for methanol oxidation to date, is a Pt/Ru bimetallic catalyst dispersed on a carbon support²²⁻²⁵ or directly on a Nafion PEM membrane.²⁶ The mechanism proposed in Section 6.2 by which the alloy improves the electrocatalytic

activity of pure Pt is a simple bifunctional one. The atoms of different metals act independently and perform different functions. Methanol adsorption and decomposition takes place on Pt, while the Ru atoms provide preferred sites for binding OH_{ads} . In this section, some preliminary results for fabricating and testing Pt/Ru/diamond composite electrodes are presented.

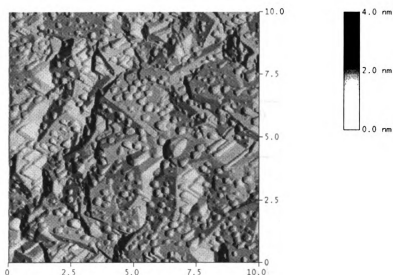


Figure 6.7 AFM image ($10 \times 10 \mu\text{m}$) of a Pt/Ru/diamond composite electrode. The deposition time is 300 s.

Figure 6.7 shows a top-view, $10 \times 10 \mu\text{m}^2$ AFM image of Pt/Ru/ composite electrodes. The co-deposition of Pt and Ru was performed in 0.1 M HClO_4 containing 1 mM K_2PtCl_6 + 0.5 mM RuCl_3 with a deposition time of 300 s. Post metal deposition, diamond film growth was applied for 2 h to entrap the metal particles. Numerous particles are randomly distributed on the microcrystallite facets and in the grain boundaries. The particle size ranges from 50 to 300 nm with a distribution of about $5 \times 10^8/\text{cm}^2$. Energy dispersive x-ray (EDX) analysis confirmed the presence of Ru. The estimated atomic ratio of Pt/Ru was 89:11.

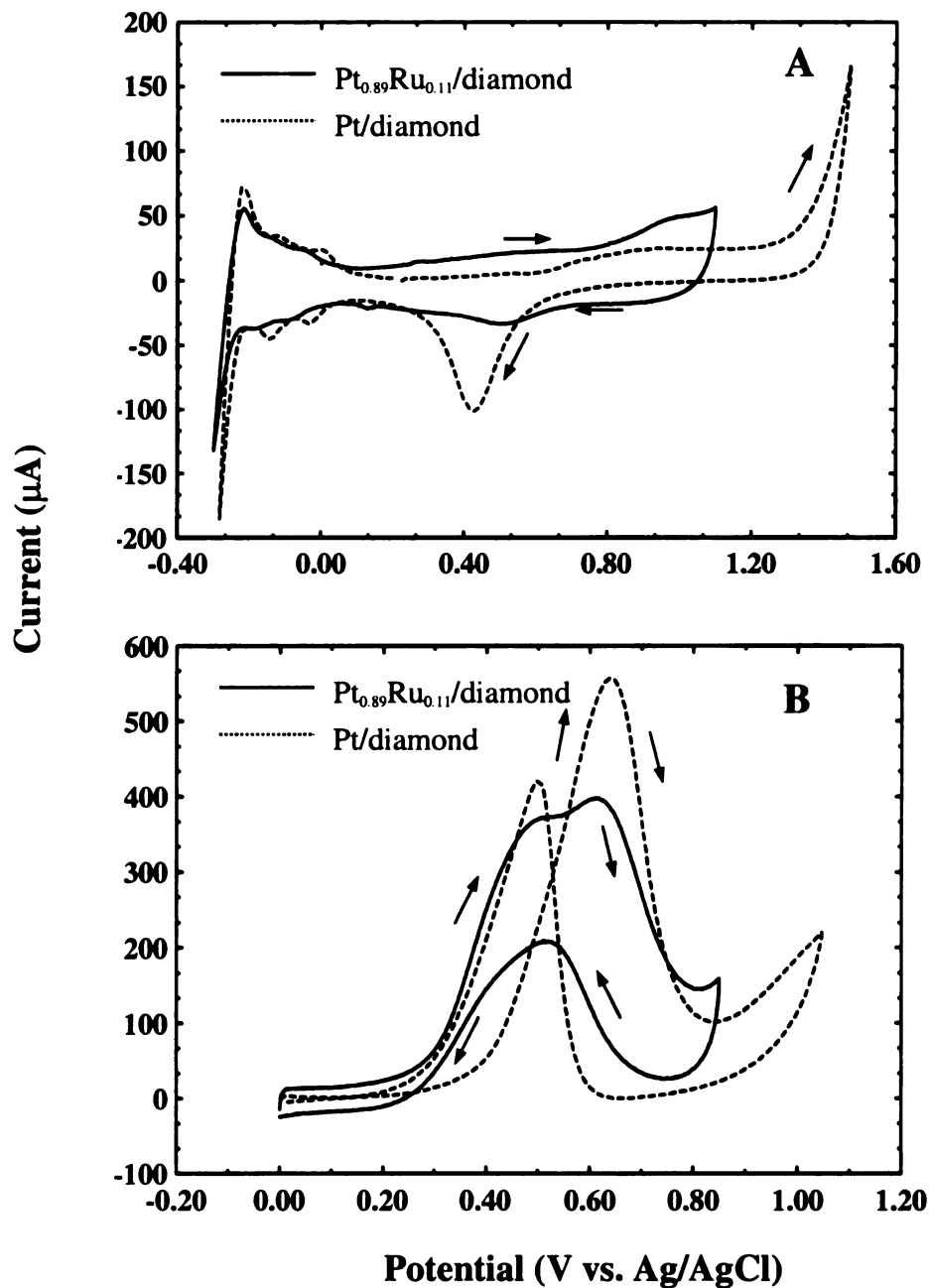


Figure 6.8 Cyclic voltammetric i-E curves for the Pt/Ru/diamond composite electrodes in (A) 0.1 M HClO₄ and (B) 0.1M HClO₄ + 0.2 M CH₃OH. The electrodeposition time is 300 s. Scan rate = 50 mV/s.

The as-deposited Pt/Ru/diamond composite electrode was initially activated by potential cycling in N₂-purged 0.1 M HClO₄. The cycling was limited to between -0.3 and 1.0 V in order to avoid oxidizing the Ru. The cyclic voltammetric i-E curve for the composite electrode is shown in Figure 6.8A. For comparison, the voltammetric response for a Pt/diamond composite electrode, fabricated with the same Pt deposition time of 300 s, is shown as a dashed line. For the Pt/Ru/diamond composite electrode, there are noticeable changes in the voltammetric features. The hydrogen adsorption/desorption peaks are suppressed over the potential range from -0.3 to 0 V, and the charge in the double layer region, 0 to 0.15 V, increases. Discernible faradaic current commences at ca. 0.15 V, presumably due to the dissociation of water to form O-containing species at Ru (Reaction 6.12). The onset potential for dissociative chemisorption of water on Ru is about 0.2 V negative of that for Pt because Ru is more oxophilic than Pt.²⁷ It is reasonable to suppose that this facile dissociation of water on Ru plays an important role in the promotion of methanol oxidation on Pt/Ru catalysts.²⁸

Cyclic voltammetric i-E curves for the electrodes in 0.1 M HClO₄ containing 0.6 M CH₃OH are presented in Figure 6.8B. During the anodic potential sweep, the methanol oxidation current commences at potential as low as 0.1 V, and starts to increase rapidly at 0.2 V. Note that two peaks are observed near 0.48 and 0.62 V, respectively. Since dissociation of water on Ru starts at 0.15 V, the former peak may correspond to the methanol electrooxidation promoted by the adsorbed OH species. The latter one might be attributed to the methanol electrooxidation on Pt sites because it appears at the same potential as that for Pt/diamond electrode. The most notable feature is the drastically

enhanced catalytic activity of the alloy catalyst at low potential. At 0.4 V, the oxidation current on the alloy catalyst is about 6 times higher than that for Pt.

6.5 Conclusions

A kinetic study of the methanol electrooxidation reaction (MOR) on the metal/diamond composite electrodes was presented in this chapter. The results can be summarized as follows:

1. The mechanism of methanol electrooxidation on the metal/diamond composite electrode follows that proposed for polycrystalline Pt and supported Pt catalyst. The specific activity of the supported Pt catalyst on diamond is comparable to that on high surface area carbons.
2. Anion adsorption affects the rate of methanol oxidation. Specifically, adsorbed anions compete with methanol molecules for adsorption sites resulting in a much smaller oxidation currents. Specifically adsorbed anions may also block the adsorption of poison species, minimizing the poisoning effect.
3. The reaction order is about 0.6 over the methanol concentration range from 0.2 to 2 M.
4. Pt/Ru alloy particles can be incorporated into the diamond surface micro-structure. The bimetallic catalyst shows enhanced catalytic activity toward methanol oxidation at low potential region.

References:

1. A. Hammett, in *Interfacial Electrochemistry: Theory, Experiment, and Applications*, A. Wieckowski, Editors, Dekker, New York, 843 (1999).
2. T. D. Jarvi and E. M. Stuve, in *Electrocatalysis*, J. Lipkowski and P. N. Ross, Editors, Wiley-VCH, New York, 75 (1998).
3. B. Beden, J. M. Leger, and C. Lamy, in *Modern Aspects of Electrochemistry*, J. O. M. Bokris, B. E. Conway and R. E. White, Editors, Plenum, New York, **22**, 97 (1992).
4. S. G. Sun, in *Electrocatalysis*, J. Lipkowski and P. N. Ross, Editors, Wiley-VCH, New York, 243 (1998).
5. C. Lamy, J. M. Leger, and S. Srinivasan, in *Modern Aspects of Electrochemistry*, J. O. M. Brokris, B. E. Conway and R. E. White, Plenum, New York, **34**, 53 (2001).
6. C. Lamy and J. M. Leger, in *Interfacial Electrochemistry: Theory, Experiment, and Applications*, A. Wieckowski, Editor, Marcel Dekker, New York, 885 (1999).
7. B. Gurau, A. Bo, Y. Yi, H. W. Lei, S. Suh, R. Liu, S. R. Bare, and E. S. Smotkin, *Preprints of Symposia - American Chemical Society, Division of Fuel Chemistry*, **46**, 691 (2001).
8. H. A. Gasteiger, N. M. Markovic, and P. N. Ross, Jr., *J. Phys. Chem.*, **99**, 8290 (1995).
9. W. Chrzanowaki and A. Wieckowski, *Langmuir*, **14**, 1967 (1998).
10. H. A. Gasteiger, N. Markovic, and P. N. Ross, *J. Phys. Chem.*, **99**, 8945 (1995).
11. B. Grgur, N. Markovic, and P. N. Ross, *J. Phys. Chem. B*, **102**, 2494 (1998).
12. S. Mukerjee and J. McBreen, *J. Electroanal. Chem.*, **448**, 163 (1998).
13. K. Yakikozava, Y. Fujii, Y. Matsuda, K. Nishimura, and Y. Takasu, *Electrochim. Acta*, **36**, 973 (1991).
14. A. Kabbabi, F. Gloaguen, F. Andolfatto, and R. Durand, *J. Electroanal. Chem.*, **373**, 251 (1994).
15. S. L. Gojkovic and T. R. Vidakovic, *Electrochimica Acta*, **47**, 633 (2001).

16. M. Watanabe, S. Saegusa, and P. Stonehart, *J. Electroanal. Chem.*, **271**, 213 (1989).
17. V. S. Bagotzky and Y. B. Vassilyev, *Electrochim. Acta*, **12**, 1323 (1967).
18. E. Herrero, K. Franaszczuk, and A. Wieckowski, *J. Phys. Chem.*, **98**, 5074 (1994).
19. H. Ogasawara and M. Ito, *Chem. Phys. Lett.*, **245**, 304 (1995).
20. A. J. Bard and L. R. Faulkner, *Electrochemical Methods, Fundamentals and Applications*, John Wiley & Sons, Inc, New York, (2001).
21. W. Chrzanowski and A. Wieckowski, in *Interfacial Electrochemistry: Theory, Experiment, and Applications*, A. Wieckowski, Editor, Marcel Dekker, New York, 937 (1999).
22. O. Savadogo and M. Lacroix, *New Materials for Fuel Cell and Modern Battery Systems II, Proceedings of the International Symposium on New Materials for Fuel Cell and Modern Battery Systems, 2nd, Montreal, July 6-10, 1997*, 872 (1997).
23. H. Hoster, T. Iwasita, H. Baumgartner, and W. Vielstich, *Physical Chemistry Chemical Physics*, **3**, 337 (2001).
24. W. Chrzanowski, H. Kim, G. Tremiliosi-Filho, A. Wieckowski, B. Grzybowska, and P. Kulesza, *Journal of New Materials for Electrochemical Systems*, **1**, 31 (1998).
25. W. Chrzanowski and A. Wieckowski, *Langmuir*, **14**, 1967 (1998).
26. X. M. Ren, M. S. Wilson, and S. Gottesfeld, *J. Electrochem. Soc.*, **143**, L12 (1996).
27. A. J. Applyby, *Surf. Sci.*, **27**, 225 (1971).
28. A. Wieckowski, H. Kim, I. R. de Moraes, Q. Lu, and A. Crown, *Book of Abstracts, 218th ACS National Meeting, New Orleans, Aug. 22-26, 1999*.

MICHIGAN STATE UNIVERSITY LIBRARIES



3 1293 02461 5118